THE ELECTROMAGNETIC EXCITATION OF ^{11}Li

By

Donald W. Sackett

A DISSERTATION

Submitted to
Michigan State University
in partial fulfillment of the requirements
for the Degree of

DOCTOR OF PHILOSOPHY

Department of Physics and Astronomy

1992

ABSTRACT

ELECTROMAGNETIC EXCITATION OF ^{11}Li

By

Donald W. Sackett

Abstract

A kinematically complete measurement of the Coulomb dissociation of a 28 MeV/nucleon beam of ^{11}Li into ^{9}Li and two neutrons by a Pb target has been performed. From the energies and angles of the emitted neutrons and of ^{9}Li , the excitation energy E of ^{11}Li was determined on an event-by-event basis, and the Coulomb dissociation cross section as a function of excitation energy was constructed. The dipole strength function $dB(E1)/dE$ and the photonuclear spectrum, $\sigma_{E1}(E)$, were determined from the Coulomb dissociation spectrum. The photonuclear spectrum σ_{E1}(E) has a peak at E=1.0 MeV and a width $\Gamma = 0.8$ MeV. These parameters are consistent with the picture of a soft dipole resonance but a significant post-breakup Coulomb acceleration of ^{9}Li suggests a direct breakup.

The complete kinematical measurement also allowed neutron and ^{9}Li momentum distributions to be constructed in the rest frame of the ^{11}Li . The momentum distributions were fitted with Gaussian functions, yielding width parameters of $\sigma_9 = 18 \pm 4$ MeV/c and $\sigma_n = 13 \pm 3$ MeV/c. A more general feature of the breakup mechanism of ^{11}Li could be deduced from these measurements. It was found that the ^{9}Li and neutron momentum distributions, and the neutron-neutron relative momentum distributions, could be reproduced if the ^{11}Li excitation energy was partitioned between

the ^{9}Li and the neutrons by a 3-body phase space distribution. This indicates there is no directional correlation between the halo neutrons.

To my parents, who always wondered when I would finish school

ACKNOWLEDGEMENTS

First, I would like to thank my thesis advisor, Dr. Aaron Galonsky, for his patience, support and humor through my entire career as a graduate student. He managed to teach a very inexperienced student, one who did not even have an undergraduate degree in physics, a great deal about experimental nuclear physics in a short period of time. I credit his great concern for the welfare and development of his students for much of this achievement.

I would like to thank Dr. Kazuo Ieki, a visiting professor from Rikkyo University, for all of his work on the data analysis of the ^{11}Li and the ^{7}Li(p,n) experiments. Without his co-analysis of the data, and particularily his work with the cross-talk analysis, this thesis would have been delayed at least another six months, perhaps longer. I also would like to thank the many collaborators for helping to make the experiments a success. In particular, I should single out Adam Kiss, Ference Deak, Zoltan Seres and Akos Horvath to thank them for their extensive help with many features of the experiments, and for their wonderful hospitality during my one but very memorable visit to Hungary. I would like to thank my committee for their careful reading of my thesis and helpful suggestions. I also thank the A1200 people for providing a stable and "intense" ^{11}Li beam.

No acknowlegement would be complete without mentioning the help received from fellow students. I would like to thank my office-mates Jim Clayton, Mike Mohar and Matts Cronqvist for their lessons in electronics and data acquisition, and for rarely telling me to look it up in the #$#%# manual. I would also like to thank their replacements, Mathias Steiner, Brian Young and Raman Pfaff, for keeping things lively in the office during the bleak months of data analysis, although their humor, political discourse and fear of daylight probably prolonged my stay at the NSCL by

at least a couple months. I would also like to thank Raman for letting me stay at his apartment (the landfill) for two months while I put the finishing touches on this thesis. I thank John Winfield for answering my many questions about SARA and Ron Fox for teaching me all about data acquisition, interval training and Sushi. I should in general thank all of the cyclotron staff members for their help in making the ^{11}Li experiment a successful one, and I thank the NSCL for their generous financial support during the course of my graduate studies.

Finally, I would like to thank my wife Lisa, who provided the support and encouragement so necessary during the occasional difficult times of the last 5 years. Whether I was studying for exams, setting up an experiment, hurriedly putting together a seminar for a job interview or preparing for the thesis defense, she could always find time to pitch in and make things easier, even though she was also in the midst of a difficult Ph.D. program. Without her companionship during these years, I might well have given up on this whole endeavor. I will always be grateful to her.

Contents

List of Tables

List of Figures

Chapter 1

Introduction

The increasing availablility of radioactive nuclear beams has led to the discovery of several unique properties of light, neutron-rich nuclei. The ^{11}Li nucleus, with 3 protons and 8 neutrons has probably received the most attention, both theoretically and experimentally, due to its rather unique structure. In the first experiments to use a ^{11}Li beam, Tanihata *et al.* [1] measured the total interaction cross section for ^{11}Li and determined the matter radius from the interaction cross section. They also determined the interaction cross sections and matter radii for ^{6}Li, ^{7}Li, ^{8}Li and ^{9}Li, and found that ^{11}Li has a larger matter radius than would be expected from the systematics of the matter radii of the less neutron-rich lithium isotopes. This large matter radius implies a long tail in the ^{11}Li density distribution. In a subsequent experiment, Kobayashi *et al.* [2] found that the transverse momentum distribution of ^{9}Li from the fragmentation of ^{11}Li nuclei has a much narrower width than that expected from the Goldhaber model[3] of projectile fragmentation. The narrow width was interpreted to mean that the density distribution of ^{11}Li has a large spatial extent and the two valence neutrons form a neutron halo around the ^{11}Li nucleus [2, 4, 5]. This halo structure arises from the long tail of the wave function of the valence neutrons due to their small binding energy (S_{2n} = 0.34 MeV [6]). Hence, the halo is expected to be a common feature of nuclei along the neutron drip line.

It was also found that the two-neutron removal cross section of ^{11}Li increased with the atomic number of the target and became extremely large for high-Z targets such as Pb. To explain the target charge dependence, it was suggested that the Coulomb excitation cross section for ^{11}Li is large. Thus a high-Z target would act as a source of photons that bombard the ^{11}Li projectile as it passes [7]. Since ^{11}Li has no bound excited states, ^{10}Li is unbound to neutron decay, and ^{9}Li is particle stable up to 4.06 MeV [8], Coulomb excitation of ^{11}Li up to 4.4 MeV leads only to Coulomb dissociation into a ^{9}Li and two neutrons. To explain the large Coulomb dissociation cross section, a new type of collective excitation was proposed [4, 9, 10]. In this excitation mode, called a soft dipole resonance (SDR), the ^{9}Li core oscillates against the halo neutrons in the ^{11}Li nucleus. This resonance is therefore fundamentally different from the giant dipole resonance (GDR), where all the neutrons oscillate against all the protons. For the SDR, the restoring force of the oscillation is weak because of the low density of the halo, hence the excitation energy of the resonance is expected to be low, near 1 MeV [4, 10], in contrast to the GDR, where the excitation energy would be about 23 MeV [11]. There have been several theoretical studies of the excitation of the SDR [4, 12, 13, 14, 15], but little experimental work has been reported so far because it is necessary to measure the angle and energy of the ^{9}Li and of both neutrons in order to deduce the excitation energy and shape of the SDR. The complete kinematical measurement also allows us to investigate the correlations between the two neutrons. Because ^{10}Li is unbound, the pairing interaction between the two halo neutrons must be crucial to the formation of a bound ^{11}Li system and should play a key role in the halo structure. It has been suggested that the interaction between the halo neutrons may be strong enough to form a dineutron, and that the ^{11}Li structure may consist of a dineutron bound to a ^{9}Li core [4]. The goals of this work were to use the information from a complete kinematic measurement to search

for the soft dipole resonance and to better understand the interaction between halo neutrons as well as their interaction with the ^{9}Li core. We present a A brief review of the formalism of Coulomb excitation theory is presented followed by a detailed description of the experiment. Next results from the ^{9}Li singles data and the one-neutron-^{9}Li coincidence (1n-^{9}Li) data are presented. Finally, several results from the two-neutron/^{9}Li coincidence (2n-^{9}Li) events are presented. Some of the results have been presented in an earlier publication [16].

The basic phenomenon of Coulomb excitation is depicted in Figure 1.1. In the rest frame of the ^{11}Li projectile, there appears to be a projectile with a large atomic number passing by. The ^{11}Li nucleus "sees" a rapidly changing electric and magnetic field due to this projectile. The time-dependent fields can be viewed as a source of virtual photons of various multipolarities that interact with the ^{11}Li nucleus. Photons with energies E greater than the neutron separation energy of ^{11}Li may be absorbed and either be re-emitted or induce dissociation into a ^{9}Li and two neutrons. For photon energies greater than 4.4 MeV, other channels are also possible, such as dissociation into a ^{8}Li and three neutrons. The bottom half of Figure 1.1 portrays a case where a photon was absorbed at a specific energy in the ^{11}Li continuum. The energy difference E_d=E-S_{2n} is referred to as the decay energy, and it is distributed between the emitted ^{9}Li and neutrons. The soft dipole resonance is predicted to lie in this continuum, near E=1 MeV, hence $E_d \approx 0.7$ MeV since $S_{2n} = 0.34$ MeV [6]. The measurement of the angles and energies of the ^{9}Li and neutrons yielded the value of E_d on an event-by-event basis, which allows the Coulomb dissociation cross section to be determined as a function of excitation energy. The terms Coulomb excitation and Coulomb dissociation will be used interchangeably in the remainder of this work since Coulomb excitation of ^{11}Li up to 4.4 MeV is equivalent to Coulomb dissociation of ^{11}Li into a ^{9}Li and two neutrons.

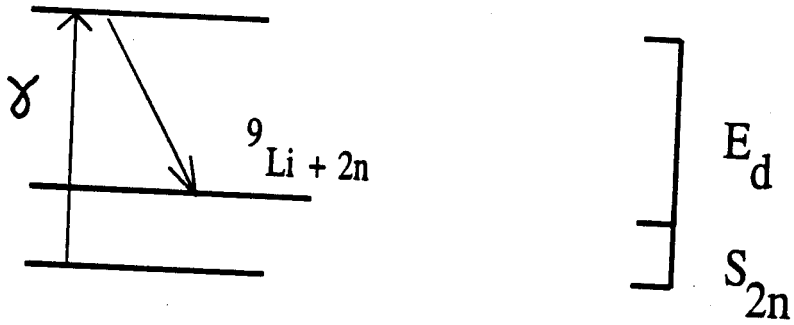

$$E = E_d + S_{2n}$$

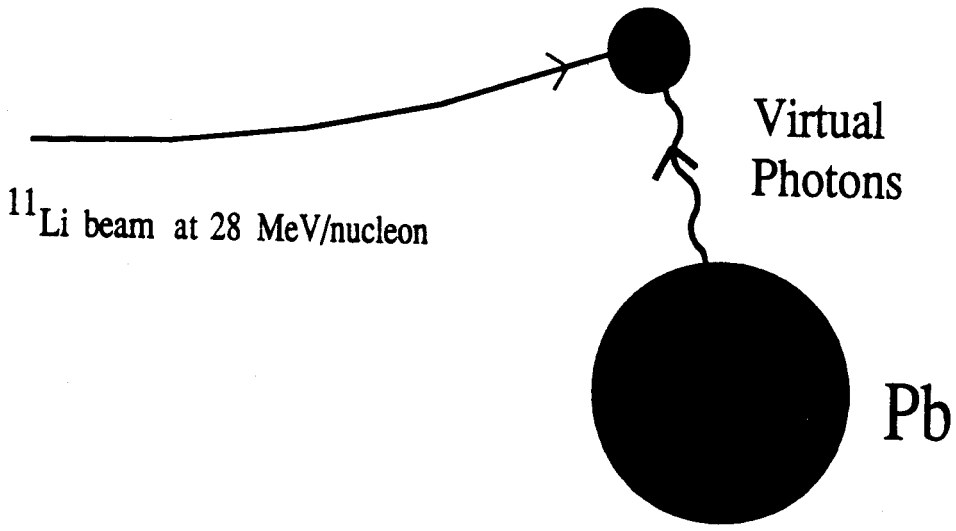

Figure 1.1: Coulomb excitation of a ^{11}Li projectile. The Pb target acts as a source of virtual photons. An excitation to the continuum followed by decay to ^{9}Li and two neutrons, with decay energy E_d is also shown.

The cross section $d^2\sigma/dEd\Omega$ for electromagnetic excitation of a projectile in the Coulomb field of a target was derived in first order perturbation theory by Alder and Winther [17]. Specializing to electric dipole excitation, $\lambda = 1$, and following Ref. [18] find:

$$\frac{d^2\sigma_c}{dEd\Omega} = \frac{dN_{E1}(E,\Omega)}{d\Omega}\,\frac{\sigma_{E1}(E)}{E} \tag{1.1}$$

Here, E is the excitation energy delivered to the projectile and $d\Omega$ is the element of solid angle into which the projectile deflects. The photonuclear cross section $\sigma_{E1}(E)$ is related to the dipole strength function $dB(E1)/dE$ by:

$$\sigma_{E1}(E) = \frac{16\pi^3}{9\hbar c}\,E\,\frac{dB(E1)}{dE} \tag{1.2}$$

The quantity $dN_{E1}(E,\Omega)/d\Omega$ is given by [18]:

$$\frac{dN_{E1}(E,\Omega)}{d\Omega} = \frac{Z_T^2\alpha}{4\pi^2}\,(\frac{c}{v})^2\,\varepsilon^4\xi^2 e^{-\pi\xi}[\frac{\varepsilon^2-1}{\varepsilon^2}\,[K_{i\xi}(\varepsilon\xi)]^2 + [K'_{i\xi}(\varepsilon\xi)]^2] \tag{1.3}$$

Here, Z_T is the target charge, α is the fine structure constant, v is the relative velocity, a is half the distance of closest approach for a head on collision in a strictly Coulomb potential, γ is the Lorentz boost for the relative velocity v, $\xi = Ea/\hbar\gamma v$ and θ is the Coulomb deflection angle of the projectile. The angular dependence in Eq. 1.3 is given in terms of ε, the eccentricity of the Coulomb orbit, which is related to the Rutherford scattering angle by $\varepsilon = 1/\sin(\theta/2)$. The function $K_{i\xi}(\varepsilon\xi)$ is a modified Bessel function of imaginary argument, and $K'_{i\xi}(\varepsilon)$ is the derivative of K with respect to the argument. Eq. 1.1 can be integrated over all pure Coulomb orbits to yield the cross section as a function of the excitation energy:

$$\frac{d\sigma_c}{dE} = \frac{N_{E1}(E)}{E}\,\sigma_{E1}(E) \tag{1.4}$$

$N_{E1}(E)$, referred to as the equivalent photon spectrum, is a dimensionless function of the projectile energy and the excitation energy E. $N_{E1}(E)$ represents the number

of virtual photons at energy E available to the projectile from the Coulomb field of the target. The quantity σ_{E1}(E) reflects the probability that the nucleus will absorb an E1 photon of energy E. Thus, the cross section for E1 excitation to energy E is a product of the number of E1 photons available at an energy E multiplied by the nuclear strength for absorbing such a photon. This formulation of the Coulomb excitation cross section is known as the equivalent photon method [18]. It has a long history of success in predicting the excitation of low-lying collective states in stable projectiles [17], so it is natural to extend the method to a search for low-lying E1 states in neutron-rich nuclei such as ^{11}Li . One of the appealing features of the method is that the measurable quantity in the laboratory, $d\sigma_c/dE$, is related in a straightforward manner to the quantities of theoretical interest, $dB(E1)/dE$ or $\sigma_{E1}(E)$, by the photon spectrum. Thus a measurement of $d\sigma_c/dE$ and a calculation of N_{E1}(E) will yield $dB(E1)/dE$ and σ_{E1}(E) directly.

Contributions from other multipoles, specifically M1 and E2, were estimated to be negligible. The expression for N_{E1}(E), valid for all projectile energies, is given in [18]. An approximate expression for relativistic projectile energies is also given in [18]. For a ^{11}Li beam at 28 MeV/nucleon, the relativistic approximation agreed with the exact calculation to within 2%. Both the M1 and the E2 photon spectra, N_{M1}(E) and N_{E2}(E), were calculated in the relativistic approximation as well [18]. The M1 spectrum was several orders of magnitude less than the E1 spectrum, but the E2 spectrum was about 400 times greater than the E1 spectrum in our energy range [18]. However, it has been shown for several models of the ^{11}Li nucleus that $\sigma_{E2}(E) < 10^{-5}\sigma_{E1}(E)$ [19]. Hence, $N_{E2}(E)\sigma_{E2}(E) < 0.004 N_{E1}(E)\sigma_{E1}(E)$.

Chapter 2

Experimental Setup

2.1 The ^{11}Li Beam

The ^{11}Li beam striking the lead target had an average energy of 30 MeV/nucleon. This beam energy was used because the neutron cross-talk problem (see below) becomes more tractable if lower energy neutrons are present and because the E1 Coulomb excitation cross section is inversely proportional to the beam energy. Of course, an even lower beam energy could have been chosen to further exploit these effects. However, the ^{11}Li beam was produced via projectile fragmentation of an ^{18}O beam at 80 MeV/nucleon, and both the intensity and quality of the ^{11}Li beam suffer as either the ^{18}O beam energy or the ^{11}Li beam energy are lowered.

A 0.7 g/cm^2 ^{9}Be production target was bombarded with an 80 MeV/nucleon $^{18}O^{6+}$ primary beam produced by the K1200 cyclotron at Michigan State University. The primary beam current was 1.2×10^{11} particles/s. The ^{11}Li exiting the production target had an average energy of 61 MeV/nucleon. The ^{11}Li was separated from most other reaction products by the A1200 Fragment Separator [20]. After exiting the fragment separator, the ^{11}Li beam traversed two dipole magnets and several quadrupole magnets and was further degraded to 30 MeV/nucleon before reaching the experimental vault and 0.60 g/cm^2 Pb target. A 7 cm thick plastic scintillator (called S1)

on a phototube was placed after the first dipole magnet to reduce the beam energy. The dipole magnet produced a dispersion in the beam, hence S1 was machined into a wedge-like shape to match the predicted dispersion, thereby minimizing the energy spread induced in the ^{11}Li beam by S1. After S1, the beam traversed the second dipole (a 14 ° bend) and entered the experimental area. The experimental area was shielded from the beamline containing S1 by a concrete wall 1.4 m thick. Because of the 14 ° bend in the beamline and the concrete wall, few neutrons produced by reactions in S1 reached the neutron detector array. The time of flight (TOF) of each beam particle was measured across a 15.45 meter flight path between S1 and the first ΔE detector in the fragment telescope (described in the next section). The average energy of the final beam striking the Pb target was 30 MeV/nucleon, with a spread of $\pm$ 2.5 MeV/nucleon. Energy loss in the tartet was 4.0 MeV/nucleon. An average of 400 ^{11}Li 's/second reached the Pb target, and the beam was approximately 80% ^{11}Li . The four most prevalent contaminants were 12% ^{8}He at 25 MeV/nucleon, 6% tritons at 45 MeV/nucleon, 1% ^{9}Li at 45 MeV/nucleon and 0.02% ^{14}Be at 33 MeV/nucleon. Although it was possible for these contaminants to react with Pb and produce a ^{9}Li , only ^{14}Be would have produced ^{9}Li at high enough energies to be included in the gated ^{9}Li spectrum from ^{11}Li dissociation. The energy of ^{9}Li from ^{11}Li dissociation in the Pb target was 28 $\pm$ 2 MeV/nucleon. The possible contribution from the ^{14}Be was neglected because of the small percentage present in the beam.

The detector set-up is shown in figure 2.1. The beam spot size at the lead target was large, about 2.5 cm $\times$ 2.5 cm, and the average angular spread of the incident beam was 0.5 °, so it was also necessary to measure the incident angle and target position of each ^{11}Li particle to accurately determine the angle of the emitted ^{9}Li fragment. This was done with two position-sensitive parallel plate avalanche counters (PPACs) separated by 1.09 m. With the position information from the PPACs, the incident

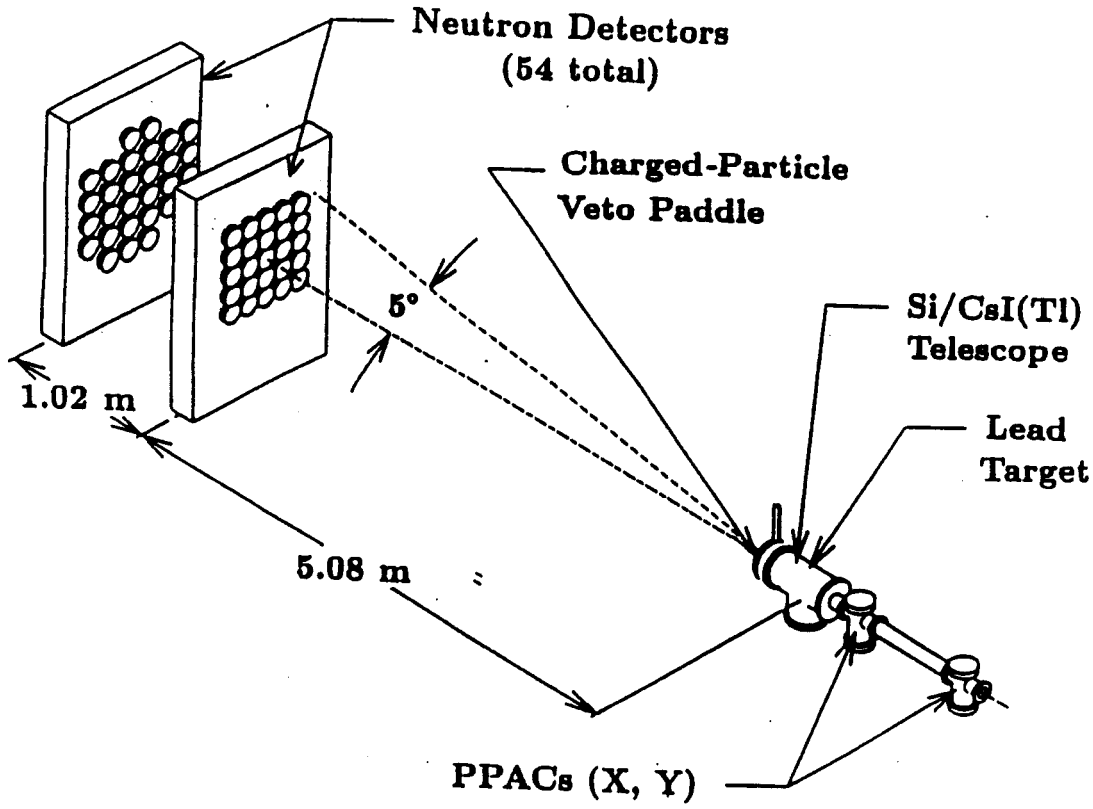

Figure 2.1: The detector setup. The detector telescope is located at zero degrees inside the target chamber, 15 cm downstream from the target. The neutron detectors are mounted in two styrofoam blocks.

angle and target position of the ^{11}Li particle could be calculated. The PPACs were filled with isooctane gas at a pressure of 5 Torr. The signals in the PPACs were resistively divided into up, down, left and right signals. From these pulse heights, the particle position in each PPAC was calculated with a resolution of 1.5 mm. The PPAC detection efficiency for ^{11}Li was greater than 99.7%.

2.1.1 The Fragment Detectors

The ^{11}Li and ^{9}Li fragments were detected and identified with a silicon/CsI(Tl) telescope centered at 0°. The telescope consisted of two silicon ΔE detectors and a CsI(Tl) E detector. The first ΔE detector was a MICRON position sensitive silicon strip detector 5 cm x 5 cm x 300 μm, consisting of 16 horizontal strips on one side and 16 vertical strips on the other [21]. Each strip was 3.125 mm wide, the detector was 14.6 cm from the target and it subtended a half-angle of 9°. The group of 16 horizontal and 16 vertical strips could be thought of as forming a grid consisting of 256 square pixels with sides of length 3.125 mm. The angle of the ^{9}Li was determined by the pixel that the particle traversed and that pixel was identified by the ΔE signals from the horizontal and vertical strips that were struck. A fast signal was also picked off of the ΔE pulse coming from the struck horizontal strip. The fast signal provided a stop for the neutron TOF measurement and a start for the incident ^{11}Li TOF measurement. Three of the horizontal strips (#8,#15 and #16) did not work during the experiment. The second silicon ΔE detector was placed behind the strip detector to increase the ratio of energy loss to straggling. This detector was a MICRON 5cm x 5cm x 300 μm silicon detector.

The remaining energy was measured with a rectangular 6 cm $\times$ 6 cm $\times$ 1.2 cm thick CsI(Tl) crystal, the light being read-out with four Hamamatsu S3204 pin diodes attached to the back of the CsI(Tl) crystal. The CsI(Tl) was calibrated with

^{9}Li beams of energies of 34.0 MeV/nucleon and 45.0 MeV/nucleon. The calibration beams were also produced by the fragmentation of ^{18}O on a ^{9}Be target and separated by the A1200 Fragment Separator. Although in general the light output from CsI(Tl) is not proportional to the deposited energy, for high energy particles over a limited energy range, the response is quite linear [22]. Therefore two calibration points for ^{9}Li were sufficient. The ^{9}Li energy spread was limited to 0.6% full width at half maximum (FWHM). Both S1 and the Pb target were removed during the calibration.

One disadvantage of CsI(Tl) crystals is that their light output response may depend upon where the particle strikes the crystal due to non-uniformity of the thallium doping [23]. Using the grid defined by the silicon strip detector, the CsI(Tl) crystal could also be considered a grid of 256 square pixels. For each calibration beam, the light output from each pixel was determined separately. The light output varied by as much as 25% over the area of the crystal. Therefore, a separate calibration was made for each pixel region. Using this technique, the energy resolution was about 2% FWHM, or 6 MeV for the lower energy calibration beam, and the problem of the non-uniformity of the crystal response was eliminated. In general, the light output from a CsI(Tl) crystal depends not only on the incident energy, but also on the charge Z and mass number A of the impinging particle [24, 25]. In addition to ^{9}Li , the calibration beam contained small quantities of several other isotopes. Calibration points for ^{7}Li, ^{8}Li, ^{9}Be, ^{10}Be, ^{11}Be, ^{12}Be, ^{11}B, ^{12}B, ^{13}B, ^{14}B, ^{14}C, ^{15}C and ^{16}C were also available. The calibration procedure was repeated for these particles and found a Z-dependence for all the calibrations, but a neglibible A-dependence.

2.1.2 The Neutron detectors

The neutrons were detected with an array of 54 cylindrical detectors, each about 7.4 cm thick and 12.5 cm in diameter filled with either Bicron 501 or NE 213 liquid

scintillator. As shown in Figure 2.1, the detectors were arranged in two layers about 5 and 6 m from the target. There were 25 detectors in the first array, and 29 in the second. In each array the detectors were inserted into holes cut in a block of styrofoam 20 cm thick and 1.22 m on a side. Because the dominant reaction channel was expected to be low energy Coulomb excitation of ^{11}Li followed by decay to a ^{9}Li and two neutrons, the neutrons were expected to be concentrated in the forward direction. Therefore all the detectors were placed at forward angles. The detector arrays were centered at 0 ° and subtended a half-angle of 5 °. The neutron energies were measured via the time-of-flight method using the fast signal from the neutron detector as a start and the fragment signal in ΔE_1 as the stop. The timing resolution was 1.2 ns. A veto paddle was placed just outside the target chamber to reject any charged particles that might reach the neutron detectors.

The γ-rays from fragment/γ-ray coincidence measurements provided the calibration for the neutron TOF measurement. Although the neutrons were predominately in the forward direction, the γ-rays were produced much more isotropically, and almost all of them missed the neutron detectors. In order to produce a substantial γ-ray peak in the TOF spectrum of each neutron detector, each detector array was placed 1/2 m from the target instead of the five or six meter distance used during the rest of the experiment. This increased the solid angle coverage by a factor of 100 and 144 for the array at five or six meters, respectively. Also, during the calibration, the lead target was removed and the 1.2 cm thick CsI(Tl) detector was used as a target instead. Since the Pb and the CsI were separated by 16 cm, γ-ray peaks separated by 1.65 ns would have been produced in the TOF spectrum. These γ-ray peaks might not have been resolvable and therefore could have produced a systematic error in the neutron TOF calibration.

The γ-ray background was determined via pulse-shape discrimination [26]. The

number of γ-ray/^{9}Li coincidences was about 10% of the number of 1n-^{9}Li coincidences. For a neutron detector at 1.7 ° the TOF spectrum for both neutrons and γ-rays is shown in Figure 2.2. Except for the peak at 17 ns representing the target γ-rays, (these are the target γ-rays detected when the detector arrays are at five and six meters, not the target γ-rays from the TOF calibration) the γ-ray TOF spectrum is well correlated with the neutron TOF spectrum. It is suspected that γ-rays with TOF's similar to the neutron TOF's resulted from neutron reactions with the liquid scintillator or surrounding detector material in which a γ-ray was produced and made a pulse in the same detector or a neighboring detector. The number of detected γ-rays from such neutron reactions was estimated. Using the cross sections for γ-ray-producing neutron reactions with the carbon in the scintillator, the carbon, oxygen and nitrogen in the light pipe, the silicon and oxygen in the glass cell holding the scintillator and the aluminum in the detector housing, and considering the γ-ray efficiency of the neutron detectors, the estimated the number of γ-ray /^{9}Li coincidences is about 8% of the number of neutron-^{9}Li coincidences. This is in good agreement with the measured value of 10% and supports the hypothesis regarding the source of most of the γ-rays.

To measure neutron background from scattering in the target chamber or surrounding areas in the vault, some data were taken with a shadow bar placed just after the target chamber, in place of the veto paddle (Figure 2.1) to block neutrons coming directly from the target. This contribution was found to be <2%.

2.1.3 Cross-Talk

The measured triple coincidence events (^{9}Li plus two neutrons) contain a mixture of true neutron-neutron (n-n) events and cross-talk events. Cross-talk occurs when one neutron makes a signal in a detector and scatters into another detector, making

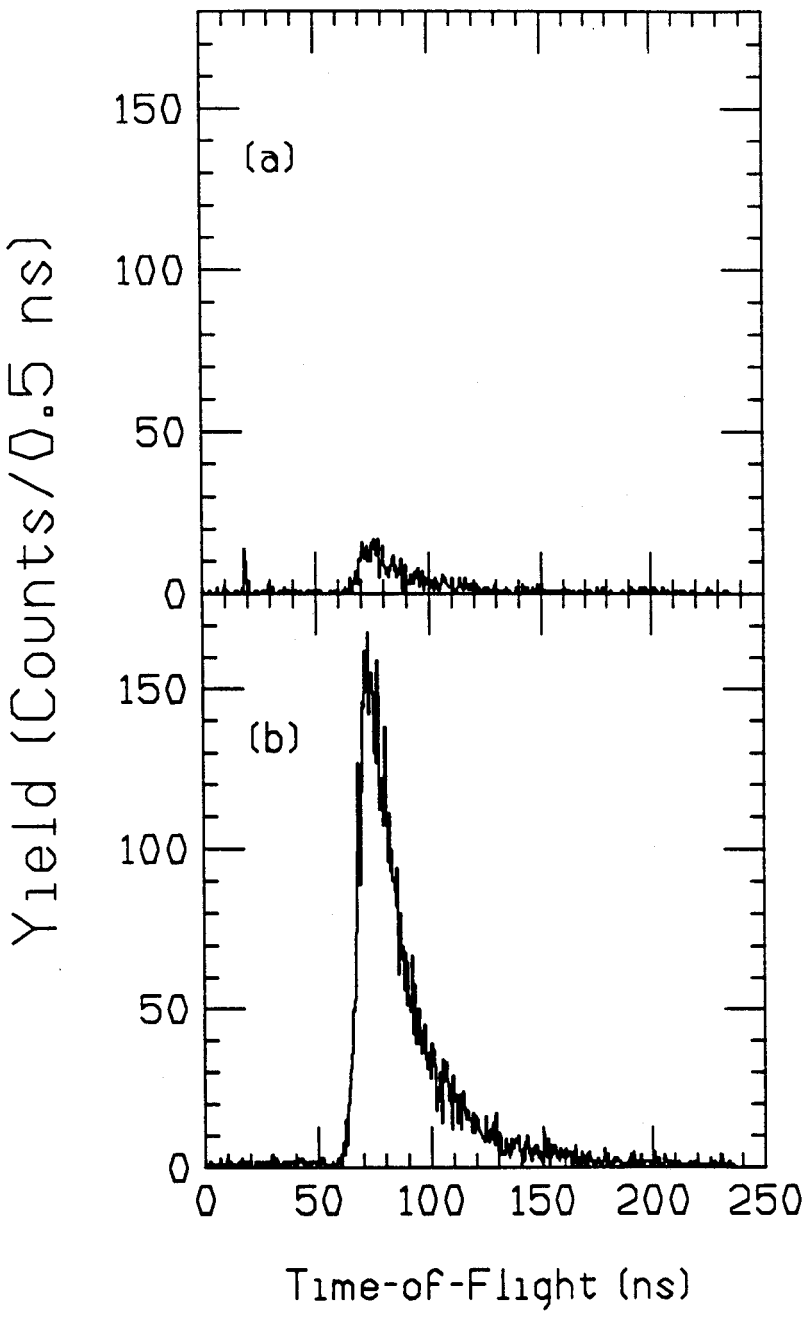

Figure 2.2: (a) A Time-of-flight spectrum for ^{9}Li /γ-ray coincidence events. (b) Time-of-flight spectrum for ^{9}Li -neutron coincidence events.

a signal there too. Cross-talk events are most prolific for detectors that are close together because of the large solid angle available to the scattered neutron from the neighboring detectors. The cross talk contribution is not necessarily negligible, in fact it can be quite large [27, 28]. Therefore some care must be taken to subtract this contribution from the data.

The kinematics of each event were examined and those events that could have been cross-talk were rejected. The average neutron energy was about 27 MeV. At this energy, the most probable reactions in the neutron detector scintillator that also yield a neutron as one of the reaction products are:

$$n + p \rightarrow n + p \tag{2.1}$$

$$n + C \rightarrow n + C \tag{2.2}$$

$$n + C \rightarrow n + 3\,\alpha\ - 7.6\ \text{MeV} \tag{2.3}$$

If a neutron is not one of the reaction products, then there is no chance of a cross-talk event. Using a neutron detector threshold above about 1 MeV electron energy restricts the detected events to those resulting from n-p elastic scattering because the α-particles and carbon only create a small amount of light in the scintillator. For a true coincidence event, the TOF of each neutron and the recoil energies of the protons in the scintillators are measured. For a cross-talk event, the TOF of one of the target neutrons, the time required for the same neutron to traverse the distance to the next detector and the recoil proton energies are determined. An energy spectrum, defined as counts per MeV versus ΔE_n, where $\Delta E_n = E_n\text{-}E_s\text{-}E_p$, was made from all the triple coincidence events. For the cross-talk events, E_n is the energy of a target neutron, E_p is the energy of the recoil proton scattered by this neutron, and E_s is the energy of

this neutron after it has scattered from the proton in the scintillator. For the cross-talk events, ΔE_n should be zero by energy conservation, but for true coincidences, ΔE_n is completely random since the energy E_s is a meaningless quantity. Therefore, a ΔE_n spectrum will consist of a peak at $\Delta E_n = 0$ for the cross-talk events and a broad distribution from the true coincidences, which is what was observed.

A gate was drawn around the peak at ΔE_n =0 and events within this gate were rejected as cross-talk. The width of the gate was determined in a separate experiment in which the ^{7}Li(p,n) reaction was used to generate neutrons at 27 MeV and send them into a neutron detector array of similar geometry. In this case, all n-n coincidence events were cross-talk, so the ΔE_n spectrum consisted of only a peak around ΔE_n =0. The width of the gate required to reject cross-talk was taken from this spectrum. The width of the gate also represents the overall cross talk resolution of the neutron detector system. Of course, in the ^{11}Li experiment the coincidence events are a mixture of true coincidences and cross-talk. Because the true coincidences yielded an arbitrary value for ΔE_n, some true coincidence events were within the ΔE_n gate and therefore rejected as cross-talk. Using the cross-talk rejection procedure, 20% of the total true-plus-cross-talk events in the ^{11}Li data were rejected during the analysis. The remaining events, called the true events, were used in the remainder of this work. The Monte Carlo studies revealed that 13% of the events rejected could have been true coincidences and that the set of true events contained at most a 10% contamination by cross-talk events. The Monte Carlo study of the neutron events was developed using the cross section data of Cecil *et al.* citeCecil. The n-n coincidences from the ^{7}Li(p,n) reaction were composed entirely of cross-talk events and were used to test the Monte Carlo calculation.

The small cross-talk contamination in the true events were further studied to determine if any bias was induced in specific spectra. The spectrum $d\sigma_c/dE$ will

yield the photonuclear cross section as a function of excitation energy, which in turn may reveal the shape and peak location of the soft dipole resonance. Therefore, it is important to have a measurement of $d\sigma_c/dE$ that is reasonably free of bias from cross-talk contamination. The spectrum for $d\sigma_c/dE$ was studied four ways. The spectrum was constructed from all the 2n-^{9}Li events and from only the true events. A simulated spectrum for $d\sigma_c/dE$ was produced from the Monte Carlo simulation with and without cross-talk rejection. For all these cases the shape of the spectrum was equivalent within statisitcal uncertainties. Therefore it was concluded that the 10% cross-talk contamination present in the true events does not affect the shape of the spectrum for $d\sigma_c/dE$.

A measurement of the n-n relative momentum spectrum might provide some insight into the halo neutron interaction. For example, a narrow peak at low relative momenta may reveal a dineutron structure for the halo neutrons, or at least indicate the presence of a strong correlation. However, because cross-talk events are more likely to occur between neighboring detectors, cross-talk contamination can generate a spurious peak at low relative momentum and lead to an incorrect conclusion about the halo neutron structure. Therefore, great care must be taken to be sure that any peak at low relative momentum is not produced by unrejected cross-talk events.

Although the cross-talk rejection used in this work was sufficient for determining $d\sigma_c/dE$, an additional analysis procedure using the results from the ^{7}Li(p,n) reaction was required for determining a n-n relative momentum spectrum. Because all the 2n events from the ^{7}Li(p,n) reaction are the result of cross-talk, a n-n relative momentum spectrum could be made from these data consisting of only cross-talk events. The relative momentum is defined as q= $\frac{1}{2} \mid \vec{p}_1 - \vec{p}_2 \mid$. This spectrum, shown in Figure 2.3 for the ^{7}Li(p,n) data, has a sharp peak at 3.5 MeV/c. It is expected that the cross-talk events from ^{11}Li breakup would also produce a peak at low q. The n-n relative mo-

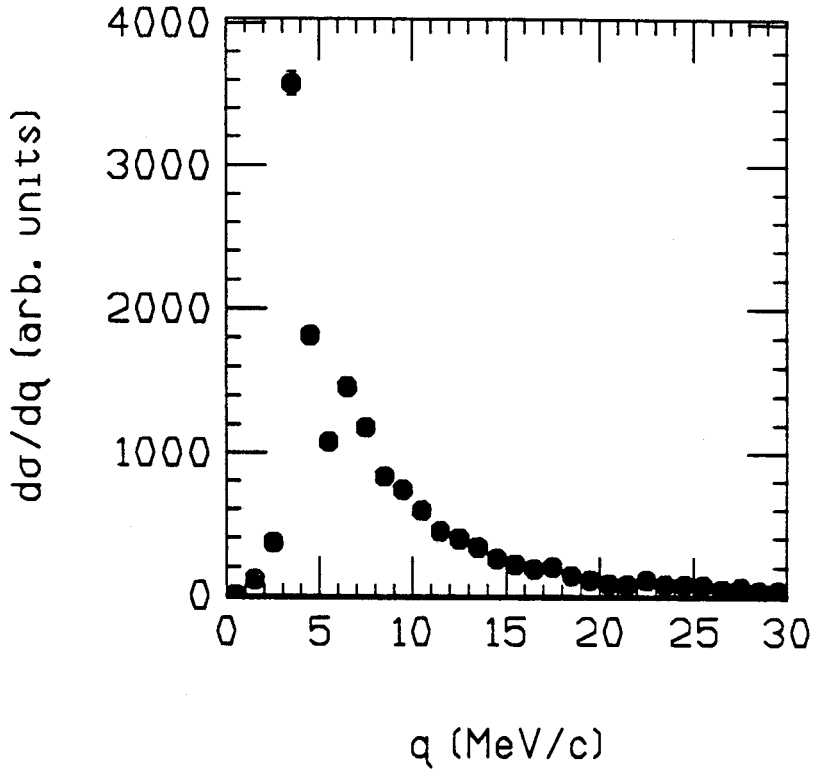

Figure 2.3: A n-n relative momentum spectrum due to cross-talk events only, using the ^{7}Li(p,n) reaction to produce neutrons at 27 MeV.

mentum spectrum for ^{11}Li breakup is shown in Figure 2.4a. There is an enhancement near q=5 MeV/c, corresponding to a relative energy of 30 keV. It is not clear if the enhancement at q=5 MeV/c should be attributed to the nature of the halo neutron interaction or if it is due to unrejected cross-talk events. Unrejected cross-talk events between neighboring detectors would appear near q=5 MeV/c because the distance between neighboring detectors was greater for the ^{11}Li experiment.

The effect of cross-talk contamination was further evaluated by using the data from the ^{7}Li(p,n) reaction. The n-n relative momentum spectrum from the ^{7}Li(p,n) data, which was composed entirely of cross-talk events, was subjected to the same cross-talk rejection procedure as the data from the ^{11}Li experiment. This spectrum was then normalized to the corresponding ^{11}Li data by the total number of 1n events, and then subtracted from the ^{11}Li spectrum. The neutron detector thresholds were also increased to 3 MeV electron energy. This corrected spectrum is shown in Figure 2.4b. The enhancement at q=5 MeV/c has been eliminated and the resulting spectrum varies smoothly as a function of the relative momentum. The implications of this result on the halo neutron correlation will be discussed in a later section (Momentum Distributions), but it can be concluded here that the enhancement observed at low q in this work was due to cross-talk contamination that could not be rejected by the kinematical procedure presented in the beginning of this section. It should be noted this procedure using the $^{7}Li(p,n)$ reaction data was used to construct the n-n correlation function presented in a previous article [16].

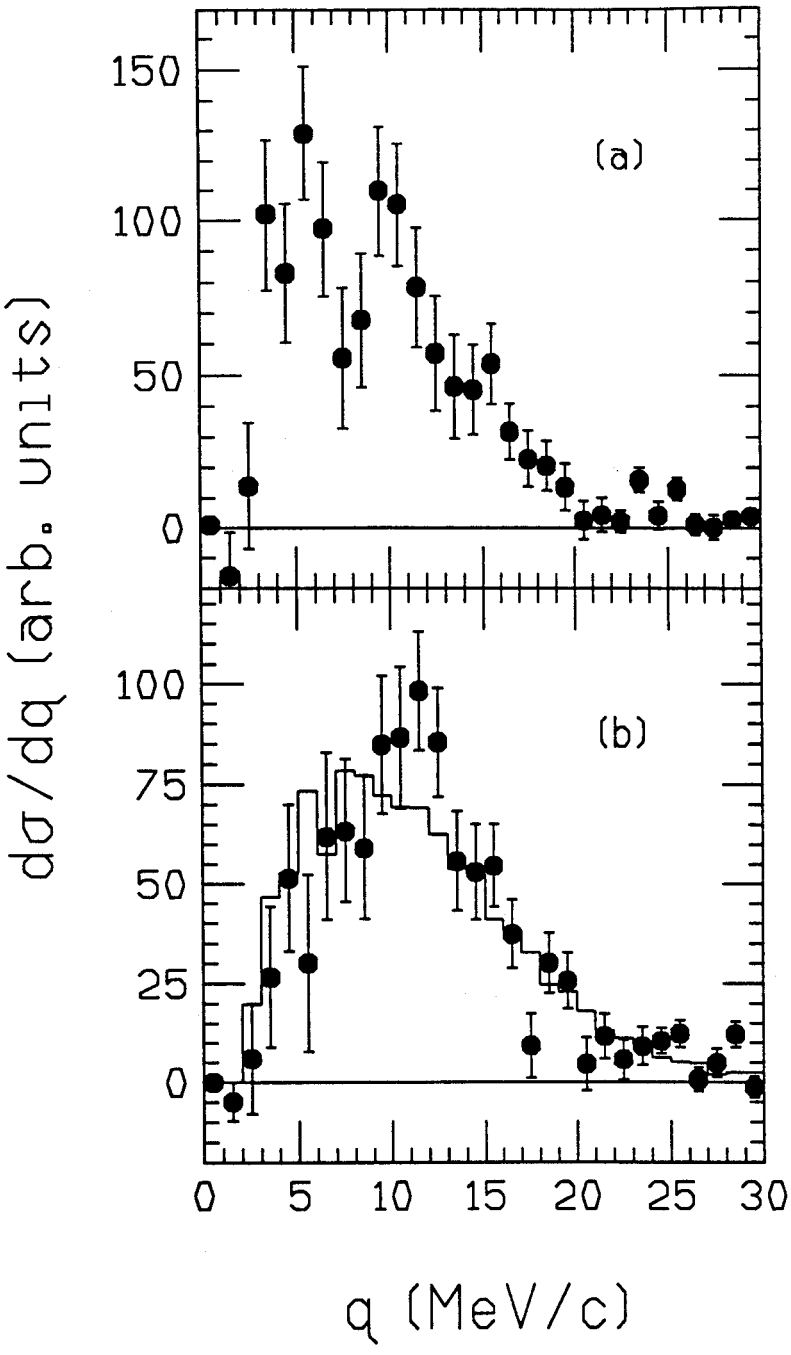

Figure 2.4: A n-n relative momentum spectrum from the ^{11}Li data. (A) before subtracting the cross-talk background measured from the ^{7}Li(p,n) experiment. (b) After subtracting the cross-talk contamination. The histogram is the prediction of a 3-body phase space simulation discussed in Section 5.4

Chapter 3

Telescope Data

Before proceeding to the main focus of this work, the 2n-^{9}Li events, results from the fragment singles measurement are presented in this section and results from the 1n-^{9}Li measurements are discussed in the next section. The telescope counted the total numbers of both ^{9}Li nuclei produced and ^{11}Li nuclei which did not react. In addition, the number of incident ^{11}Li was determined from the beam TOF measurement. From this information, the two-neutron removal cross section σ_{2n} (^{11}Li $\rightarrow$ ^{9}Li + 2n) and the total reaction cross section σ_{tot} for ^{11}Li + Pb at 28 MeV/nucleon were determined. Before presenting the results and comparing to other work, a description of the analysis technique is presented.

A ΔE-E plot for ^{11}Li and ^{9}Li is shown in Figure 3.1a. The distinction between ^{11}Li and ^{9}Li is blurred due to ^{11}Li dissociation that occurs in the CsI. When dissociation occurs in the CsI, the energy signal is a sum of the ^{11}Li energy loss before dissociation and the remaining ^{9}Li energy after dissociation, since the neutrons in general do not deposit any energy. Therefore, the energy signal is greater than that of a ^{9}Li nucleus that enters the CsI, but less than that of a non-dissociating ^{11}Li . ^{11}Li may also dissociate in one of the silicon ΔE detectors (2x300 μm thick). For these events, the resulting ^{9}Li signal appears in the same location on the ΔE-E plot as ^{9}Li dissociations that occurred in the lead target. Dissociation in the detector thus

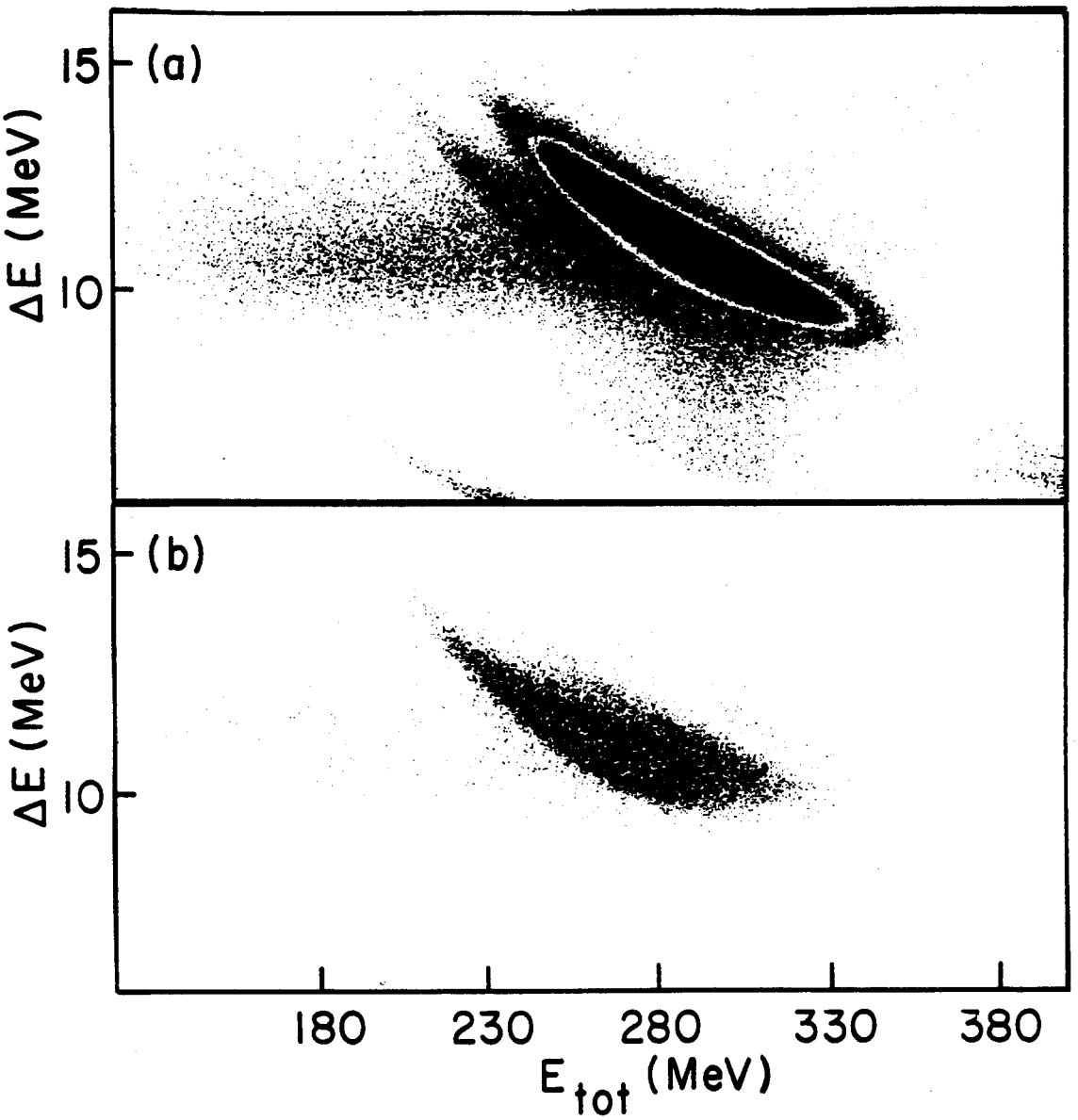

Figure 3.1: (a) Two dimensional ΔE-E plot for the fragment singles events. Only the region around the ^{9}Li and ^{11}Li is shown. (b) A similar plot, but requiring at least one neutron in coincidence with the ^{9}Li fragment.

makes particle identification ambiguous and generates some ^{9}Li events that appear to come from reactions with the target.

In order to accurately subtract the contribution due to reactions in the telescope, data was also taken with the target removed and the beam energy lowered to compensate for energy loss in the target. The ^{11}Li beam energy was reduced by inserting an aluminum degrader to S1. The energy loss of the aluminum degrader was identical to that of the target, so the ^{11}Li energy striking the detector was the same as in the target-in runs. For any spectrum, a subtraction of target-out data from target-in data yields data representing ^{11}Li reactions in the target. From the ΔE-E spectrum shown in Figure 3.1a, a linearized two-dimensional spectrum of particle identification number (PID) versus E_{CsI} was made using the relation PID = $E_{tot}^{1.795} - E_{CsI}^{1.795}$. Here, E_{tot} is the sum of the Si and CsI energy signals in MeV and E_{CsI} is the energy deposited in the CsI detector alone. Projecting onto the PID axis, a one-dimensional PID spectrum was made for both target-in and target-out data. These projections are shown in Figure 3.2a. The peak around channel 1000 is from the ^{11}Li beam. The spectrum for the target-out runs has been normalized to the target-in runs for the same number of incident ^{11}Li . Figure 3.2b shows the result of the subtraction of the two spectra in Figure 3.2a. The ^{9}Li peak appears at PID=880, although with a considerable asymmetry. An over-subtraction and an under-subtraction occur for the ^{11}Li data between PID=950 and 1150. It is important to be sure that both the asymmetry in the ^{9}Li peak as well as the over-subtraction and under-subtraction in the ^{11}Li region are not due to a flaw in the subtraction procedure.

The over-subtraction and under-subtraction between PID=950 and 1150 is most likely caused by differences in the beam energy distributions, although the average beam energies were equal. The energy loss in the aluminum degrader used in the target-out runs was equal to that in the lead target, but the Al degrader was used

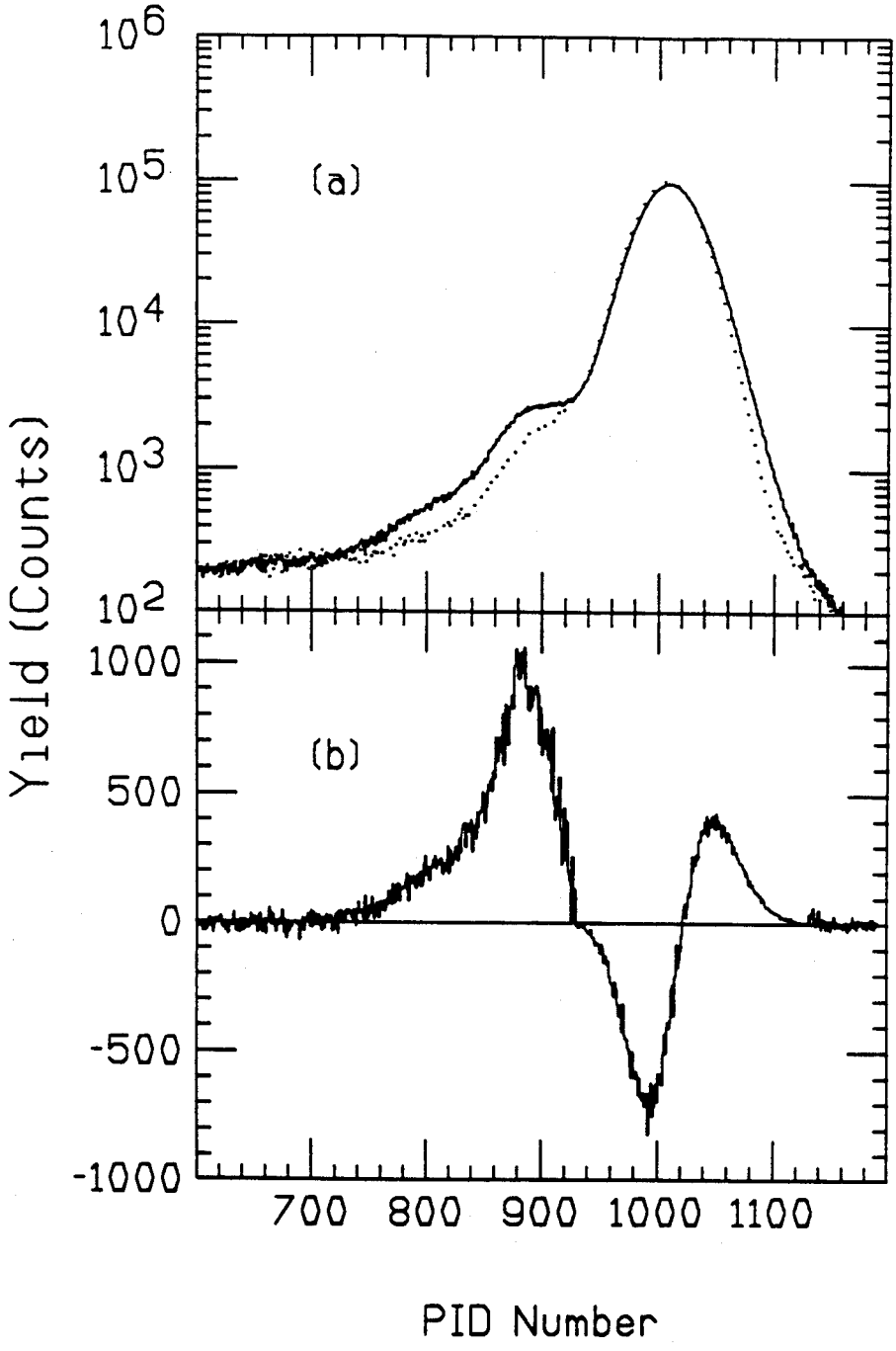

Figure 3.2: (a) A one-dimensional particle identification spectrum for target-in data (solid histogram) and target-out data (dashed histogram). (b) The subtracted result. The ^{9}Li peak is near PID=880. The under-subtraction and over-subtraction have been downscaled by a factor of ten for plotting purposes.

before a final dipole magnet. The rigidity of the ^{11}Li beam for the target-out data was modified by the Al degrader, so a different beam energy distribution was produced at the telescope due to the acceptance of the final dipole magnet. One verification that the subtraction procedure was correct comes from examining the ^{11}Li region shown in Figure 3.2a. The amount of ^{11}Li in the peak region for the target-in data, N_{11}(in), represents the number of ^{11}Li nuclei that are transmitted through the target and telescope without reacting. For the target-out data, the number of ^{11}Li in the peak region, N_{11}(out), represents the number of ^{11}Li nuclei transmitted through the telescope without reacting. Because more flux is removed by the target-plus-telescope than the telescope only, $N_{11}(\text{in}) < N_{11}(\text{out})$, and the difference $N=N_{11}(\text{in}) - N_{11}(\text{out})$ should be negative. Figure 3.2 shows clearly that N is negative. This is one indication that the subtraction procedure is valid, even though the beam energy distributions for the target-in and target-out data sets were slightly different. The number N was determined by integrating the PID spectrum shown in Figure 3.2b from PID=930 up 1200. The result is $N=-118,000$, and the magnitude of N amounts to 1.7% of the total incident ^{11}Li . The absolute value of N is the amount of incident ^{11}Li removed by the Pb target.

The tail on the ^{9}Li peak was assumed to be caused by reactions between ^{11}Li and Pb other than the two-neutron removal channel. For example, the reaction $^{11}\text{Li} \rightarrow {}^{8}\text{Li} + 3\text{n}$ would appear at about PID=790. A more complex reaction yielding an α-particle plus ^{6}He, both hitting the CsI(Tl) detector, would appear near PID=850. These reaction products and events from other fragmentation reactions with similar PID values would not be subtracted by the target-out data.

From the subtracted PID spectrum in Figure 3.2b, both the two-neutron removal cross section σ_{2n} and the total interaction cross section σ_{tot} for ^{11}Li on Pb can be determined at 28 MeV/nucleon. Fitting the ^{9}Li peak with a Gaussian gives $\sigma_{2n} = 5.1 \pm 0.3$

barns. The error arises from extracting a symmetrical peak from the asymmetric peak-plus-tail region. The measurement can be compared with the result of Anne *et al.* [32]. They found σ_{2n} =5.0±0.8 barns for the dissociation of ^{11}Li projectiles on a Au target at 29 MeV/A. They used a silicon telescope for particle identification and also performed a subtraction of target-out data from target-in data. Assuming mostly Coulomb dissociation, their result can be scaled by 1.08 to account for the slight difference in target and beam energy. The 1.08 scaling factor was estimated based on the measured target charge (Z_T) dependence of Coulomb excitation, $Z_T^{1.4}$ [9], and an the inverse beam energy dependence of the Coulomb dissociation cross section [18]. The scaled cross section is σ_{2n} =5.4±0.9 barns, in good agreement with the result from this work. The agreement is an indication that the ^{9}Li peak has been correctly extracted from the asymmetric ^{9}Li tail-plus-peak region.

The total reaction cross section for ^{11}Li + Pb was also determined. The number of ^{11}Li that traversed the Pb target without reacting, |N|, was measured from by the Si/Csi(Tl) telescope. A total of 1.7% of the incident ^{11}Li beam was removed by the Pb target, yielding a total reaction cross section σ_{tot} =9.7 ± 0.7 barns. The principal source of the uncertainty arises from a difficulty in determining N_0. The beam TOF measurement that yielded N_0 required a start signal in the first ΔE detector of the telescope. However, there were some reactions between the ^{11}Li and the Pb target that produced fragments at angles greater that 9°, and these fragments missed the telescope. For events where a fragment did not strike the telescope, the beam TOF could not be determined and therefore the incident ^{11}Li particles could not be counted for these events.

Our result for σ_{tot} can be compared to the results from Villari *et al.* [30]. They have measured the total reaction cross sections for several neutron-rich nuclei on silicon, including ^{11}Li + Si at 25.5 MeV/nucleon and have provided a parameterization of σ_{tot}

fitted over an energy range of 30-200 MeV/nucleon, a projectile nucleus range of A=1 to 40, and a target nucleus range of A=9 to 209. Using their parameterization yields a total nuclear reaction cross section of 5.7 $\pm$ 0.7 b. This cross section represents the total reaction cross section less the Coulomb dissociation cross section, since the parameterization given in ref. [30] does not include a scaling term for Coulomb excitation. Adding an extracted Coulomb dissociation cross section of 3.8 $\pm$ 0.8 b [40] yields a total reaction cross section σ_{tot} = 9.5 $\pm$ 1.1 b, in good agreement with our result. A somewhat less quantitative comparison can also be made to a result of Blank *et al.* [31], which yielded 7.23 $\pm$ 0.78 barns for ^{11}Li + Pb at an average ^{11}Li energy of 70 MeV/nucleon. Because the Coulomb dissociation component of σ_{tot} is expected to increase by a factor of 70/28 (= 2.5) at our beam energy [18], the two measurements are probably in agreement. Thus it is reasonable to conclude that the target-in and target-out subtraction procedure for the telescope data yields reliable results for both σ_{2n} and σ_{tot}. The results for σ_{2n} and σ_{tot}, as well as cross sections determined from the coincidence measurements, are summarized in Table 3.1.

Table 3.1: Compilation of cross sections from the telescope data, the 1n-^{9}Li data, and the 2n-^{9}Li data. The total two-neutron removal cross section is given by σ_{2n} and σ_{1n} is the total neutron cross section from the integrated neutron angular distribution. The cross sections for Coulomb and nuclear dissociation are denoted by σ_c and σ_{nuc}, respectively. B(E1) is the total strength and σ_{E1} is the photonuclear cross section, determined from the two-neutron ^{9}Li coincidence data. The quantity $^a\sigma_{nuc}$ was calculated in ref. [40] and $^b\sigma_c$ was determined from the difference between σ_{2n} and $^a\sigma_{nuc}$.

Data set	Quantity	Value
Telescope data	σ_{2n}	5.1 ± 0.3 b
	σ_{tot}	9.7 ± 0.7 b
1n-^{9}Li data	σ_{1n}	8.3 ± 0.5 b
	σ_c	3.2 ± 0.6 b
	σ_{nuc}	1.9 ± 0.7 b
2n-^{9}Li data	σ_c	3.6 ± 0.4 b
	B(E1)	1.00 ± 0.11 e^{2}fm^2
	total σ_{E1}	4.1 ± 0.5 mb
	$^a\sigma_{nuc}$	1.2 b
	$^b\sigma_c$	3.9 ± 0.3 b

Chapter 4

One-neutron ^{9}Li Coincidence Results

In this section a measurement of the neutron energy and angular distributions is presented and the results are discussed in light of previous measurements of the neutron angular distribution and ^{9}Li transverse momentum distribution from ^{11}Li breakup.

The ΔE-E spectrum for fragment-neutron coincidence events is shown in Figure 3.1b. The coincidence requirement eliminated the unreacted ^{11}Li from the spectrum. The events shown are due to ^{11}Li breakup in the target, silicon ΔE detectors and CsI. It is not possible to draw a gate that eliminates events where dissociation occured in the detector but preserves events where dissociation occured in the target. Therefore, all coincidence events were used, and, as with the fragment singles data, a target-in, target-out subtraction was performed.

The neutron energy distributions for target-in and target-out are shown in Figure 4.1a. The target-out data have been normalized to the target-in data by the total number of incident ^{11}Li nuclei. The lower-energy neutrons were produced by neutrons coming from ^{11}Li projectiles that lost energy in the silicon and CsI before dissociating. The result of the subtraction is shown in Figure 4.1b. A surprising feature is that the mean energy of the neutrons, 26.9 ± 0.3 MeV, is lower than both the mean ^{9}Li energy

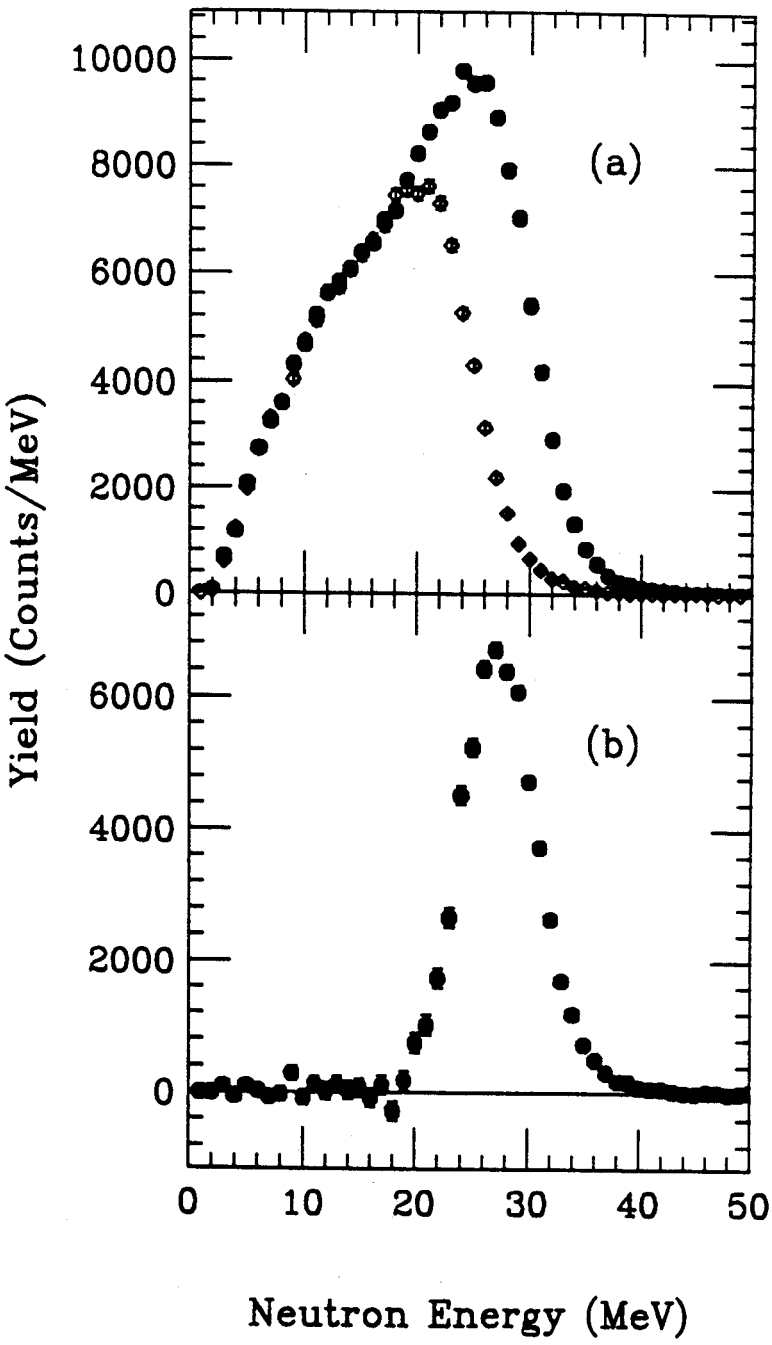

Figure 4.1: Neutron energy distributions for target-in (solid points) and target-out (open points) data are shown in (a). The low energy portion is due to ^{11}Li dissociation in the CsI. The subtracted result, showing the neutron energy distribution due to the Pb only, is shown in (b).

and the incident beam energy, 28.3 ± 0.4 MeV/nucleon and 28.0 ± 0.4 MeV/nucleon, respectively, after correcting for the energy loss in the target. This effect will be discussed in more detail in the section on post breakup Coulomb acceleration.

The neutron angular distribution could be constructed for angles between 0.5 ° and 4.8 °. The spectrum was corrected for neutron detector efficiency and for attenuation of neutrons by half the lead target thickness, the silicon-CsI telescope, three mm of aluminum at the back of the target chamber, a 6 mm plastic veto paddle, and several meters of air. The angular distribution is given by the solid points in Figure 4.2. The open diamonds in Figure 4.2 are data taken from Anne *et al.*[32] for ^{11}Li + Au at 29 MeV/nucleon and scaled to our conditions by a factor of 1.08.

This forward-peaked angular distribution was produced by the projectile fragmentation of ^{11}Li into ^{9}Li and two halo neutrons by the Coulomb and nuclear field of the target. The momentum distribution of fragments of mass A from the fragmentation of stable projectiles is well described by a Gaussian function $d^3\sigma/dp^3 \propto e^{-p^2/2\sigma_A^2}$ in the rest frame of the projectile. The width σ_A has been parameterized with a single parameter, $\sigma_0 \approx 70 - 90$ MeV/c, in the Goldhaber model [3] for many different projectile and fragment combinations. However, ^{9}Li transverse momentum distributions have been measured [2, 9] and very narrow distributions, corresponding to $\sigma_0 = 16$ MeV/c, were required to reproduce the data. Similar results for the narrow component for ^{9}Li parallel momentum distributions have also recently been reported [34]. The narrow width is understood to originate from the removal of the weakly-bound halo neutrons, which gives a small recoil to the ^{9}Li fragment. The narrowness of the ^{9}Li transverse momentum distribution reflects the small spread in the Fermi momentum of the halo neutrons.

The neutron angular distribution was also fitted by the Gaussian distribution in the Goldhaber model. In the laboratory reference frame, in terms of perpendicular

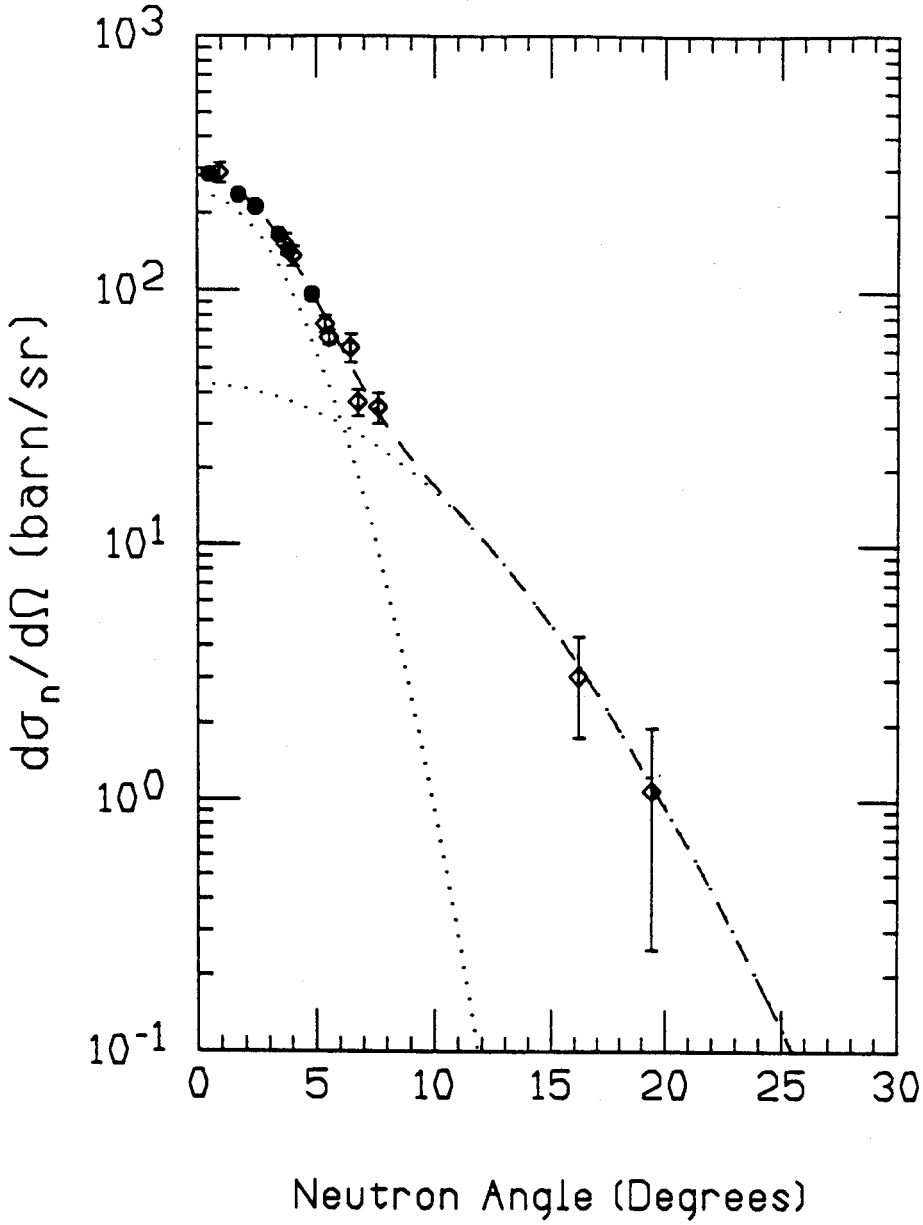

Figure 4.2: Measured angular distribution for ^{11}Li + Au at 29 MeV/nucleon taken from [32] is shown with the open diamonds. The solid points represent the angular distribution for ^{11}Li + Pb at 28 MeV/A (this work). The dotted lines are fits using narrow and broad gaussians. The dashed line is the sum of both components.

($p_\perp$) and parallel ($p_{||}$) momentum components, the momentum distribution becomes:

$$\frac{d^3\sigma}{dp^3} = N \exp^{-(p_\perp^2 + (p_{||}-p_0)^2)/2\sigma_A^2} \tag{4.1}$$

Here, N is a normalization factor, p_0 is the average projectile momentum per nucleon, σ_A is the width parameter and θ is the laboratory angle of the neutrons. Using $p_{||} = p\cos\theta$, $p_\perp = p\sin\theta$, and $dp^3 = p^2 dp d\Omega$, the angular distribution is given by:

$$\frac{d\sigma}{d\Omega} = N \exp^{-p_0^2 \sin^2\theta/2\sigma_A^2} \int_0^\infty p^2 \exp^{-(p-p_0\cos\theta)^2/2\sigma_A^2} dp \tag{4.2}$$

$$\approx N \cos^2\theta \exp^{-p_0^2 \sin^2\theta/2\sigma_A^2} \tag{4.3}$$

The normalization factor N and the width parameter σ are fitting parameters. To reproduce the neutron angular distribution, a sum of a narrow ($\sigma_A = \sigma_{nar}$) and a broad ($\sigma_A = \sigma_{br}$) component were used, with each component given by Eqn. 4.3. The combination of our data and the data from [32] was used for the fitting. The results of the fitting are shown in Figure 4.2. The dotted curves are for the narrow and broad components and the dashed line is the sum of the two components. The width parameters are σ_{nar} =11.8 ± 0.8 MeV/c and σ_{br} =28 ± 1 MeV/c. The errors were determined by the change in the value of each parameter required to increase χ^2 by one, with all other parameters fixed at their optimum values [35]. Both σ_{nar} and σ_{br} must be corrected for Coulomb deflection of the ^{11}Li projectile. For Coulomb dissociation, assuming an average impact parameter of 20 fm [36] and assuming the breakup occurs at the distance of closest approach between target and projectile, 20.6 fm, the Coulomb deflection angle is 1.6 ° , yielding a width of σ_{coul} = 6.6 MeV/c. Subtracting this width (in quadrature) from σ_{nar} above yields σ_{nar} corrected for Coulomb deflection of the ^{11}Li projectile, σ_{nar} =9.8 ±0.1 MeV/c.

The integrated neutron angular distribution yielded a total neutron cross section of σ_{1n}=8.3 ± 0.5 barns. The integrated cross section can be interpreted in terms

of nuclear and electromagnetic effects and compared to recent calculations of the Coulomb and nuclear dissociation cross sections. Since the equivalent photon spectrum decreases sharply with energy [18], both neutrons, when liberated via Coulomb excitation, will have little excess energy and will tend to be emitted at forward angles in the laboratory. Hence the multiplicity resulting from Coulomb dissociation, m_c, should be $m_c \approx 2$. There will also be nuclear dissociations that produce ^{9}Li and two neutrons where either halo neutron in ^{11}Li may be scattered or absorbed in the Pb target. The absorption mechanism for the halo neutrons can be thought of in terms of the Serber model [37], where for ^{11}Li , a halo neutron may be absorbed by the Pb target. The projectile remnant, ^{10}Li , is unbound and decays to a ^{9}Li plus a neutron. Because of the low decay energy of ^{10}Li , 150 keV [38] or 800 keV [39], the neutron from ^{10}Li decay would appear at forward angles. Another possibility is the scattering of a halo neutron by the Pb target, also leaving a ^{10}Li fragment. Thus for the combined absorption and scattering mechanisms, if scattering produces a broad angular distribution of neutrons, the nuclear dissociation mechanism would produce both a broad and a narrow neutron angular distribution of neutrons. Because the neutron angular distribution only covers the forward 20 ° , much of the broad angular distribution would be unobserved. Therefore, the observed neutron multipliciy for nuclear dissociation would be $m_{nuc} \approx 1$.

Using the integrated cross section from the neutron angular distribution, $\sigma_{1n} = 8.3 \pm 0.5$ barns, which can be considered a multiplicity-weighted sum of Coulomb and nuclear dissociation, and the two-neutron removal cross section σ_{2n} from the fragment singles measurement, $\sigma_{2n} = 5.1 \pm 0.3$ barns, the Coulomb (σ_c) and nuclear (σ_{nuc}) dissociation cross sections for ^{11}Li $\rightarrow$ ^{9}Li +2n were estimated by the following relations:

$$\sigma_{2n} = \sigma_c + \sigma_{nuc} \tag{4.4}$$

$$\sigma_{1n} = m_c\sigma_c + m_{nuc}\sigma_{nuc} \tag{4.5}$$

The solution of these equations, with m_c =2 and m_{nuc} =1, yields σ_c =3.2± 0.6 barns and σ_{nuc} =1.9± 0.7 barns. These results are listed in Table 1. The cross section σ_{nuc} has been calculated for 30 MeV/nucleon ^{11}Li + Au using a diffractive eikonal model [40]. The result, σ_{nuc} =1.2 barns, is expected to increase slightly for a lead target and agrees with our result of $\sigma_c = 1.9 \pm 0.7$ b. Subtracting the calculated σ_{nuc} =1.2 b from σ_{2n} yields σ_c =3.9 ±0.3 b, in agreement with $\sigma_c = 3.2 \pm 0.6$ determined here. Also, a recent calculation for ^{11}Li plus Au at 29 MeV/nucleon found that Coulomb dissociation accounts for up to 80% of the total two-neutron removal cross section [41]. The cross sections for σ_c and σ_{nuc} from Eqns. 4.4 and 4.5 indicate that $63 \pm 16\%$ of the two-neutron removal cross section is due to Coulomb dissociation, in agreement with the calculation.

Chapter 5

Two-Neutron–^{9}Li Coincidence Results

The primary goals of this experiment were to measure the dipole strength distribution $dB(E1)/dE$ and the photonuclear cross section $\sigma_{E1}(E)$, and to determine the ^{9}Li momentum distributions in the ^{11}Li rest frame in order to better understand the structure of ^{11}Li . The spectra for $dB(E1)/dE$ and σ_{E1}(E) may provide the best evidence for the predicted soft dipole resonance. The momentum distributions will yield information on how the excitation energy is distributed between the ^{9}Li and the neutrons, which may provide information about the degree of correlation between the halo neutrons and possibly evidence for a dineutron structure. In Section 5.1 the technique used to determine the ^{11}Li excitation energy event-by-event is discussed and in Section 5.2 the results for $dB(E1)/dE$ and σ_{E1}(E) and comparisons to some calculations are presented. In Section 5.3 ^{9}Li and neutron velocity distributions are displayed. The impact of these velocity distributions on the interpretation of the soft dipole resonance will be discussed. Finally, in Section 5.4, ^{9}Li and neutron momentum distributions, determined in the ^{11}Li rest frame, are given. The structure of the ^{11}Li nucleus will be discussed in light of these distributions.

5.1 The Decay Energy Spectrum

The excitation energy E was determined by measuring the ^{11}Li decay energy, E_d . The excitation energy is related to the decay energy by E=E_d +S_{2n}, where S_{2n} is the two-neutron separation energy of ^{11}Li . In the rest frame of the excited ^{11}Li , the decay energy can be expressed as:

$$E_d = \frac{1}{2}\mu_1 \vec{V}^2_{2n-9} + \frac{1}{2}\mu_2 \vec{V}^2_{n-n} \tag{5.1}$$

$$\text{with } \mu_1 = \frac{m_9(2m_n)}{m_9 + (2m_n)} \text{ and } \mu_2 = \frac{m_n}{2} \tag{5.2}$$

Here, $\vec{V}_{2n-9}$ is the relative velocity between the ^{9}Li and the two neutron center of mass, $\vec{V}_{n-n}$ is the relative velocity between the two neutrons in the rest frame of the two-neutron center of mass, m_9 is the ^{9}Li mass and m_n is the neutron mass. The relative velocities are measured in the laboratory reference frame and Lorentz transformed to the ^{11}Li rest frame. For our beam energy, the relative velocities are nearly frame invariant, so the Lorentz transform alters the relative velocities <2%. The decay energy was calculated and the decay energy spectrum was constructed from the 2n-^{9}Li events. Figure 5.1a,b displays the measured decay energy spectrum for target-in and target-out runs. Approximately 50% of the events are due to dissociation in the Si/CsI telescope. The peak at low decay energies for the target-in data indicates the abundance of events arising from Coulomb dissociation in the Pb target. The subtracted spectrum, representing ^{11}Li decay events in the Pb target, is displayed in Figure 5.1c.

Because both electromagnetic and nuclear interactions may contribute to the decay energy spectrum shown in Figure 5.1c, it is important to understand the magnitude of the nuclear contribution in order to accurately calculate the E1 strength

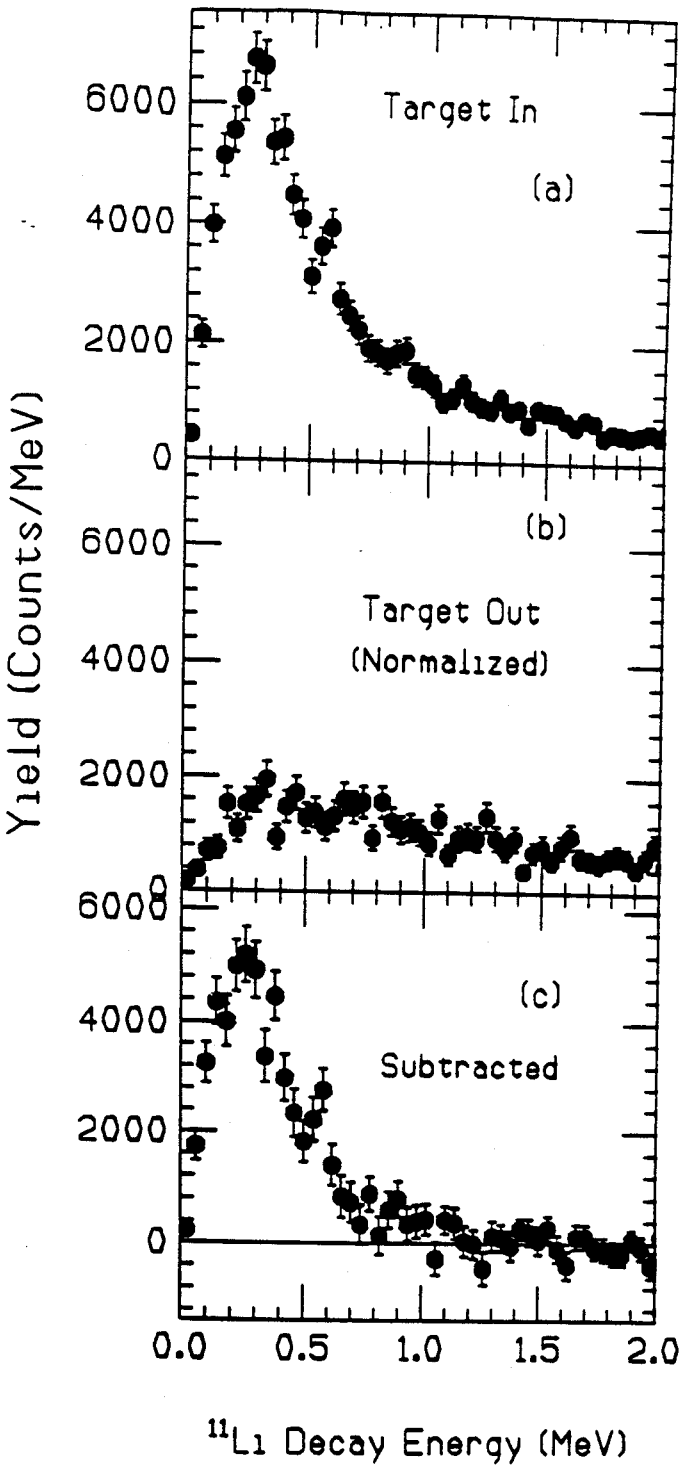

Figure 5.1: Decay energy spectrum for (a) target in, (b) target out, and (c) the subtracted result. The target out data result from ^{11}Li dissociation in the silicon detectors and the CsI detector.

function. Recent theoretical calculations show that electromagnetic effects contribute up to 80% of the total dissociation cross section for high Z targets[41] and projectiles near 30 MeV/nucleon, in agreement with the Coulomb and nuclear cross sections determined from the 1n-^{9}Li events, $\sigma_c = 3.2 \pm 0.6$ barns and $\sigma_{nuc} = 1.9 \pm 0.7$ barns. For nuclear dissociation mechanisms like those described in the previous section, requiring two neutrons to be detected at less than 5 ° would further enhance the number of events from electromagnetic dissociation relative to nuclear dissociation.

An investigation of the contribution from nuclear dissociation was performed. Coulomb excitation is largely a peripheral process, occurring at impact parameters $b > b_{min}$, and at an average impact parameter of about 20 fm [36]. Here b_{min} is the impact parameter corresponding to the grazing angle. Using a matter radius of 3.3 fm [1] for ^{11}Li and a Pb radius of 7.1 fm yields $b_{min} = 10.1$ fm. Nuclear dissociation, where the halo neutrons are scattered or absorbed by the Pb target, occurs for impact parameters $b \approx b_{min}$. Because of the complete kinematic measurement, an approximate impact parameter could be determined for each event. A decay-energy spectrum was constructed consisting only of events with b> 15 fm. In this case the decay energy spectrum is expected to be free of contamination from nuclear dissociations. The impact parameter was determined for each event from the change in the velocity vector of the center of mass before and after breakup, since the Coulomb deflection alters the center of mass velocity. The center of mass velocity after breakup was determined from the measured momenta of the ^{9}Li and two neutrons. The incident ^{11}Li velocity was measured by TOF and the PPAC's. The recoil of the Pb was neglected in this analysis. The decay energy spectrum, gated on events for b> 15, is shown in Figure 5.2. The decay energy spectrum for all events (no gating) was shown in Figure 5.1c. Although the magnitude of the gated spectrum is reduced by 25%, the shape of the two spectra agree within statistical uncertainties. Also, it is

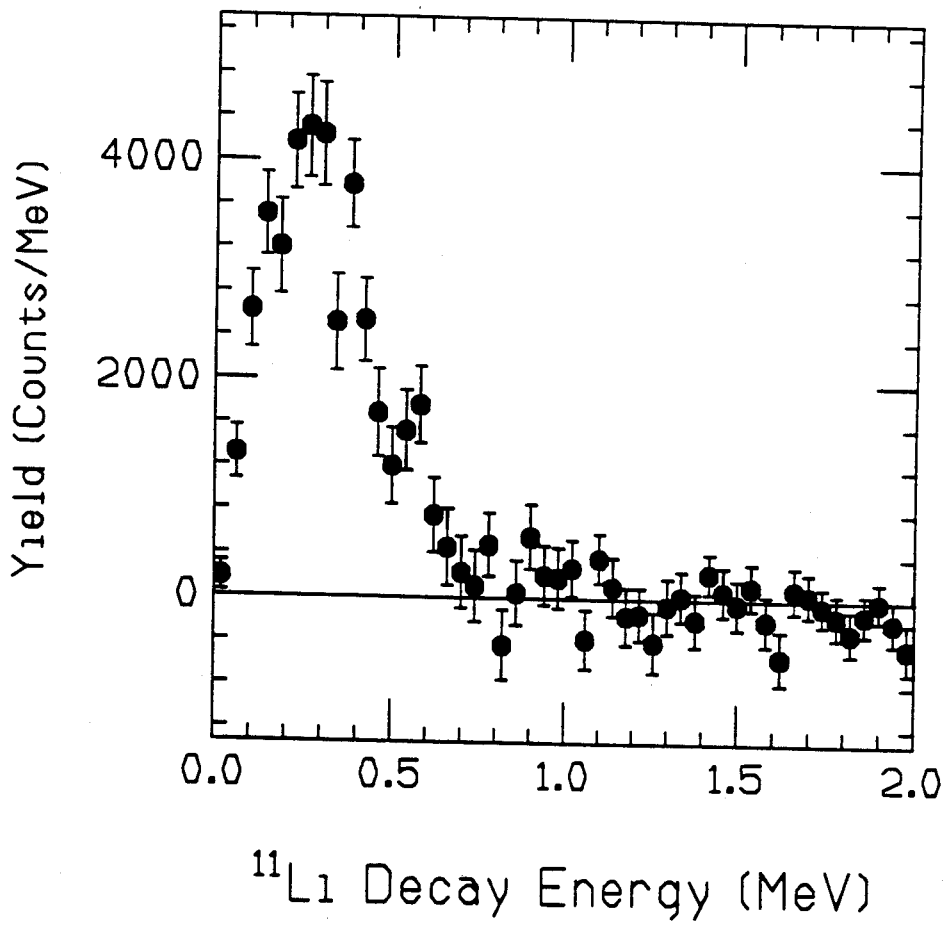

Figure 5.2: Decay energy spectrum gated on impact parameter, for b> 15 fm.

not known how many of the events with b$\leq$ 15 fm were the result of Coulomb dissociation. Disentangling Coulomb and nuclear effects is difficult for b$\approx$ b_{min} because the Coulomb dissociation cross section increases considerably as b decreases, due to the increasing intensity of the equivalent photon spectrum [18]. It is quite possible that many of these events originated from Coulomb dissociation. Therefore, the data from the ungated decay energy spectrum was used, with the knowledge that events from nuclear dissociation were not numerous enough to affect the shape of the spectrum, but that the integrated spectrum may overestimate the number of events from Coulomb dissociation and hence the magnitude of the Coulomb dissociation cross section σ_c.

The decay energy spectrum was also corrected for the efficiency of the detection system. The efficiency for several decay energies was determined by a Monte Carlo calculation. An empirical fit to the calculated efficiency is show in Figure 5.3. The efficiency is mainly determined by the product of the geometric efficiency for both neutrons striking scintillator, and the intrinsic neutron detector efficiency, which is about 18% for each neutron, using a theshold corresponding to 3 MeV neutrons. The geometric efficiency is strongly decay-energy dependent, since large decay energies yield neutrons with higher transverse momenta, and these neutrons are more likely to miss the detector array.

Using the calculated efficiency, the ^{11}Li flux and the target thickness, the absolute Coulomb dissociation spectrum $d\sigma_c/dE$ was determined from the spectrum in Figure 5.1c. Integrating over energy yielded the total cross section, $\sigma_c = 3.6 \pm 0.4$ barns. This value is also listed in Table 3.1. The magnitude of σ_c determined here is consistent with σ_c determined from the 1n-^{9}Li data (σ_c =3.2$\pm$0.6 b) and from σ_c determined from the difference $\sigma_c = \sigma_{2n} - \sigma_{nuc} = 3.9 \pm 0.3$ b, where σ_{2n} =5.1$\pm$0.3 b was measured with the telescope, and σ_{nuc} =1.2 b from a calculation [40]. The

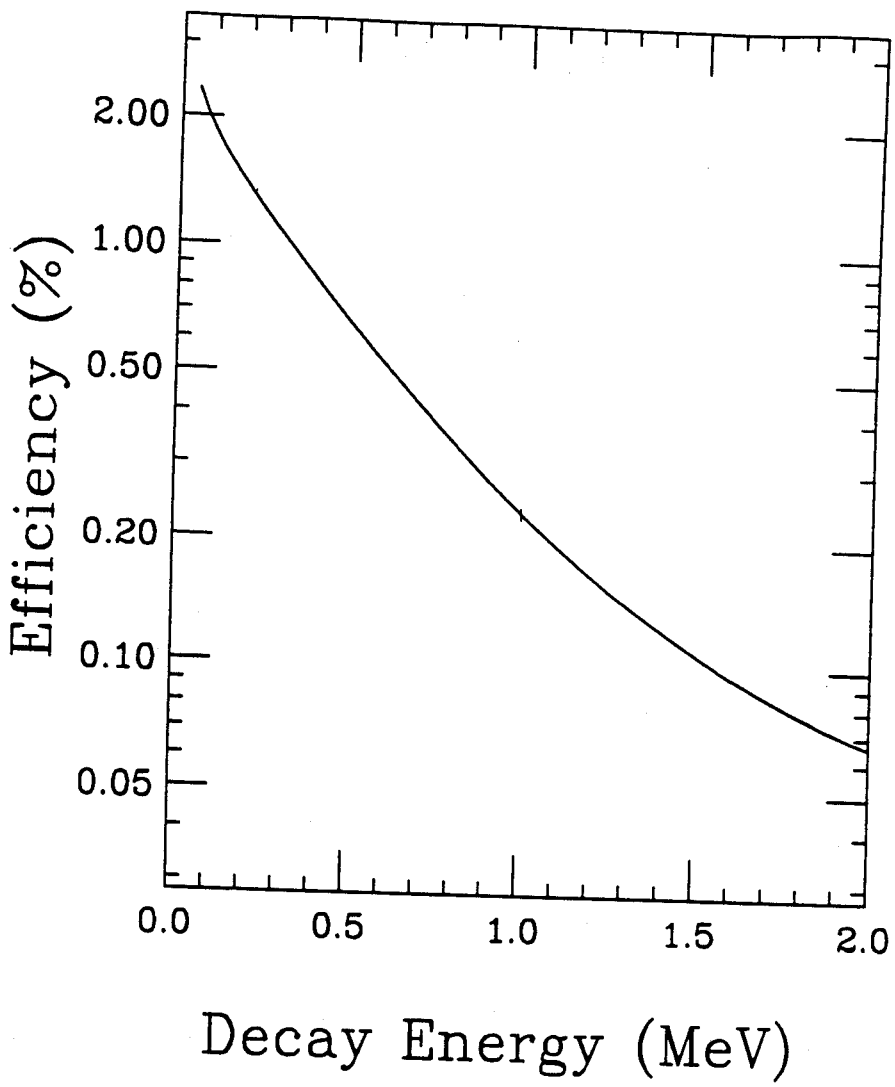

Figure 5.3: Detection efficiency as a function of decay energy.

statistical accuracy of the decay energy spectrum shown in Figure 5.1c is quite low for $E_d > 0.7$ MeV, and the spectrum is consistent with zero for $E_d > 1$ MeV. These features are reflected in the detector efficiency in Figure 5.3, where the efficiency decreases by an order of magnitude for E_d between 0.1 and 1.0 MeV. However, because σ_c determined from the decay energy spectrum is consistent with the values obtained from the fragment singles and from the 1n-^{9}Li data, it is unlikely that a significant portion of the decay energy spectrum was not observed due to low statistical accurracy or a cutoff imposed by the detector apparatus. This will also be important when the strength function and photonuclear cross section are calculated and presented in the next section.

5.2 $dB(E1)/dE$ and σ_{E1}(E)

The measured decay energy spectrum $d\sigma_M/dE_d$, shown in Figure 5.1c, is related to the true spectrum $d\sigma/dE_d$ by the following:

$$\frac{d\sigma_M}{dE_d}(E_d) = \int \frac{d\sigma_c}{dE'_d}(E'_d)\,\varepsilon(E'_d, E_d)\,dE'_d \tag{5.3}$$

The function $\varepsilon(E'_d, E_d)$ represents the response of the detector system and dictates how much the true decay energy spectrum is distorted by detector induced biases. Often, $\varepsilon(E'_d, E_d)$ is a complicated function and unfolding such a response function, equivalent to performing the inverse transform of Eqn. 5.3, is quite difficult. The response function of the detection system was studied as a function of decay energy. Computer-generated events at a specific decay energy were fed through a simulated detector system to determine the resolution response. Neutron detector timing and angular resolutions (1 ns and 0.7°), ^{9}Li energy and angular resolutions (3 MeV and 0.6°), energy losses in the Pb target, and multiple scattering effects in the target were all considered. The results for decay energies of 100 keV, 500 keV and 1 MeV

are shown in Figure 5.4a-c, respectively. The width of the response function is shown in Figure 5.4d. Because of the tails in the response functions, FWHM is not an appropriate measure of width. Instead, starting from the centroid, the peak was integrated up to a distance ± s away from the centroid until the area equaled 76% of the total area of the peak. A width was then defined as 2s. For a Gaussian distribution 2s would be equivalent to FWHM.

Because of the complicated shape of the response function, it was not feasible to unfold the response from $d\sigma_M/dE_d$ directly. Therefore, model predictions were chosen for $d\sigma_c/dE_d$, filtered through a simulated detection system using a Monte Carlo program and compared to the measured decay energy spectrum. The filtering process folds in the effect of the response function $\varepsilon(E'_d, E_d)$ on the true spectrum. A search was performed for a model of the true spectrum that best reproduced the measured decay energy spectrum. As shown in Eqn. 1.4, $d\sigma_c/dE_d$ is a product of the photon spectrum $N_{E1}(E)$ and a photonuclear spectrum. Therefore, constructing model distributions of $d\sigma_c/dE_d$ requires a function for $\sigma_{E1}(E)$ to be chosen, since the photon spectrum is calculable.

An empirical model, in which $\sigma_{E1}(E)$ was parameterized with a Breit-Wigner function, provided the best reproduction of the data. The Breit-Wigner function is given by:

$$\sigma_{E1}(E_d) = \frac{\sigma_m \Gamma}{(E_d - E_0)^2 + (\Gamma/2)^2} \quad \text{and} \quad \Gamma = \frac{\Gamma(E_0)T(E_d)}{T(E_0)} \tag{5.4}$$

The function is written in terms of the decay energy E_d and the excitation energy $E = E_d + S_{2n}$, with S_{2n}=0.34 MeV. The centroid and width are denoted by E_0 and Γ, respectively, and σ_m is a normalization constant. The Breit-Wigner function included a transmission coefficient, denoted by T(E), with the energy dependence of s-wave neutrons. The transmission coefficient forces the Breit-Wigner shape to zero at

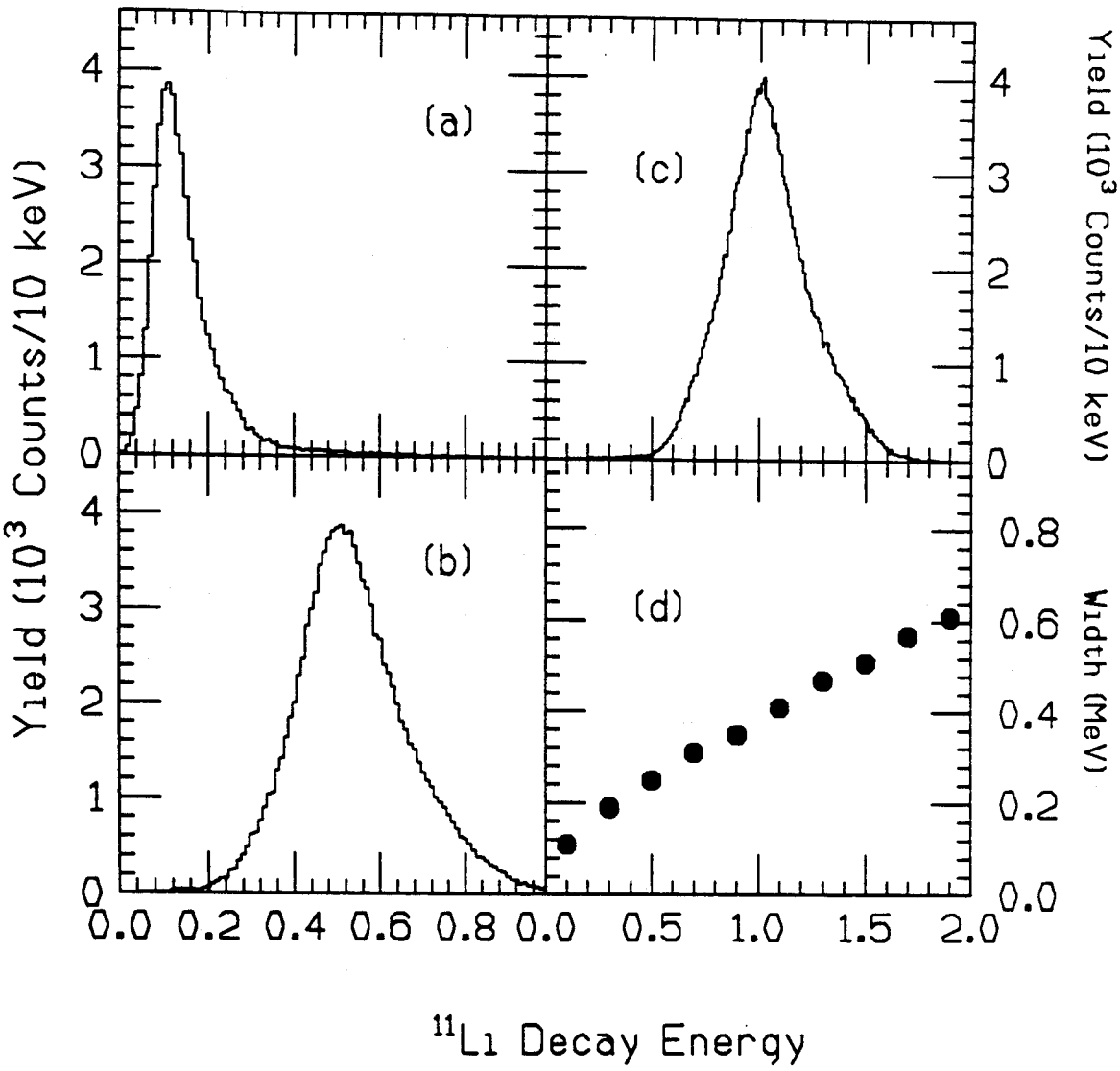

Figure 5.4: Experimental resolution for decay energies of 0.1 MeV, 0.5 MeV and 1.0 MeV is shown in a-c, respectively. The width (see text for definition) as a function of decay energy is shown in (d).

$E_d = 0$. The measured decay energy spectrum, shown in Figure 5.1, is shown again in Figure 5.5a, after summing some channels. The solid line represents the Breit-Wigner model with resonance parameters $E_0 = 0.7$ Mev and $\Gamma = 0.8$ MeV. The good fit of this function after being folded with the response function means that, to within our experimental errors, Eq. 5.4 represents our measured photonuclear spectrum.

Figures 5.5b,c show the measured photonuclear spectrum and dipole strength function, as determined from the fit to the data in Figure 5.5a. The strength function is determined from σ_{E1}(E) according to Eqn. 1.2. The integrated photonuclear cross section and dipole strength function is 4.1 ± 0.5 mb and 1.00 ± 0.11 e^2 fm^2. These values are listed in Table 3.1. It is important to emphasize that the distributions in Figure 5.5b,c were deduced from the true decay energy spectrum and therefore can be compared directly to theoretical calculations.

The narrow peak in the spectrum for σ_{E1}(E) ($\Gamma = 0.8$ MeV) and the location of the peak ($E_0 = 0.7$ MeV) are suggestive of a soft dipole resonance for ^{11}Li and in good agreement with the predictions of several calculations. Broadly speaking, the models of ^{11}Li excitation can be grouped into two categories. The first group assumes a direct breakup into ^{9}Li and two neutrons, while the second group considers the existence of a continuum resonant state in ^{11}Li that can be populated by E1 excitation, followed by breakup into a ^{9}Li and two neutrons. In the direct breakup picture, the absorbed photon induces a displacement of the ^{9}Li core relative to the halo and the restoring force provided by the halo is too weak to keep the ^{11}Li nucleus from dissociating into a ^{9}Li and two neutrons. Alternatively, in the resonant state picture, the restoring force is strong enough such that E1 excitation populates a vibrational mode between the ^{9}Li core and the halo neutrons. Using a direct breakup scheme, the resonance was originally predicted to exist at a mean decay energy of E_d =0.7 MeV [4]. Another direct breakup calculation, the cluster model [15], found the dipole strength function

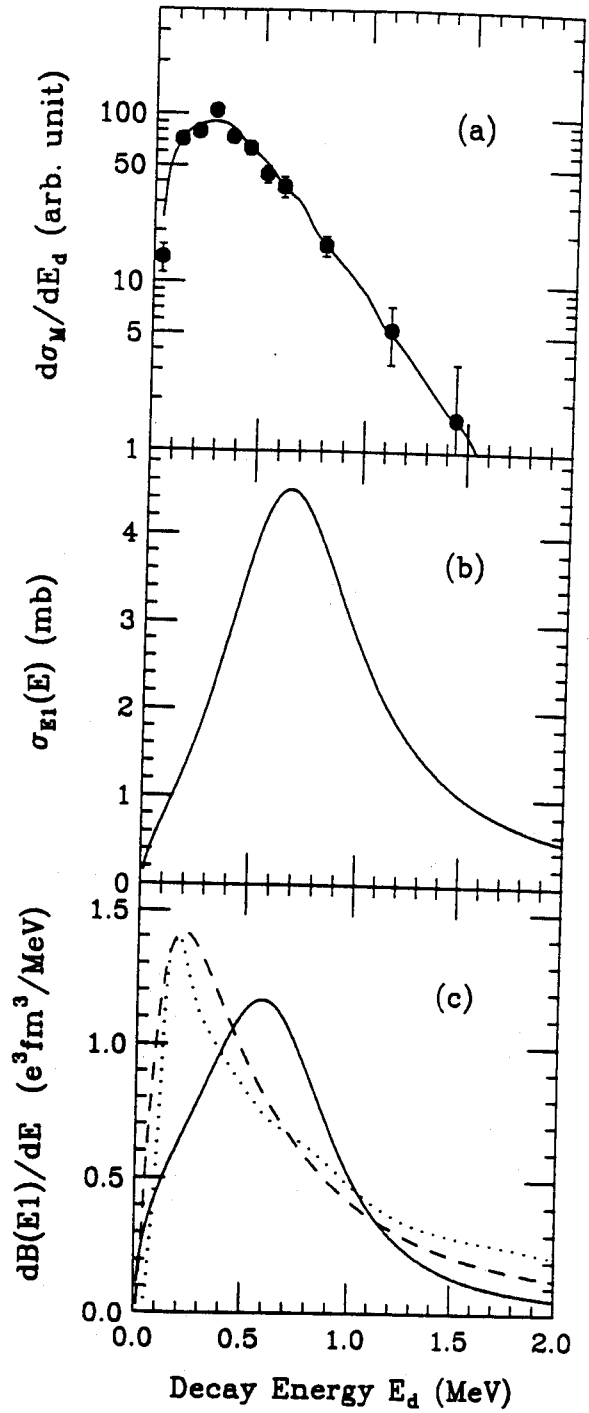

Figure 5.5: The decay energy spectrum. (a) The solid line is the product of a Breit-Wigner function with $E_0 = 0.7$ MeV and $\Gamma = 0.8$ MeV and the photon spectrum, after being filtered through the detector system. (b) The solid line is the photonuclear spectrum corresponding to the Breit-Wigner parameters determined from the data. (c) The solid line is the dipole strength function determined from the data. The dashed line is a calculation using a cluster model and the dotted line comes from a correlated 3-body calculation.

is sharply peaked near E_d=0.2 MeV. The dipole strength function predicted by this model is shown in Figure 5.5c by the dashed line. The total strength predicted by the cluster model is B(E1)= 1.34 e^2fm^2, close to the measured value of 1.00 ± 0.11 e^2fm^2 but the strength function peaks at a considerably lower energy. For the resonant state models, a correlated three body calculation [14] predicts a peak in the dipole strength function near E_d = 0.2 MeV also. The predited dipole strength function from this model is shown in Figure 5.5c by the dotted line. A model of the resonant state as a vibration between the halo neutrons and the ^{9}Li core predicted peaks at energies of E_0 = 0.5 MeV and E_{peak} = 2.5 MeV [10]. A calculation that modeled the SDR as a collective vibrational mode and was constrained to reproduce the measured Coulomb dissociation cross section found E_0 = 0.7 MeV and Γ = 0.7 MeV [9]. However, It was shown in a previous report [16] that the lifetime of a collective state with these parameters would only be 1/5 of an oscillation period. It is difficult to accept the concept of a collective vibrational state with this constraint.

It can be concluded that the photonuclear spectrum has a peak near a decay energy of 0.7 MeV and width of 0.8 MeV, but it is not possible, based solely on these data, to determine whether the breakup occurs directly or passes through a resonant state. The question of the nature of the breakup mechanism will be addressed in the following section.

5.3 Post-breakup Coulomb Acceleration

Some ^{9}Li and neutron velocity distributions provide the means to discriminate between a direct breakup and a resonant state picture for the excitation of ^{11}Li . Figure 5.6a shows the magnitude of the velocity difference $\Delta V = V_9 - V_{2n}$, where V_9 is the magnitude of the ^{9}Li velocity and V_{2n} is the magnitude of the average neutron

velocity for each 2n-^{9}Li event. The centroid of the distribution appears at 0.0090c ± 0.0003c, indicating the ^{9}Li is, on the average, more energetic than the neutrons.

Before interpreting the velocity difference, it is important to be sure that the result is not produced by detector biases or systematic errors in the energy and angle measurements. The former was investigated via Monte Carlo calculations. Computer-generated events with ΔV distributed about zero were fed through the simulated detector array. The result of the simulation, shown by the histogram in Figure 5.6a is peaked around zero, indicating instrumental biases are not causing the shift observed in the data. To check for systematic errors, overall momentum conservation could be verified since the complete kinematics were measured. Figure 5.6b displays the spectrum of counts versus the z-component of the center of mass velocity after breakup minus the z-component of the center of mass velocity before breakup. After breakup, the center of mass velocity is determined from the measured velocities of the ^{9}Li and both neutrons. Before breakup, the center of mass velocity is given by the measured energy and direction of the incident ^{11}Li . The z-components of velocity were used because the contribution from the Pb nucleus, which recoils close to 90 °, was negligible in this case. The near-zero centroid of the distribution, -0.0010c ± 0.0001c, showed momentum conservation is quite well enforced and provided a good check that the shift in the z-component of ΔV was not due to systematic error. The width of the distribution in Figure 5.6b yields the overall velocity resolution of the detection system, 0.008c FWHM.

It appears that the difference between the ^{9}Li velocity and average neutron velocity is a real effect, and it can be interpreted in terms of the breakup mechanism. Coulomb excitation is more likely to occur when the ^{11}Li projectile is close to the lead nucleus, due to the greater intensity of the photon spectrum [18]. If the breakup occurs soon after excitation, the ^{9}Li will be re-accelerated by the Coulomb field of

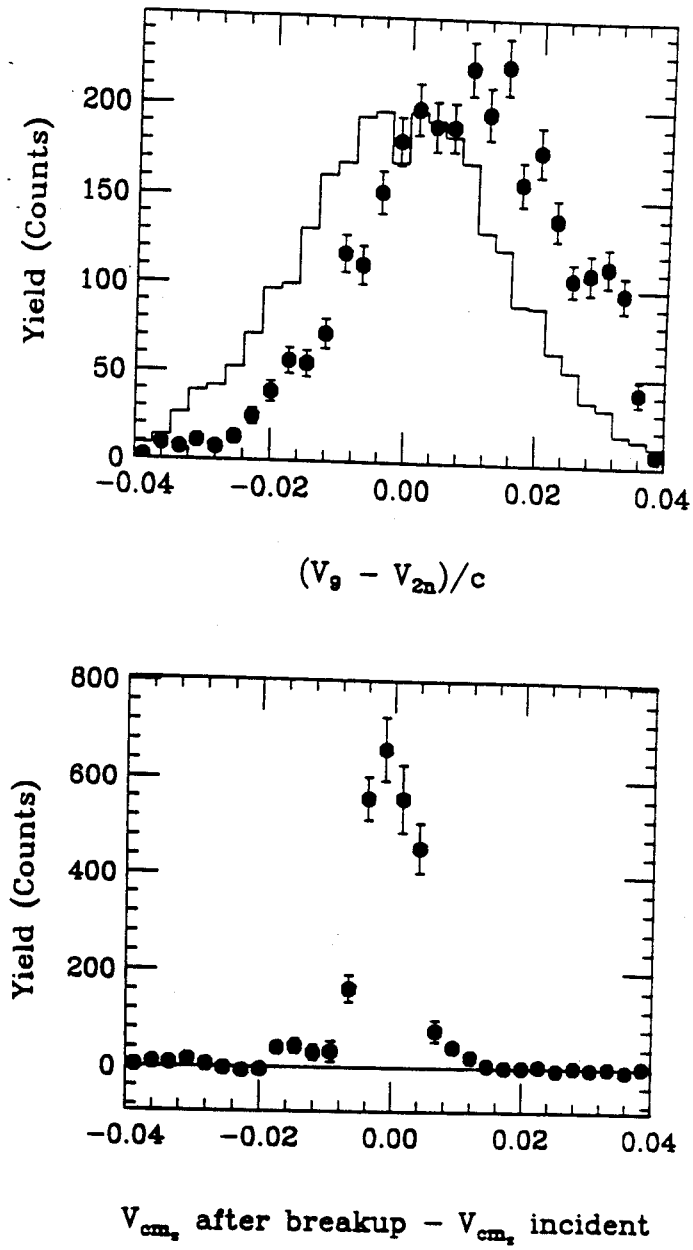

Figure 5.6: Spectrum for the magnitude of the velocity difference $V_9 - V_{2n}$, where V_{2n} is the average velocity of the two detected neutrons, is shown in (a). The histogram is the result of a simulation using an initial distribution with the velocity difference peaked at zero. Spectrum for the z-component of the center of mass velocity before breakup subtracted from the center of mass velocity after breakup is shown in (b). The near-zero centroid reflects overall momentum conservation. The width of the peak, about 0.008c FWHM, represents the overall velocity resolution of the system.

the lead nucleus, thus yielding events in which the ^{9}Li velocity is greater than the neutron velocity. Because the breakup is occuring close to the Pb nucleus, either the E1 excitation is populating a resonant state with a short lifetime or the breakup is direct.

In the case of a resonant state, the meanlife τ of the resonance can be roughly estimated from the difference in the z-components of the ^{9}Li velocity and the average velocity of the two neutrons. The z-direction is the direction along the beamline. For the z-components of velocity, the centroid of the relative velocity distribution was 0.0080c $\pm$ 0.0003c. Figure 5.7 is a schematic view of a ^{11}Li dissociation. A straight line trajectory is assumed, since the ^{11}Li is only deflected by a few degrees. It is also assumed that the excitation occurs at the distance of closest approach, because the electric field is the most intense at that point [18]. The beam velocity is denoted by V, and τ is the meanlife of the resonance. The distance from the Pb nucleus where the breakup occurs is denoted by r. After breakup, the ^{9}Li regains the Coulomb energy $U = Z_{Li}Z_{Pb}e^2/r$. The equation of motion for the velocity of ^{9}Li after breakup is:

$$\frac{d\vec{V}}{dt} = \frac{Z_{Li}Z_{Pb}e^2}{m_9 r^2}\frac{\vec{r}}{r} \quad \text{and} \quad \vec{r} = b\hat{x} + Vt\hat{z} \tag{5.5}$$

For the z-component, integrating from $t = \tau$ to $t = \infty$ yields the result:

$$V_{9z}(\infty) - V_{9z}(\tau) = \frac{Z_{Li}Z_{Pb}e^2}{m_9 V}\frac{1}{\sqrt{b^2 + V^2\tau^2}} \tag{5.6}$$

The velocity $V_{9z}(\infty)$ is calculated from the measured ^{9}Li energy. The velocity $V_{9z}(\tau)$ at the point of ^{11}Li breakup is unknown, but because the decay energy is only about 0.6 MeV, it can be assumed to be equal to the average neutron velocity $V_{2nz}(\tau)$ at that point. Because the neutron velocities are not affected by the Coulomb force, $V_{2nz}(\tau) = V_{2nz}(\infty)$, where $V_{2nz}(\infty)$ is the average neutron velocity determined from the TOF measurment of the two emitted neutrons. Therefore, $V_{9z}(\tau) = V_{2nz}(\infty)$,

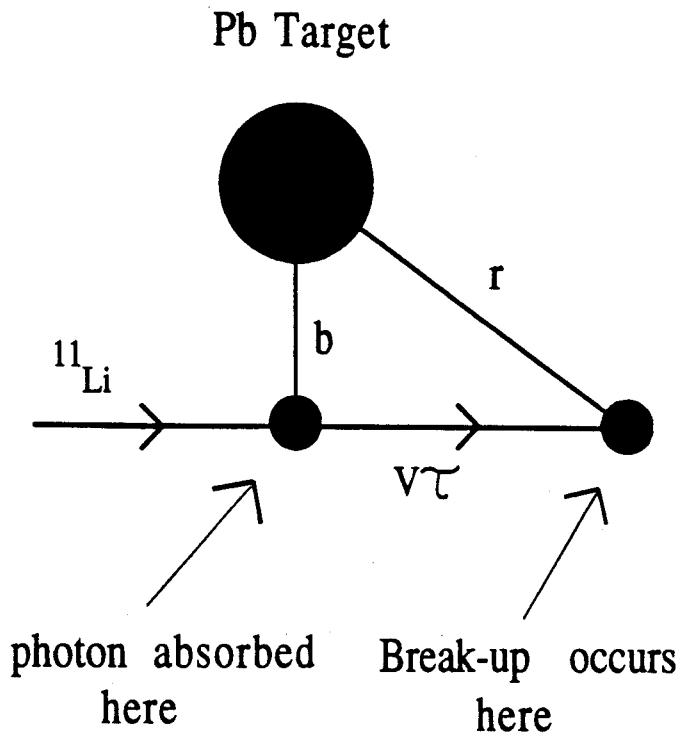

Figure 5.7: Schematic view of a ^{11}Li breakup. The average impact parameter is b=20 fm, the distance from the lead nucleus where the breakup occurs is denoted by r, V is the beam velocity and τ is the meanlife of the resonance.

and the centroid of the relative velocity spectrum shown in Figure 5.6a, and given by $\langle \Delta V \rangle = \langle V_{9z}(\infty) - V_{2nz}(\infty) \rangle$, is related to the meanlife of the resonant state as:

$$\langle \Delta V \rangle = \langle V_{9z}(\infty) - V_{2nz}(\infty) \rangle = \frac{Z_{Li} Z_{Pb} e^2}{m_9 V} \frac{1}{\sqrt{b^2 + V^2 \tau^2}} \tag{5.7}$$

Using an average impact parameter of $b = 20$ fm [36] and the centroid of the relative velocity distribution, $\langle \Delta V \rangle = 0.0080c \pm 0.0003c$, the meanlife of a resonant state is $\tau = 50 \pm 7$ fm/c. This meanlife yields a width $\Gamma = 4.0 \pm 0.5$ MeV. Therefore, a resonant state would require a width of approximately 4 MeV to be consistent with the measured velocity difference between the neutrons and the ^{9}Li . It must be re-emphasized that this is only intended to be a rough estimate of the width. However, the photonuclear cross section yielded a width of only 0.8 MeV, a factor of four too low. If the breakup mechanism proceeded via a resonant state, the width of the resonance from the photonuclear cross section would be consistent with the width determined from the ^{9}Li -neutron energy differences. It is this contradiction between the width determined from the photonuclear cross section and the width implied by neutron-^{9}Li velocity differences that rules out a resonant state and indicates the breakup mechanism must be direct.

It should not be surprising that the presence of a peak in the strength function or photonuclear spectrum does not guarantee the existence of a resonant state. A peak was predicted by the by the cluster model [15]. Recent calculations [33] have shown that, in general, loosely bound systems will have a peak in the strength function near threshold, and that the peak appears because of the large spatial extent of the loosely bound nucleons. A more general argument comes from the fact that the photonuclear spectrum will be zero at threshold, rise with increasing phase space, and eventually become zero at high excitations because the integrated cross section must be finite, thus producing a peak in the spectrum.

5.4 Momentum Distributions

Much of the study of ^{11}Li has been dedicated to measuring the momentum distributions of the ^{9}Li and neutrons resulting from the breakup of ^{11}Li on both high-Z and low-Z targets [2, 6, 43, 34]. A recent measurement of parallel momentum distributions of ^{9}Li following breakup on a tantalum target yielded $\sigma_9 \sim 17$ MeV/c, and the width deduced from a measurement of a neutron angular distribution in this work and in refs. [43, 6] was $\sigma_n \sim 10$ MeV/c. Because a kinematically complete measurement was performed for this work, the ^{9}Li and the neutron momentum distributions could be constructed in the rest frame of the ^{11}Li . The measured ^{9}Li and neutron momentum distributions are shown in Figure 5.8a,b. The momentum distributions in the ^{11}Li rest frame were parameterized by a Gaussian function $d^3\sigma/dp^3 \propto \exp(-p^2/2\sigma_i^2)$, with $\sigma_i = \sigma_9$ or σ_n. An integration over solid angle yielded the function (Maxwellian) used for the fitting: $d\sigma/dp = p^2 \exp(-p^2/2\sigma_9^2)$. For the ^{9}Li and neutron momentum distributions, the best fits yielded $\sigma_9 = 18 \pm 4$ MeV/c, in agreement with ref. [34] and $\sigma_n = 13 \pm 3$ MeV/c, in agreement with refs. [43, 6]. These width parameters have been corrected for detector acceptances and resolution.

The narrow widths of the ^{9}Li and the neutron momentum distributions have been interpreted as evidence for a neutron halo [6, 43], and as an indication of the internal momentum distribution of the ^{11}Li nucleus [34]. Recently, the measured values of σ_9 and σ_n were also used to show that the halo neutrons possess a high degree of directional correlation [44], indicating they tend to move in the same direction. A strong momentum correlation such as this would indicate that the halo neutrons are not in close proximity to each other. Also, a comparison of the widths of the distributions may also provide some insight into the degree of correlation of the halo neutrons. For example, for no correlation, the width of the neutron momentum

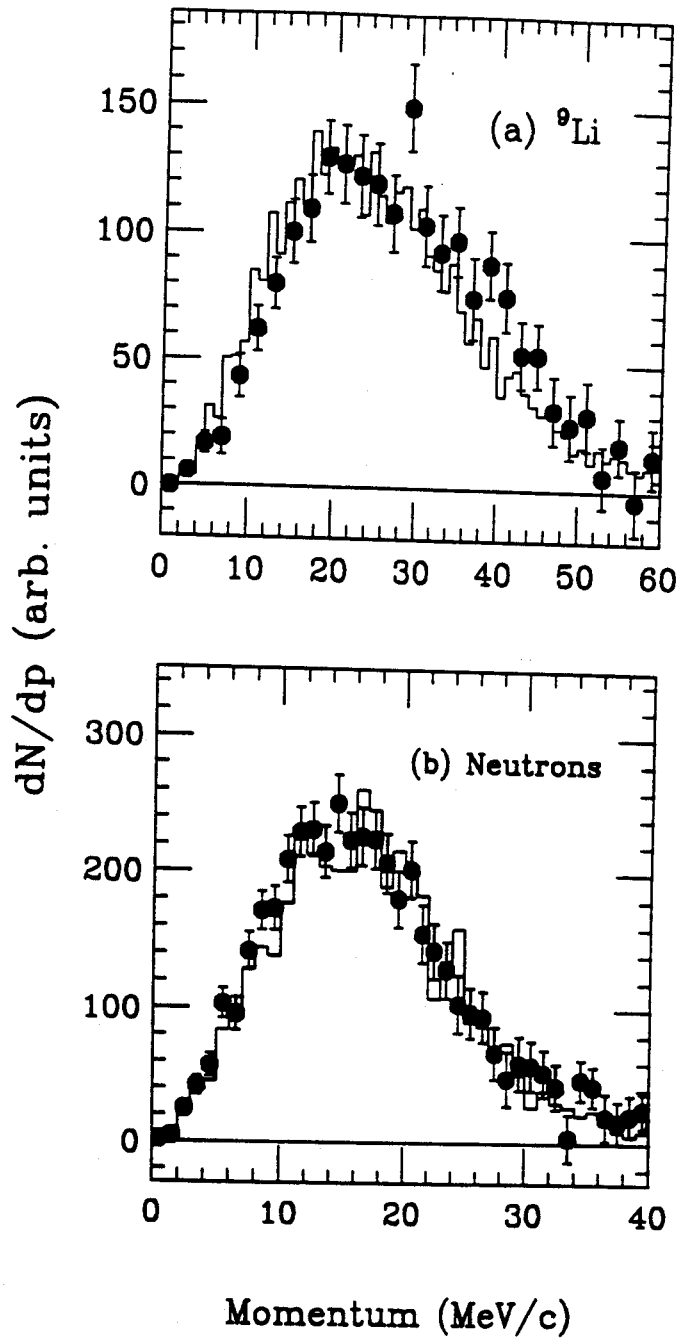

Figure 5.8: (a) ^{9}Li momentum distibution determined in the ^{11}Li rest frame. The histogram is the result of a simulation of ^{11}Li breakup with the decay energy partitioned by a 3-body phase space distribution. (b) Neutron momentum distribution in the ^{11}Li rest frame. The histogram is the result from the simulation.

distribution is expected to be $\sqrt{2}$ smaller than the width of the ^{9}Li distribution, as suggested by Hansen [45]. Alternatively, if a strong directional correlation exists between the neutrons, then the width $\sigma_n = 1/2\ \sigma_9$ since both neutrons recoil against the ^{9}Li .

A different interpretation is that the widths σ_n and σ_9 may reflect the breakup mechanism of ^{11}Li and the distribution of excitation energy absorbed by the ^{11}Li nucleus. Because of evidence presented earlier that the breakup of ^{11}Li into ^{9}Li and two neutrons following excitation is direct, it is natural to assume the excitation energy is partitioned between the ^{9}Li and neutrons via a 3-body phase space distribution. Therefore, a Monte Carlo simulation of the ^{11}Li breakup was developed that used the product of the measured photonuclear spectrum and the equivalent photon spectrum as the input excitation energy distribution. This product represents the ^{11}Li breakup probability as a function of excitation energy. The ^{11}Li decay energy was distributed between the two neutrons and the ^{9}Li based on a 3-body phase space distribution, and the angular distributions were chosen to be isotropic in the ^{11}Li rest frame. The simulation also included the detector acceptances. The predictions for the ^{9}Li and neutron momentum distributions are shown by the histograms in Figure 5.8 a,b respectively. The good agreement between the histograms and the data supports the interpretation that the ^{9}Li and neutron momentum distributions at least partially result from the distribution of excitation energies and the manner in which the excitation energy is partitioned between the three particles.

The 3-body phase space formulation also yields information about the degree of correlation between the halo neutrons. The kinetic energy distributions and average kinetic energies for each of the three particles are given by:

$$N(T_1)\ dT_1 = \sqrt{T_1(T_{1max} - T_1)}\ dT_1 \quad \text{and} \quad T_{1max} = \frac{m_2 + m_3}{m_1 + m_2 + m_3}\ E_d \qquad (5.8)$$

$$\langle T_1 \rangle = \frac{T_{1max}}{2} \quad and \quad \langle p_1^2 \rangle = m_1 T_{1max} \tag{5.9}$$

The average angle between the halo neutrons can be calculated from:

$$\langle \cos\theta_{12} \rangle = \frac{\langle \vec{P}_1 \cdot \vec{P}_2 \rangle}{\sqrt{\langle P_1^2 \rangle}\sqrt{\langle P_2^2 \rangle}} \quad \text{and} \quad 2\langle \vec{P}_1 \cdot \vec{P}_2 \rangle = \langle P_9^2 \rangle - \langle P_1^2 \rangle - \langle P_2^2 \rangle \tag{5.10}$$

Here, the subscripts 1 and 2 refer to the neutrons and 3 to the ^{9}Li . Substituting in the expressions for the average of the squares of the momenta yields $\langle \cos\theta_{12} \rangle = -m_n/(m_n + m_9) = -0.10$. The phase space distribution thus predicts a large opening angle, about 96 ° , between the halo neutrons in the ^{11}Li rest frame. The fact that the 3-body phase space formulation, which assumes the system is uncorrelated, reproduces both the ^{9}Li and the neutron momentum distributions is evidence that there is no correlation between the halo neutrons. This result contradicts a recent calculation of Tanihata *et al.* [44], where $\langle \cos\theta_{12} \rangle$ was calculated from the widths of the momentum distribution by the relationship $\langle P_i^2 \rangle = 3\sigma_i^2$. Using $\sigma_9 = 21 \pm 3$ MeV/c from [2] and $\sigma_n = 10 \pm 1$ MeV/c from [43, 6], their result was $\langle \cos\theta_{12} \rangle = 1.2 \pm 0.3$, consistent with $\theta_{12} = 0$ ° , indicating the presence of a strong directional correlation between the halo neutrons.

Although it is difficult to reconcile these two contradictory results, some additional data, the neutron-neutron relative momentum spectrum, can also be shown to agree with the 3-body space formulation of the ^{11}Li breakup. The neutron-neutron relative momentum spectrum was shown in Figure 2.4. A fit using the Gaussian distribution described above yielded a width $\sigma_{nn} = 10 \pm 2$ MeV/c, in agreement with the result expected from two uncorrelated neutrons each with $\sigma_n = 13$ MeV/c and an opening angle of 96 ° . The histogram is a prediction from the Monte Carlo simulation discussed above. The simulation is in reasonable agreement with the data, although the data are somewhat over-predicted at low relative momenta. It is expected that

a strong directional correlation between the halo neutrons, like that predicted in ref. [44], would produce a peak at low relative momenta, a peak that is not present. However, both the peak and the width of the neutron-neutron relative momentum spectrum, 10.5 MeV/c and 13 MeV/c respectively, are consistent with an average opening angle of 96 ° between the halo neutrons in the ^{11}Li rest frame. Therefore, all of our results, when compared to the predictions of a 3-body phase space formulation, suggest that there is no correlation between the halo neutrons.

Finally, one caveat regarding this analysis should be mentioned. Our conclusions are based on the success of a 3-body phase space formulation in reproducing the measured momentum distributions. It is reasonable to suppose that more sophisticated models that explicitly include correlations between the halo neutrons could also reproduce the measured distributions. For example, a correlated soft dipole model [14] predicts an opening angle between the neutrons of 110 °, although this result is for the neutron kinetic energies fixed at 100 keV rather than integrated over the complete distribution. It would be desirable to compare the predictions of more sophisticated models such as that of ref. [14] to our data in order to further understand the nature of the interaction between the halo neutrons.

Chapter 6

Summary

Both fragment singles events and coincidence events from the dissociation of ^{11}Li nuclei at 28 MeV/nucleon on a Pb target have been measured. The results from the fragment singles and 1n-^{9}Li are consistent with measurements from several other experiments [6, 32, 43, 31] and new results from the 2n-^{9}Li coincident data are presented. From the ^{9}Li fragment singles data, a total two-neutron removal cross section of $\sigma_{2n} = 5.1 \pm 0.3$ b was measured. Also, from the number of ^{11}Li nuclei transmitted through the target, a total reaction cross section of $\sigma_{tot} = 9.7 \pm 0.7$ b was determined.

The angular distribution for 1n-^{9}Li events was constructed between 0° and 5°. The angular distribution agreed very well with a previous measurement of the neutron angular distribution for a 29 MeV/nucleon ^{11}Li beam on a Au target [32]. The data from this measurement were combined with the data from ref. [32] and fitted with the sum of a narrow and a broad Gaussian. The fitting yielded a width of σ_n = 9.8 MeV/c for the neutron momentum distribution. From the combined neutron angular distribution, an integrated neutron cross section of $\sigma_{1n} = 8.3 \pm 0.5$ b was determined. This cross section could be considered to be a sum of the multiplicity-weighted contributions from Coulomb and nuclear dissociations. For multiplicities m_c =2 and m_{nuc} =1 and σ_{2n} =5.1 b, $\sigma_{2n} = \sigma_c + \sigma_{nuc}$, Coulomb and nuclear dissociation cross sections of $\sigma_c = 3.2 \pm 0.6$ b and $\sigma_{nuc} = 1.9 \pm 0.7$ b were calculated. The values

of the multiplicities were chosen based on a possible reaction mechanism for nuclear dissociation, namely absorption of a halo neutron by the Pb or scattering of a halo neutron by the lead into a broad angular range, and the fact that the combined angular distribution was limited to a maximum angle of 20°. The results for σ_c and σ_{nuc} were in reasonable agreement with two different theoretical estimates of the magnitudes of the Coulomb and nuclear dissociation cross sections [40, 41].

This work focused mainly on the data resulting from the complete kinematical measurement of the 2n-^{9}Li events. That measurement allowed the ^{11}Li decay energy, and hence the excitation energy, to be determined on an event-by-event basis. From the decay energy spectrum, an excitation-energy-dependent Coulomb dissociation cross section could be constructed. Dividing out the equivalent photon spectrum then yielded the photonuclear spectrum σ_{E1}(E) and dipole strength function dB(E1)/dE. The photonuclear spectrum was fitted with a Breit-Wigner resonance shape, yielding a resonance energy of E=1.0 MeV and a width Γ = 0.8 MeV. These parameters are in very good agreement with the location and width of the predicted soft dipole resonance predicted by a variety of models [4, 6, 12, 14, 42]. However, although there is little dispute that a low-energy E1 enhancement exists in ^{11}Li due to the large Coulomb dissociation cross section of 3.6 ± 0.4b, the exact nature of the enhancement is not known. Specifically, there is considerable debate about whether the excited ^{11}Li nucleus breaks up immediately, as in a direct breakup model, or if it populates a collective mode of the type discussed in refs. [9, 10]. The nature of the enhancement cannot be ascertained merely from the measurement of the photonuclear spectrum.

However, from a ^{9}Li -neutron relative velocity spectrum, the lifetime of the resonance was estimated to be τ = 50 fm/c, which yields a width of Γ = 4 MeV, a factor of five greater than the width of the photonuclear spectrum. This contradiction between the width from the photonuclear spectrum and the width estimated from a

relative velocity spectrum indicates that the photonuclear cross section does not describe a resonant state, and therefore, the breakup is direct. Thus our measurement is evidence against the existence of a soft dipole resonance, i.e., a vibrational resonance between the halo neutrons and the ^{9}Li core.

Also, from the complete kinematical measurement, ^{9}Li and neutron momentum distributions could be reconstruced in the rest frame of the ^{11}Li nucleus. The distributions were fitted with Gaussian functions and yielded widths of $\sigma_9 = 18 \pm 4$ MeV/c and $\sigma_n = 13 \pm 3$ MeV/c, in good agreement with previous measurements [2, 6, 34]. It should be noted that this determination of σ_n is independent of, but in agreement with, the value of σ_n from the 1n-^{9}Li events. Perhaps the most interesting feature of these momentum distributions was that they could be reproduced by a simulation that used the measured ^{11}Li excitation energy distribution, assuming the excitation energy was partitioned amongst the ^{9}Li and the neutrons according to a 3-body phase space distribution. This was interpreted as evidence that the excitation energy distribution and the nature of the breakup mechanism largely determine the shape of the momentum distributions. Also, this is evidence that there is no correlation between the halo neutrons, although comparisons of the data with other models are necessary to confirm this hypothesis.

APPENDICES

Apppendix A: Calibration of Fragment Detectors

I: The Silicon Detectors

Figure A.1 shows a sketch of a side view of the target and fragment detectors and a schematic representation of the pixel-like quality of the strip detector due to the 16 horizontal and 16 vertical strips. The first ΔE detector, a MICRON silicon strip detector, was located 15 cm from the Pb target. The distance was chosen to be close enough for complete solid angle coverage for the resulting forward focused ^{9}Li fragments, but still be far enough away to achieve sufficient angular resolution of the ^{9}Li . The 3.125 mm wide strips provide square pixels that are 3.125 mm on a side, yielding a ^{9}Li angular resolution of 1.2 $^{\circ}$. The second ΔE detector, a MICRON silicon detector of the same thickness, was used to increase the ratio of energy loss to straggling. The second silicon detector yielded an energy loss similar to that of the strip detector. The total energy loss is about doubled, but the energy loss straggling, which is proportional to the square root of the thickness of the medium, only increases by 40%.

Energy signals were readout from each of the 32 strips, although the magnitudes of the energy signals from the back set of strips are equivalent to those of the front set of strips. One energy signal was also readout from the second ΔE detector. Fast signals were picked-off of the energy signals coming from the front (horizontal) strips

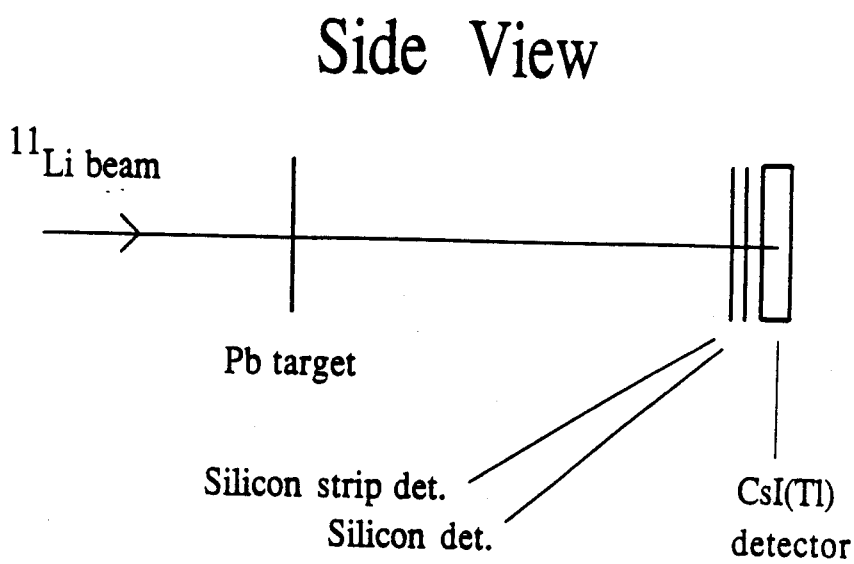

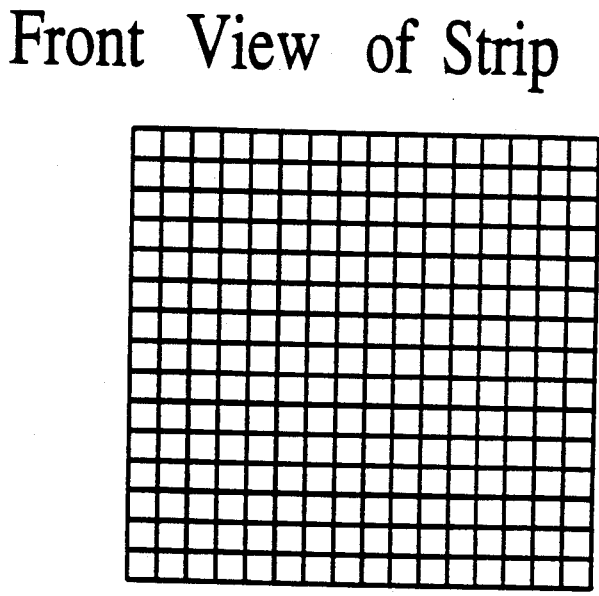

Figure A.1: Side view of target and fragment telescope setup. The telescope consisted of a 300 μm strip detector, a 300 μm silicon detector, and 1.2 cm thick CsI(Tl) detector. The front view of the strip detector shows the pixel structure defined by the horizontal and vertical strips, used to determine the ^{9}Li angle.

by a Berkeley 21X742 timing preamplifier/pick-off unit. The fast signals were fed through a constant fraction discriminator, which generated a logic signal (NIM) as a stop for the neutron tof measurement. The energy signals from both silicon detectors went through preamplifiers and amplifiers before being digitized by Ortec AD811 Amplitude-to-Digital Converters (ADC's).

Two problems were discovered with the strip detectors. First, there was a great deal of cross talk between strips. Here, cross talk means that the pulse of electrons liberated by a charged particle striking a strip would induce smaller pulses in neighboring strips. Therefore, for almost every event, several strips yielded signals. The induced signals were in all cases about two orders of magnitude lower than the signal caused directly by the charged particle, so in the analysis only the strip which yielded the maximum signal was used to determine charged particle energy and angle information. The second problem involved the pulse shape of the signal. The recommended bias for the strip detector was V=17 Volts to reach full depletion. The pulse rise time, t_r, is given by $t_r = d^2/\mu V$, where d=300 μm is the thickness of the silicon, μ=1200 cm^2/volt·s is the electron mobility in silicon and V=30 Volts is the voltage applied to the detector. Substituting these values into the equation yields a rise time of 44 ns. The ^{9}Li fragments, on average, deposited about 11 MeV into a strip. The size of this signal, coupled with the rise time, produced a signal whose amplitude was too low to trigger the time pick-off units. Therefore, fast signals required for the neutron tof measurement could not be obtained from the strip detector under these conditions. In order to obtained the required fast output signal, the strip detector was biased up to V=60 Volts. At this voltage, t_r = 12 ns, and a fast signal was obtained from the time pick-off units. The leakage current was monitored for the duration of the experiment to check for damage caused by the excessive voltage.

The silicon strip detector and the second ΔE detector were each calibrated sep-

arately using a thin ^{228}Th source. ^{228}Th and subsequent daughter nuclei emit α-particles at eight energies: 5.34 MeV, 5.42 MeV, 5.69 MeV, 6.05 MeV, 6.09 MeV, 6.29 MeV, 6.78 MeV and 8.78 MeV [46]. All of these α-particles stop in less than 300 μm of silicon. The peak at 5.34 MeV was not strong enough to be used as a calibration point and the α-particles at 6.05 MeV and 6.09 MeV were not resolvable due to the resolution of the detectors, about 200 keV FWHM. For the α-particles at 6.05 MeV and 6.09 MeV, an average energy of 6.07 MeV was used instead. Therefore six different calibration points were available. Each strip of the strip detector was calibrated separately. The spectrum for horizontal strip 7 is shown in Figure A.2a. In Figure A.2b a plot of α-particle energy versus channel number is shown. The solid line is the calibration, determined from a least squares fit to the six points.

II: The CsI(Tl) Detector

The light produced by charged particles stopping in the CsI(Tl) detector was read out by four PIN diodes attached to the back surface of the CsI(Tl). The voltage applied across the four diodes was +400 V. The diodes were connected in series, so the voltage across each diode was +100 Volts. The leakage current was typically 100 nA. The signals from the diodes were first processed by a preamplifier [24] and then by a standard spectroscopy amplifier before being digitized by an Ortec AD811 ADC module. Because of the low power dissipation of the preamplifier, 0.5 W [24], the preamplifier could be placed in the target chamber, hence under vacuum, without overheating the diode.

Unlike silicon detectors, where the magnitude of the energy signal depends only on the energy loss of the particle, the light output of CsI(Tl) depends not only on the energy loss of the incident particle, but on the atomic number Z and often on

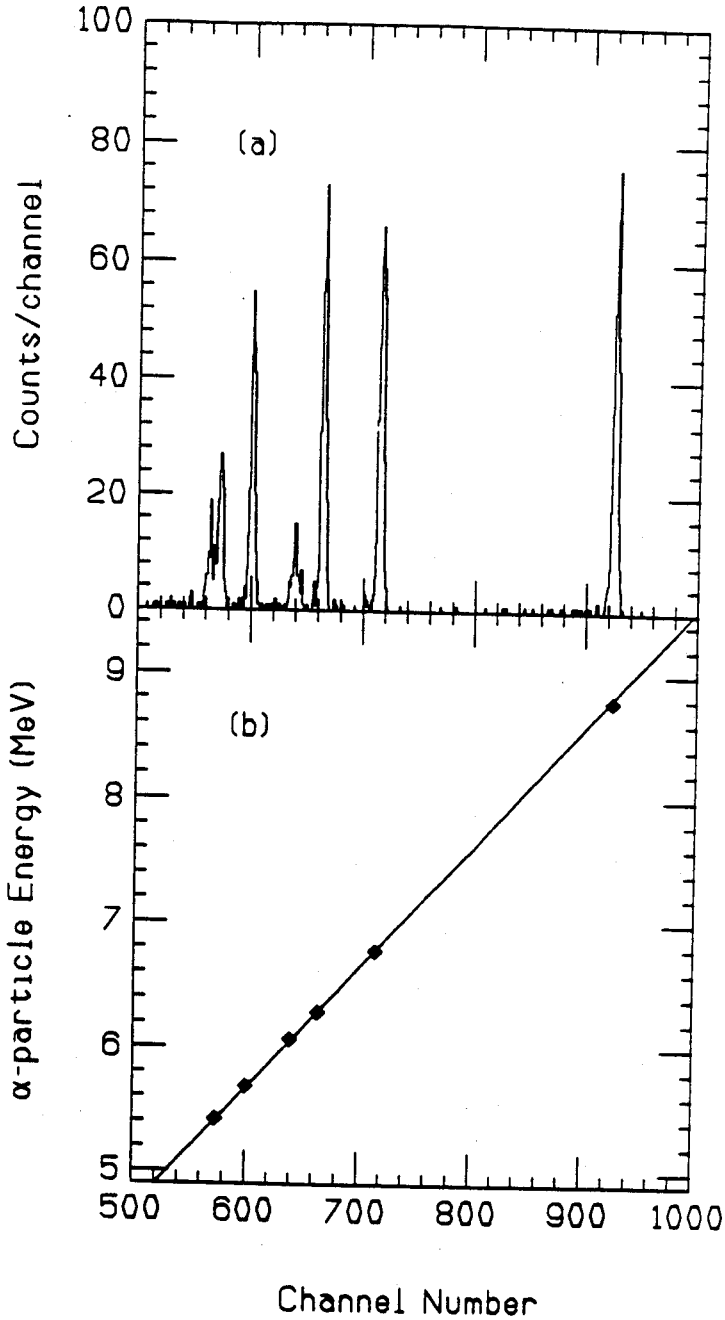

Figure A.2: (a) Energy spectrum for horizontal strip 7 using a ^{228}Th source for calibration. The energies of the α-particles are given in the text. (b) Calibration for horizontal strip 7. The six calibration points were fitted with a straight line.

the atomic mass A of the particle as well [24, 25, 47, 22]. Furthermore, for a given A and Z, often the energy dependence is non-linear over a large energy range. Therefore, instead of a simple calibration using an α-particle source such as ^{228}Th, the CsI(Tl) must be calibrated with the same ion or ions that are to be measured in the experiment, and in the same energy range.

The calibration of the CsI(Tl) was performed using ^{9}Li beams at 34 MeV/nucleon and 45 MeV/nucleon. The calibration beams were produced by the fragmentation of an ^{18}O primary beam on a ^{9}Be target. The energy spread of the ^{9}Li beams was limited to 0.6% FWHM by the A1200. The Pb target and the thick degrader scintillator were removed from the beamline, so the ^{9}Li beam only traversed the silicon ΔE detectors before stopping in the CsI(Tl) detector. The calibration beam consisted primarily of ^{9}Li but contained small percentages of other Li isotopes as well as tritons and He, Be, B and C isotopes. A list of the isotopes and their energies is given in Table A.1. The energies represent the ion energy after traversing both silicon ΔE detectors. The tritons and He isotopes are not included because they punched through the CsI(Tl) detector. From the known momentum of the ^{9}Li beam, the Bρ value could be calculated for the last dipole magnet in the beamline, where $B\rho = p/q$ and B is the magnetic field strength, ρ is the bending radius, p is the momentum of the beam particle and q is the charge. The other particles could then be identified from the ΔE signal and the value of $B\rho$, since $\Delta E \propto q^2/v^2 \propto m^2/(B\rho)^2$, with v the velocity of the beam particle. The total energy of each particle was calculated from the energy loss in the silicon. The result of the calibration for the CsI(Tl) is shown in Figure A.3. The CsI(Tl) response was linear in this energy range, possessed the expected Z-dependence, but displayed very little A-dependence.

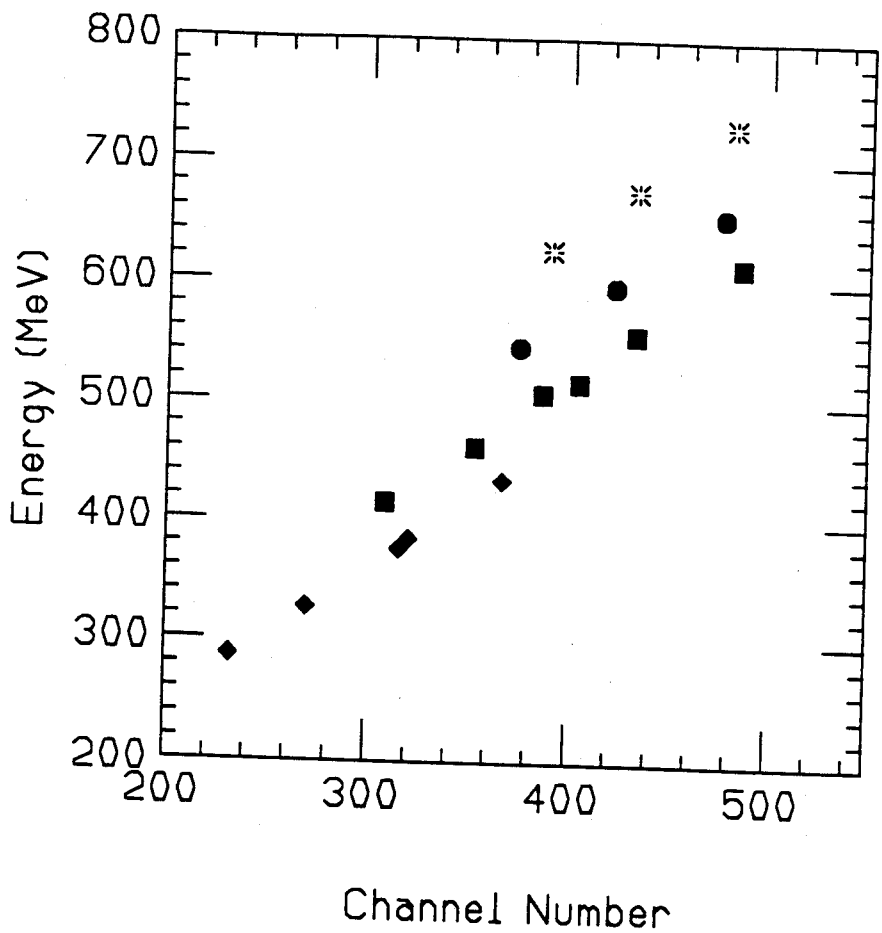

Figure A.3: Calibration data for the CsI(Tl) detector. The isotopes and energies are listed in Table 2. The solid diamonds are Li isotopes, the solid squares are Be isotopes, the solid circles are B isotopes and the stars are C isotopes.

Table A.1: Ions and their energies present in the calibration beams

Ion	Energy (MeV)
^{7}Li	376.3
^{8}Li	327.1
^{8}Li	434.5
^{9}Li	287.5
^{9}Li	384.9
^{9}Be	516.0
^{10}Be	461.7
^{10}Be	614.0
^{11}Be	415.3
^{11}Be	556.3
^{12}Be	507.1
^{11}B	654.3
^{12}B	595.9
^{13}B	544.9
^{14}C	729.9
^{15}C	674.9
^{16}C	625.4

Appendix 2: Decay Energy Calculation

It would not be possible to determine the ^{11}Li excitation energy with sufficient resolution by only measuring the energies of the incident and final particles. For example, energy conservation for the excitation and decay of ^{11}Li requires the equation $E_{11} + E - S_{2n} = E_9 + E_1 + E_2 + E_{Pb}$ to be satisfied for each ^{11}Li that breaks up via Coulomb dissociation. In this equation, E_9 is the ^{9}Li kinetic energy, E_1 and E_2 are neutron kinetic energies, E_{Pb} is the energy of the recoiling Pb nucleus, E is the excitation energy (the energy of the absorbed photon), E_{11} is the incident ^{11}Li kinetic energy and S_{2n} is the neutron separation energy of ^{11}Li , by convention a positive number here. In principle, a measurement of the incident ^{11}Li energy and a measurement of the energies of the emitted ^{9}Li , the two neutrons and the Pb nucleus would yield the excitation energy. However, in addition to the difficulty of measuring the small Pb recoil (about 0.7 MeV), for reasonable neutron and ^{9}Li energy resolutions of $\delta E_1 = \delta E_2 = 1$ MeV and $\delta E_9 = 3$ MeV (representing 1% energy resolution for a 30 MeV/nucleon ^{9}Li nucleus), and a 0.2% energy resolution for a 30 MeV/nucleon incident ^{11}Li beam, the best resolution available from the A1200, the excitation energy resolution would be $\delta E = 3.4$ MeV. Because the soft dipole resonance of ^{11}Li is predicted to exist near $E = 1$ MeV, a technique with superior resolution is necessary.

Fortunately, a technique that does provide sufficient energy resolution is available that does not require the Pb recoil energy to be measured. Energy conservation in

the rest frame of the ^{11}Li can be expressed as follows:

$$E_d = \frac{1}{2} m_9 V_9'^2 + \frac{1}{2} m_n V_1'^2 + \frac{1}{2} m_n V_2'^2 \tag{B.1}$$

The neutron and ^{9}Li masses are denoted by m_n and m_9 and the primed velocities are the ^{9}Li and neutron velocities in the rest frame of the decaying ^{11}Li . The decay energy E_d of ^{11}Li is related to the excitation energy by $E = E_d + S_{2n}$. A schematic picture of a ^{11}Li breakup into a ^{9}Li and two neutrons is shown in Figure B.1. The velocity $\vec{V}_9'$ is the ^{9}Li velocity in the ^{11}Li rest frame, $\vec{V}_{2n}'$ is the velocity of the two-neutron center of mass in the ^{11}Li rest frame, $\vec{V}_{2n}' = (\vec{V}_1' + \vec{V}_2')/2$, $\vec{V}_1'$ and $\vec{V}_1'$ are the neutron velocities in the ^{11}Li rest frame and $\vec{V}_1''$ and $\vec{V}_2''$ are the neutron velocities in the rest frame of the two-neutron center of mass. Two relative velocity vectors can be defined as follows:

$$\vec{V}_{2n-9}' = \vec{V}_9' - \vec{V}_{2n}' \tag{B.2}$$

$$\vec{V}_{n-n}'' = \vec{V}_1'' - \vec{V}_2'' \tag{B.3}$$

From momentum conservation, $\vec{V}_1'' = -\vec{V}_2''$ and $\vec{V}_9' = -2m_n\vec{V}_{2n}'/m_9$. Substituting these relationships and eqns. 2.2 and 2.3 into eqn. B.1 yields the decay energy in terms of the relative velocities:

$$E_d = \frac{1}{2}\mu_1 \vec{V}_{2n-9}'^2 + \frac{1}{2}\mu_2 \vec{V}_{n-n}''^2 \tag{B.4}$$

$$\text{with } \mu_1 = \frac{m_9(2m_n)}{m_9 + (2m_n)} \text{ and } \mu_2 = \frac{m_n}{2} \tag{B.5}$$

A measurement of the energy and angle of both neutrons and the ^{9}Li allows the laboratory velocity vectors of each particle to be calculated. Then the relative velocity vector between the ^{9}Li and two-neutron center of mass, as well as the neutron-neutron

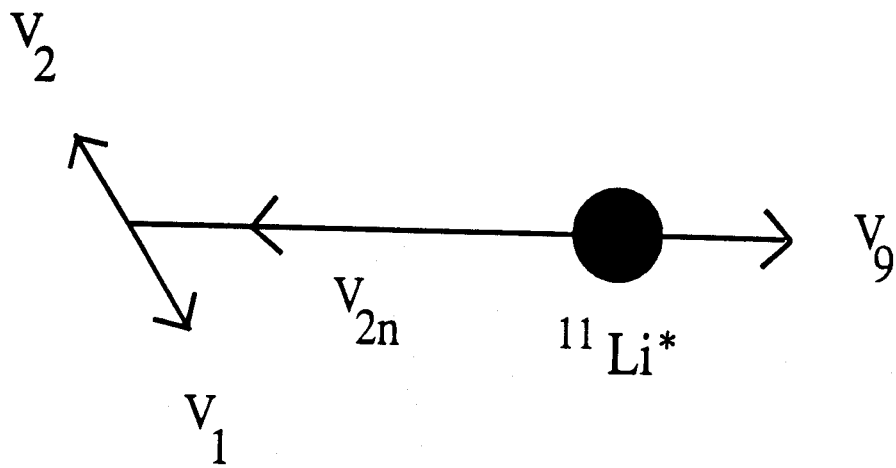

Figure B.1: ^{11}Li breakup into ^{9}Li and two neutrons. Momentum conservation requires the ^{9}Li and the two-neutron center of mass to have equal and opposite momenta. In the rest frame of the two-neutron center of mass, each neutron has equal and opposite momenta.

relative velocity vector, can be calculated in the laboratory frame. The relative velocity components can then be Lorentz transformed to the ^{11}Li rest frame and the two-neutron center of mass frame in order to calculate the decay energy with eqn. B.4. For example, the longitudinal and transverse components of the relative velocity between the ^{9}Li and the two-neutron center of mass in the ^{11}Li rest frame is calculated from the Lorentz transformation as follows:

$$V'_{2n-9_z} = V'_{9_z} - V'_{2n_z} = \frac{V_{9_z} - V_0}{1 - V_0 V_{9_z}} - \frac{V_{2n_z} - V_0}{1 - V_0 V_{2n_z}} \tag{B.6}$$

$$V'_{2n-9_\perp} = V'_{9_\perp} - V'_{2n_\perp} = \frac{V_{9_\perp}}{\gamma(1 - V_0 V_{9_\perp})} - \frac{V_{2n_\perp}}{\gamma(1 - V_0 V_{2n_\perp})} \tag{B.7}$$

All velocities are in units of c. The longitudinal direction is labelled the z-direction which is also the direction along the beamline. The transverse components are thus the x and y components. The $\vec{V}_9$ and $\vec{V}_{2n}$ are laboratory velocities, and the velocity $\vec{V}_0$ is the velocity of the laboratory frame, which can be calculated from the average ^{11}Li beam energy of 28 MeV/nucleon. The angular spread in the ^{11}Li beam is only about 0.5 ° and the average Rutherford deflection for all the events is 1.6 ° hence the velocity $\vec{V}_0 \approx V_0\hat{z}$. For a ^{11}Li beam energy of 28 MeV/nucleon, assuming the relative velocities are frame invariant only induces about an 11% error in the decay energy. As will shown later, this error is much less than the decay energy resolution. Therefore, the relative velocities were considered to be frame invariant, and the decay energy for each event was calculated from the relative velocities determined in the laboratory reference frame. The decay energy expressed in terms of the laboratory relative velocities is then:

$$E_d = \frac{1}{2}\mu_1 \vec{V}^2_{2n-9} + \frac{1}{2}\mu_2 \vec{V}^2_{n-n} \quad \text{and} \quad \vec{V}_{2n} = (\vec{V}_1 + \vec{V}_2)/2 \tag{B.8}$$

An advantage of this expression is that the ^{11}Li velocity $\vec{V}_0$ is not required. With the approximation that the relative velocities are frame invariant, the decay energy of

each event was calulated from the laboratory ^{9}Li and neutron velocity components, and the decay energy spectrum was constructed. Finally, it should be noted that this technique of using relative velocities to determine the decay energy of unbound states in excited nuclei has been successfully applied to several neutron-unbound states in excited ^{13}C and ^{12}B nuclei [48]. In this case, the excited nuclei decayed into a ^{12}C plus a neutron or ^{11}B plus a neutron, respectively. A detailed discussion is given in ref. [48].

The principle motivation for using the relative velocities to calculate the decay energy was the relatively good decay energy resolution obtainable with this technique. The resolution response of the detection system as a function of decay energy was discussed in Chapter 5. The separate contribution to the response from neutron timing and neutron angular resolutions, energy losses in the Pb target, ^{9}Li angular resolution, and multiple scattering in the target were also investigated and are presented here. A plot of each of these contributions for a 100 keV decay are shown in Figure B.2a-e and the total resolution for a 100 keV decay is shown in Figure B.2f. The response functions due to the uncertainty in the neutron timing and angle represent the net effect from both neutrons. The response due to the ^{9}Li energy measurement represents the combined uncertainty of the energy resolution of the silicon detectors, the CsI(Tl) detector, and energy losses in the target. Figure B.3 shows the separate response functions and the total response function for 500 keV decays.

The correction for energy losses in the target is the largest source of uncertainty in determining the ^{11}Li decay energy. Because it is not known where in the target the reaction occurs, it must be assumed that the reaction happens in the center of the target. In the data analysis, to compensate for energy loss in the target, the measured energy of each ^{9}Li is increased by the amount of energy the ^{9}Li would lose in half the thickness of the Pb target. For the average ^{9}Li energy in this experiment

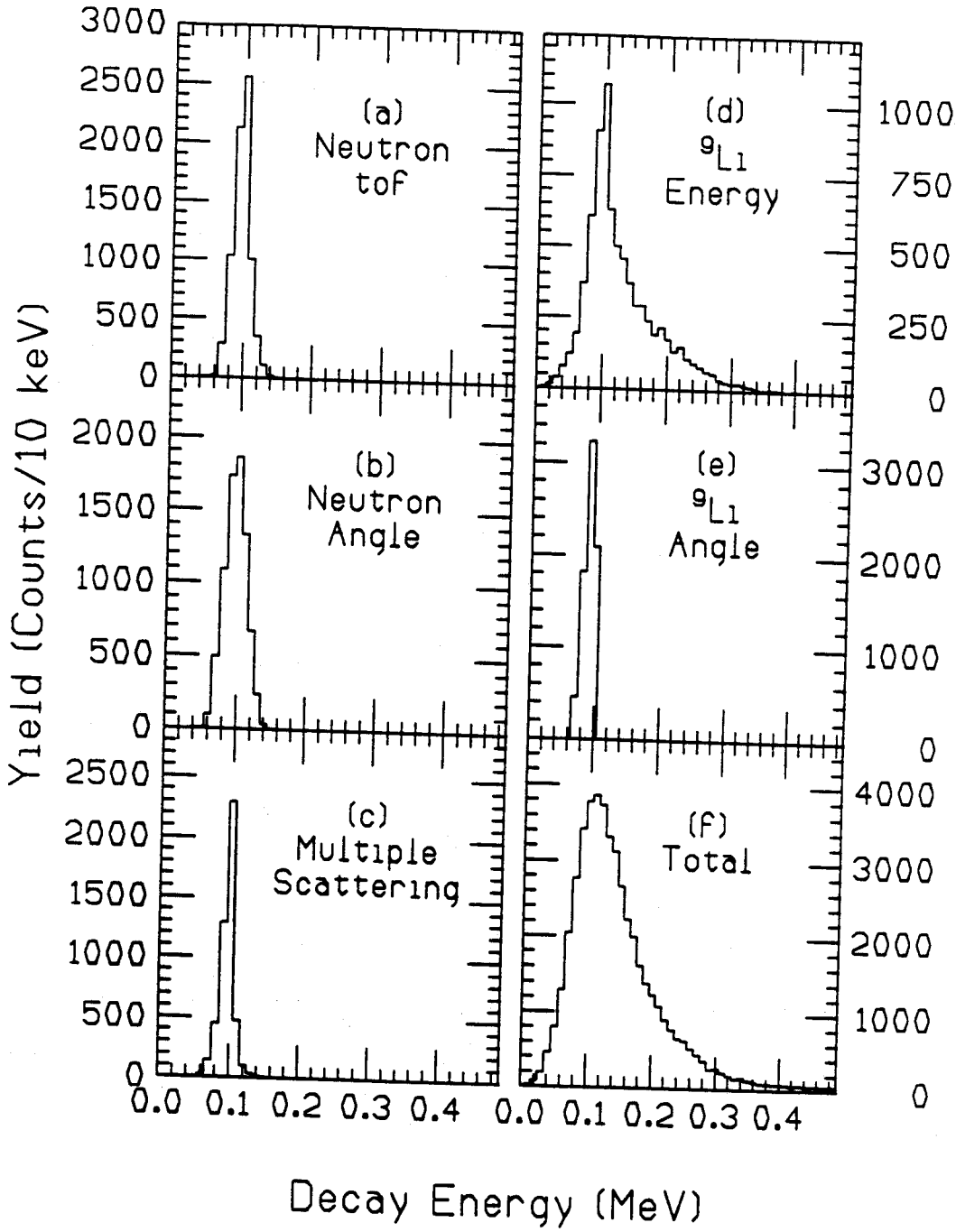

Figure B.2: Contributions to the response function for 100 keV decay energies due to neutron timing resolution, neutron angular resolution, multiple scattering in the target, energy loss in the target, and the ^{9}Li angular resolution. The total resolution function is shown in (f).

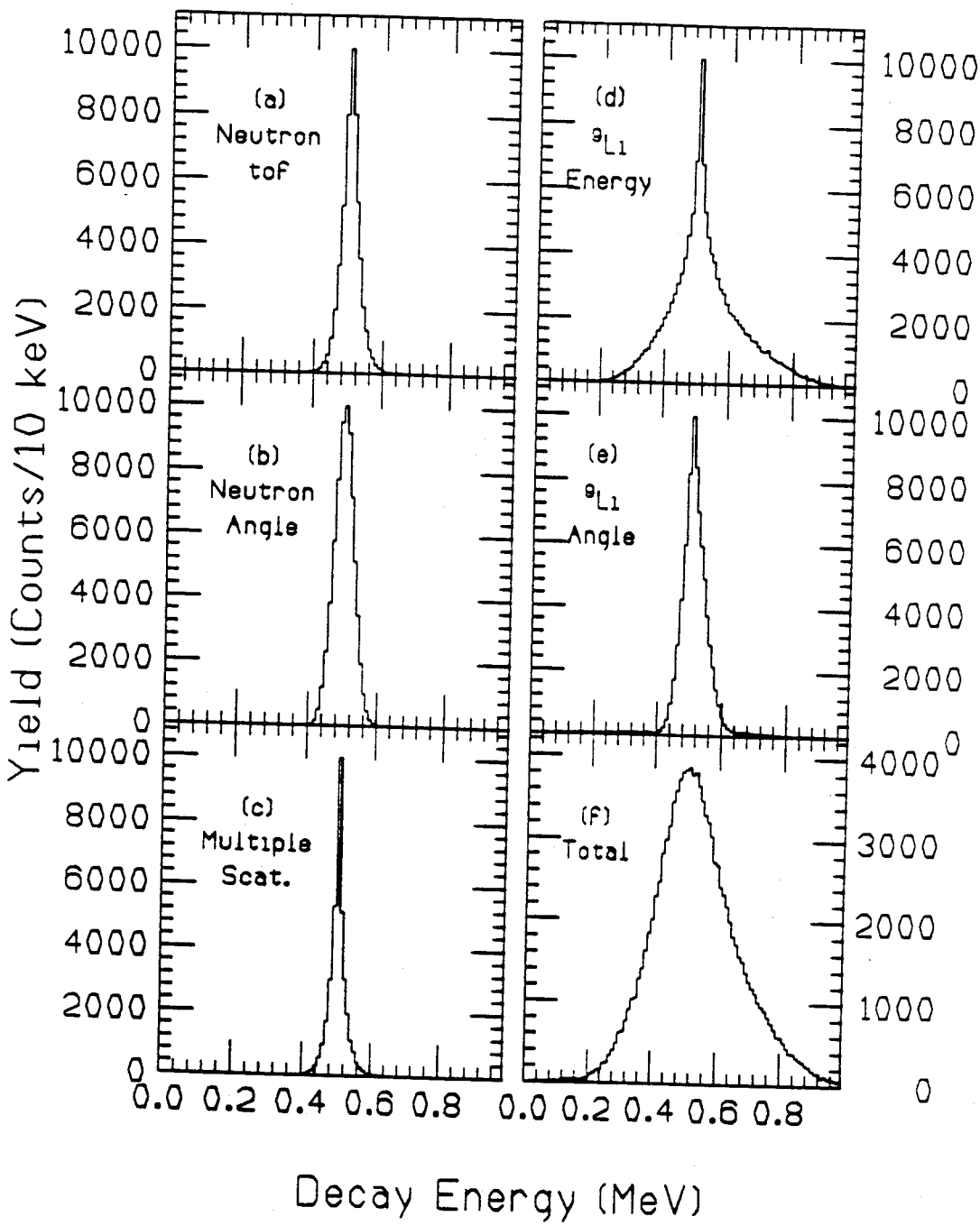

Figure B.3: Contributions to the response function for 500 keV decay energies due to neutron timing resolution, neutron angular resolution, multiple scattering in the target, energy loss in the target, and the ^{9}Li angular resolution. The total resolution function is shown in (f).

with a 0.598 g/cm^2 Pb target, the average ^{9}Li energy loss in half the target thickness was 22 MeV. In the extreme cases, ^{9}Li could have been formed in the front or the back of the target, so adding on 22 MeV to the measured ^{9}Li energy could cause a maximum error in the ^{9}Li energy of $\pm$ 22 MeV.

Appendix C: Correction for Post-Breakup Coulomb Acceleration

Because of post-breakup Coulomb acceleration, the measured velocity of the ^{9}Li is somewhat higher than the velocity of the ^{9}Li immediately after the breakup of ^{11}Li . Therefore, the measured relative velocity $\vec{V}_{9-2n}$, and hence the calculated decay energy, are not quite correct. In the following, a method for correcting the error in the decay energy due to post-breakup Coulomb acceleration is presented.

The starting point for the method is the breakup scenario shown in Figure 5.7 in Chapter 5 and the application of the classical equations of motion for a charged particle moving in an electromagnetic field. The incident ^{11}Li particle is assumed to follow a straight line trajectory at an impact parameter b with a velocity V. It is also assumed that the photon is absorbed at the distance of closest approach. Now suppose the breakup occurs at a distance r from the Pb nucleus. If the relative velocities could be measured at the breakup point, no correction would be necessary for the decay energy. However, for ^{9}Li only its re-accelerated velocity is measurable. Therefore, the change in the ^{9}Li velocity due to the Coulomb field of the Pb nucleus must be calculated and subtracted from the measured ^{9}Li velocity components. Of course, the velocities of the neutrons are not altered by the Coulomb field of the Pb, so the measured neutron velocities are equal to the neutron velocities at the point of

breakup. For the ^{9}Li particle, the equation of motion is:

$$\frac{d\vec{V}_9}{dt} = \frac{Z_{Li}Z_{Pb}e^2}{m_9 r^2}\frac{\vec{r}}{r} \quad \text{and} \quad \vec{r} = b\hat{x} + V_9 t\hat{z} \tag{C.1}$$

The non-relativistic formulation ($\gamma = 1.0$) has been used because $\gamma = 1.03$ for a 28 MeV/nucleon ^{11}Li beam. The lifetime of the excited ^{11}Li is denoted by τ. The photon is absorbed at t=0, r=b, and the ^{11}Li breaks up at t=tau, at a distance r from the Pb nucleus. Making the additional assumption that the change in the velocity of ^{9}Li is small, and hence replacing V_9 with the average beam velocity V in the expression for $\vec{r}$ allows the equation of motion to be integrated directly. Integrating from $t = \tau$ to $t = \infty$ yields the change in the longitudinal and transverse velocity of ^{9}Li . The z-direction (beam diretion) is taken as the longitudinal direction.

$$\Delta V_z \equiv V_{9z}(\infty) - V_{9z}(\tau) = \frac{Z_{Li}Z_{Pb}e^2}{m_9 V}\frac{1}{\sqrt{b^2 + V^2\tau^2}} \tag{C.2}$$

$$\Delta V_\perp \equiv V_{9\perp}(\infty) - V_{9\perp}(\tau) = \frac{Z_{Li}Z_{Pb}e^2}{m_9 b}\left[\frac{1}{V} - \frac{\tau}{\sqrt{b^2 + V^2\tau^2}}\right] \tag{C.3}$$

The changes in the x and y velocity components are taken as $\Delta V_x = \Delta V_y = \Delta V_\perp/\sqrt{2}$. Although straight line trajectories were assumed, transverse accelerations were still calculated. The convenient approximation of a straight line trajectory merely allows the integrations to be done analytically.

Calculating the impact parameter for each event as described in Chapter 5, Section 1, and using the average lifetime τ = 50 fm/c that was determined in Chapter 5, Section 3, the values of ΔV_x, ΔV_y and ΔV_z were determined on an event-by-event basis. These values were then subtracted from the measured ^{9}Li velocity components to yield corrected ^{9}Li velocity components, defined here as V_{xc}, V_{yc} and V_{zc}. The corrected ^{9}Li velocity components and the measured neutron velocities were used to

calculate the relative velocities and hence the corrected decay energy spectrum. Figure C.1a shows the distribution for the z-component of the relative velocity between the ^{9}Li velocity and the average neutron velocity V_{2n} calculated for each event before any corrections were applied. These data were also presented previously, in Figure 5.6. The distribution for the relative velocity using the corrected ^{9}Li velocities is shown in Figure C.1b. This velocity spectrum is centered about zero, indicating the validity of the correction procedure.

It is also interesting to examine the decay energy spectrum that results with and without the correction for post-breakup Coulomb acceleration. Figure C.2a shows the decay energy spectrum that results if no correction is made to the ^{9}Li velocity. In Figure C.2b, the decay energy spectrum that uses the corrected ^{9}Li velocities is shown. This spectrum was also shown previously, in Figure 5.1c. Comparing the two spectra, it can be seen that the post-breakup acceleration causes a significant broadening, about 200 keV, of the decay energy spectrum and a shift in the centroid to higher decay energies.

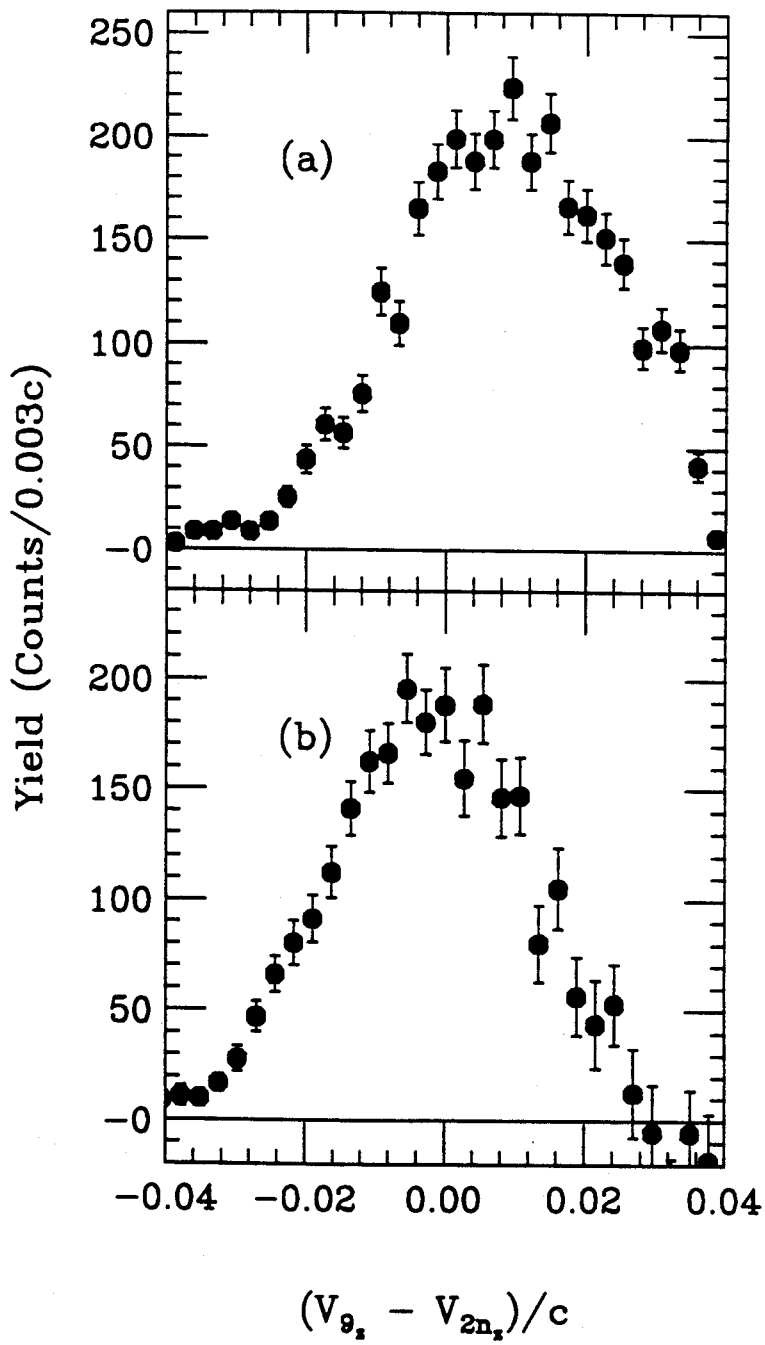

Figure C.1: (a) Longitudinal (z) component of ^{9}Li and average neutron relative velocity for each event. (b) Relative velocity difference after correcting ^{9}Li for post-breakup Coulomb acceleration.

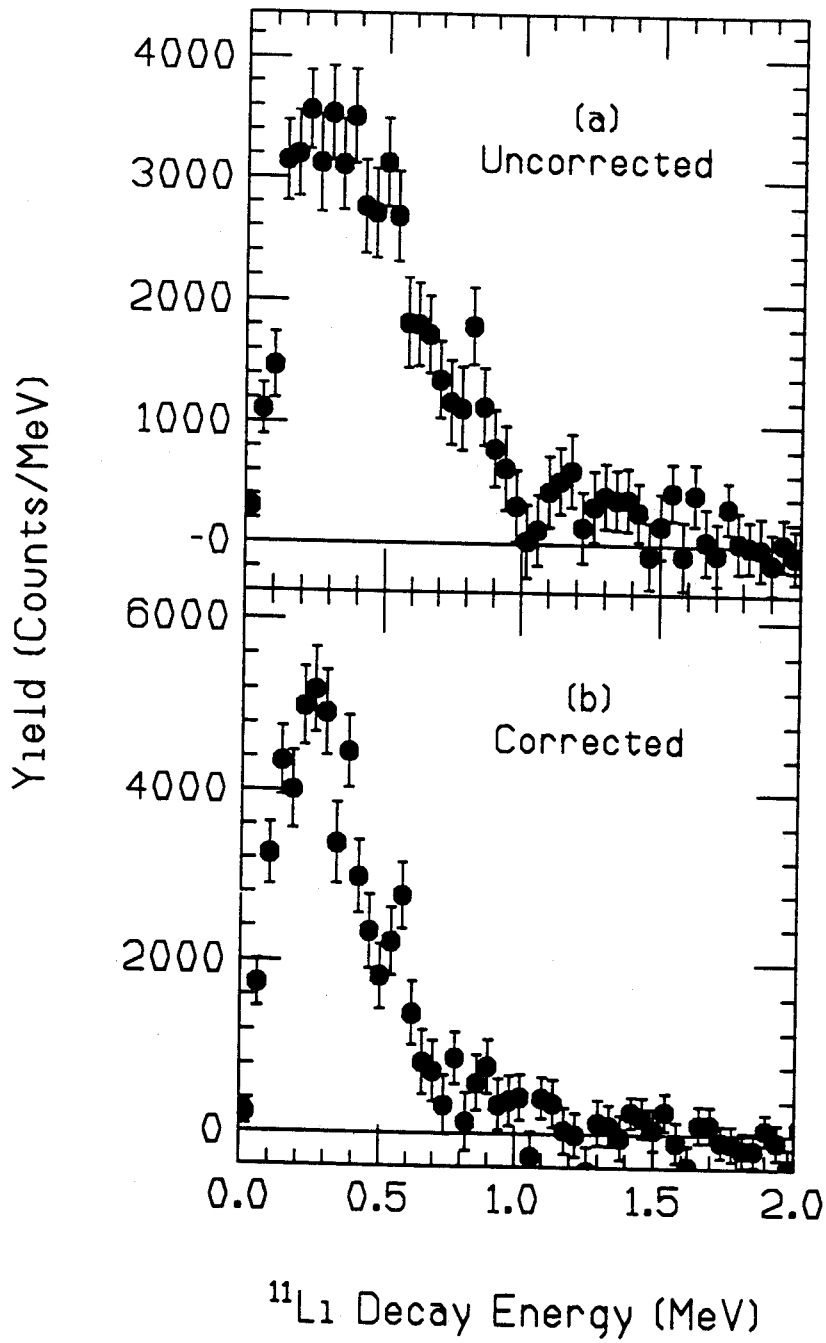

Figure C.2: (a) Decay energy spectrum before correcting for post-breakup Coulomb acceleration. (b) Decay energy spectrum after the correction.

Appendix D: Results from the ^{7}Li(p,n) Experiment

The problem of cross talk was discussed in Chapter 2. The purpose of this appendix is to display some additional data from the ^{7}Li(p,n) experiment that was relevant to the cross-talk rejection procedure described earlier. First the basic strategy of the cross-talk rejection will be reviewed.

The cross-talk rejection procedure consisted of calculating the quantity $\Delta E_n = E_n - E_s - E_p$ for a two-neutron ^{9}Li coincidence event. The quantites E_n, E_s and E_p were defined earlier and are shown in Figure D.1 for a typical cross-talk event. For a cross-talk event, $\Delta E_n = 0$ by energy conservation. Figure D.1 also depicts a true neutron-neutron coincidence event. For the true events, the quantity E_s is determined from the time difference between the arrival of the two neutrons at their respective detectors. However, since this is not a cross-talk event, E_s does not represent the energy of a scattered neutron. Hence the quantity ΔE_n takes on arbitrary values for the true coincidences.

The spectrum for ΔE_n for the n-n events from the ^{7}Li(p,n) data is shown in Figure D.2. This spectrum consists entirely of cross-talk events. Although there is a peak at $\Delta E_n = 0$, there is also a non-negligible shoulder on the peak at $\Delta E_n > 0$. This shoulder originates from events when reactions other than n-p elastic scattering produced the pulse height. For example, for the reaction n+C$\rightarrow$ n + 3α -7.6 MeV, a

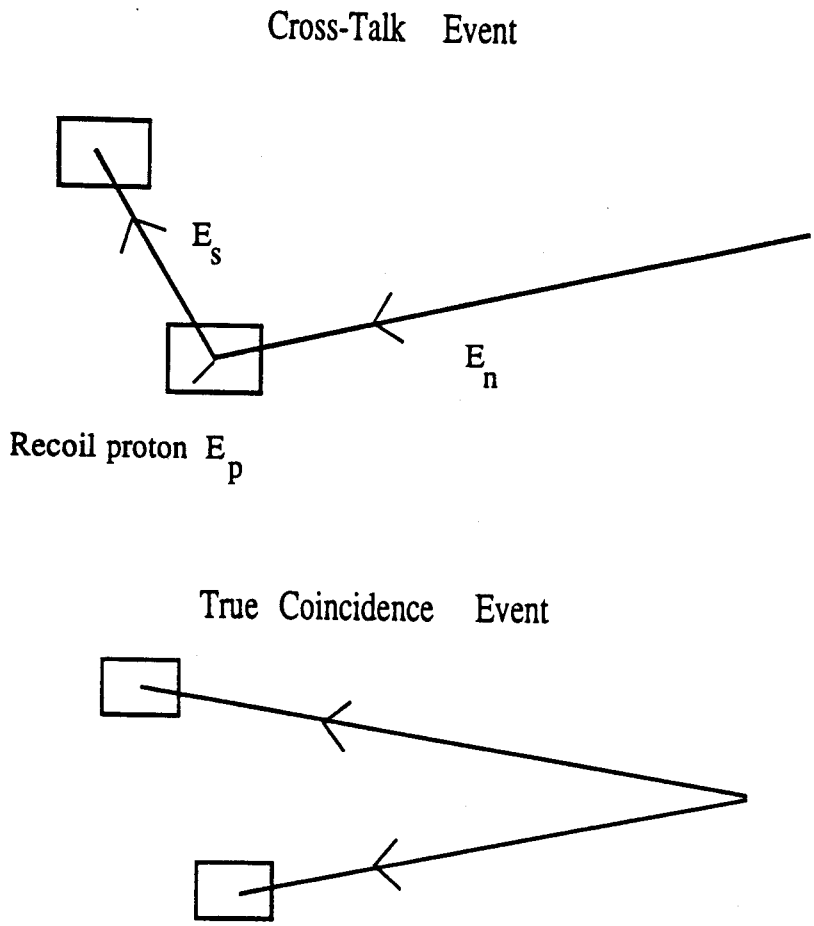

Figure D.1: (a) Sketch of a typical cross talk event, which yields false neutron-neutron coincidence events. (b) True coincidence event.

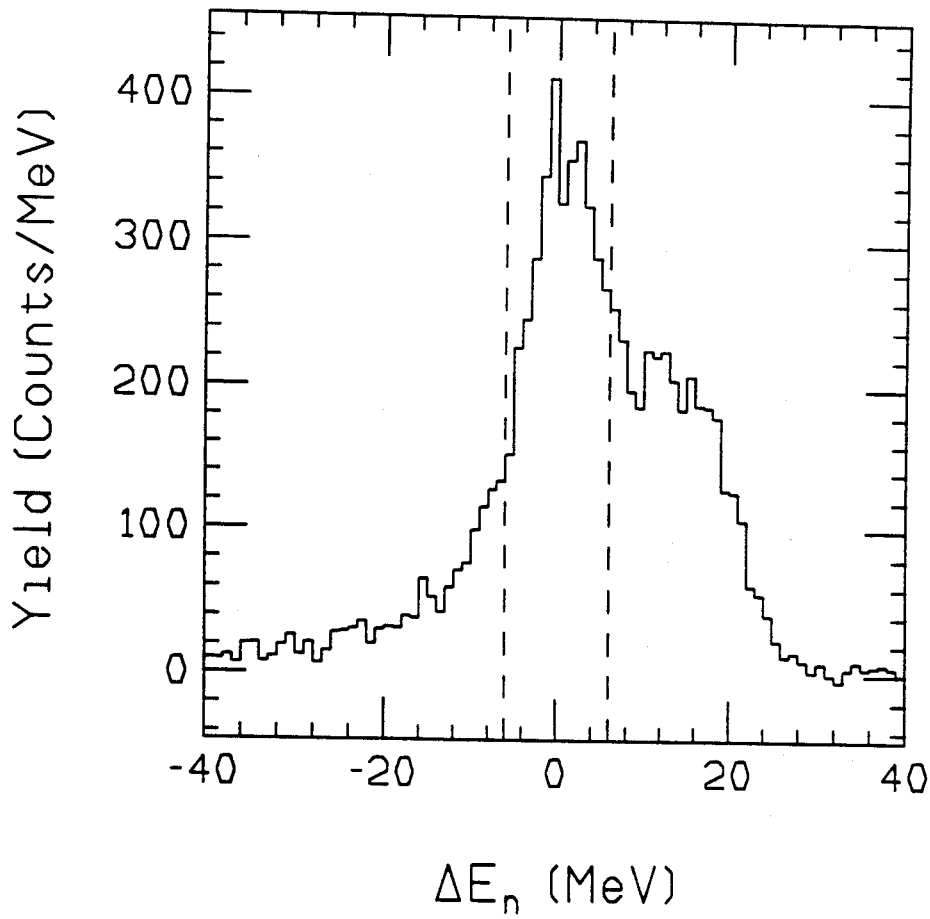

Figure D.2: ΔE_n spectrum constructed from the pure cross talk events from the ^{7}Li(p,n) reaction. The dashed vertical lines indicates the gate used for cross talk rejection in the ΔE_n spectrum from the ^{11}Li data

measured pulse height in the scintillator would correspond to a much higher energy α-particle than a proton. Attributing the pulse to a proton then yields too low a value for E_p, and hence $\Delta E_n > 0$. The negative Q-value of the reaction also causes $\Delta E_n > 0$. The vertical dashed lines indicate the width of the gate used in the ΔE_n spectrum for the ^{11}Li data to reject cross-talk events. As shown in Figure D.2, most of the cross-talk events from reactions other than n-p scattering were not eliminated by the gating procedure. The existence of this type of events was one of the primary motivations for developing a Monte Carlo simulation that could reproduce the ^{7}Li(p,n) data and evaluate the amount of cross-talk contamination remaining in the ^{11}Li data before and after cross-talk rejection.

Another motivation for developing a Monte Carlo simulation was the realization that cross-talk events occuring between neighboring detectors would be more difficult to eliminate than cross-talk events occuring between detectors separated by greater distances. A good illustration of this was found in the ^{7}Li(p,n) data. Figure D.3a depicts the ΔE_n spectrum from cross-talk events from detectors in the same array, which primarily come from neighboring detectors. Although still peaked at ΔE_n =0, the spectrum is broader than the ΔE_n spectrum constructed from cross-talk events that occurred in detectors in different arrays, as shown in Figure D.3b. Because neighboring detectors are in such close proximity to each other, the finite size of the detectors makes the actual flight path of the scattered neutron less well defined, which caused a spread in the calculated energy E_s of the scattered neutrons. For cross-talk events from detectors in different arrays, the distance between detectors was at least 1 m, hence the flight path of the scattered neutron, and thus the energy, was better defined. As shown in Figure D.3b, the cross-talk rejection procedure for these events was more effective.

The ΔE_n spectrum for the ^{11}Li data is shown in Figure D.4. These events consist

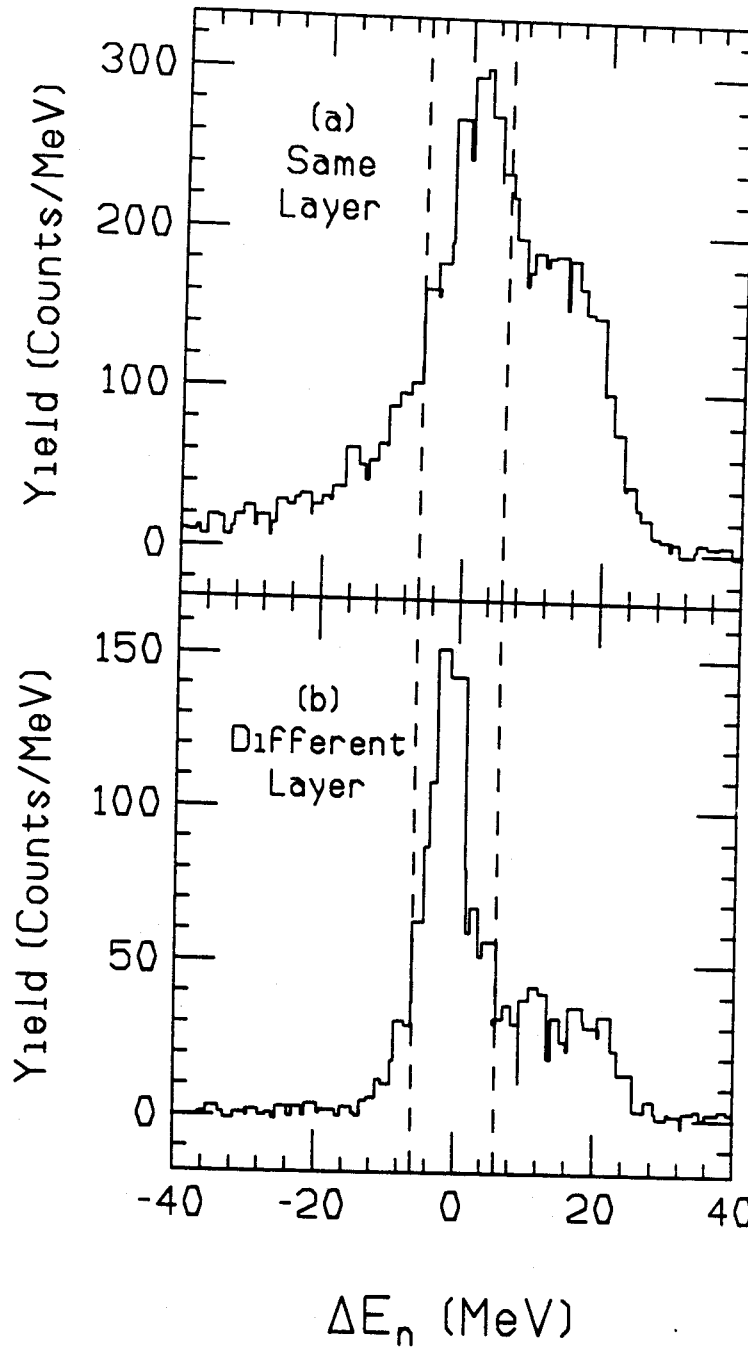

Figure D.3: (a)ΔE_n spectrum from the ^{7}Li(p,n) reaction for cross-talk between detectors in the same detector array. (b) Similar spectrum, but for cross-talk events between detectors in different arrays.

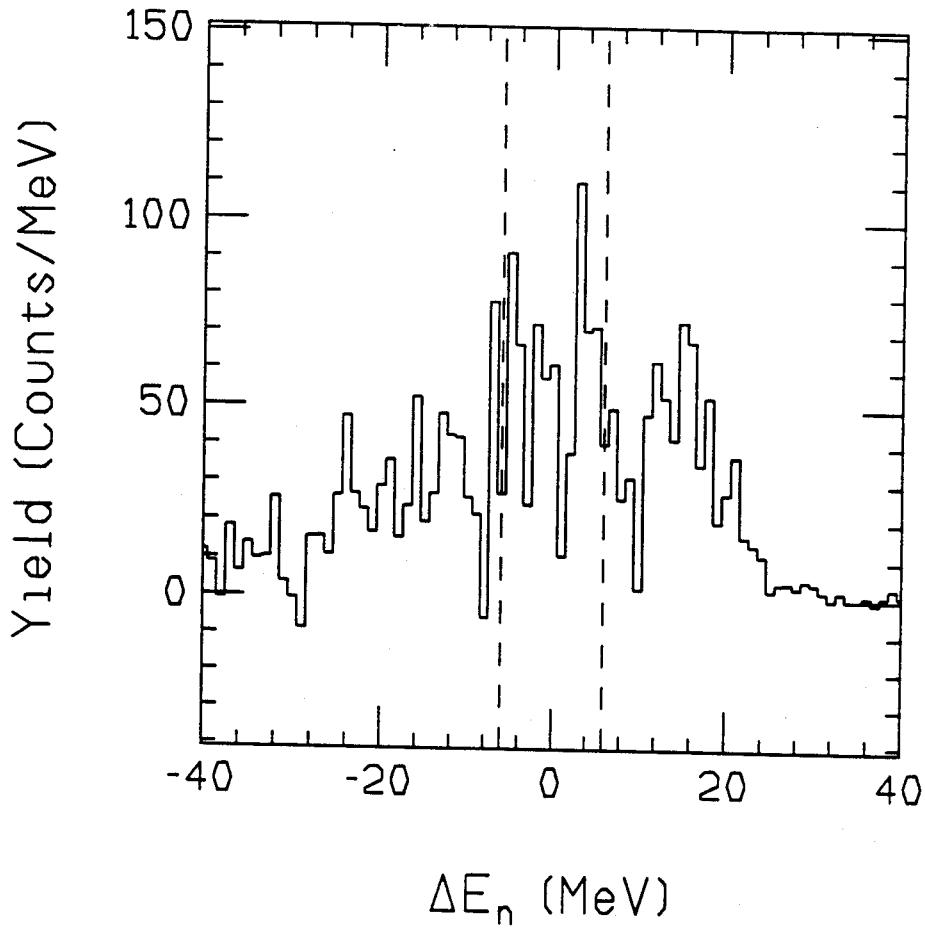

Figure D.4: ΔE_n spectrum from the ^{11}Li data. Here, the events are a mixture of cross-talk and true coincidences. The vertical dashed lines indicate the gate used for rejecting cross-talk events.

of both cross-talk and true coincidences. The gate used to reject cross talk, which was determined from the ^{7}Li(p,n) data and the Monte Carlo simulation, is depicted by the dashed lines. This spectrum is very broad because the true coincidence events produce a very flat ΔE_n spectrum. In fact, the lack of a strong peak at ΔE_n =0 indicates the cross-talk contamination was not too severe. This statement is also supported by the Monte Carlo simulation of the ^{11}Li data, which indicated that only about 15% of the events were cross-talk events.

Appendix E: The Virtual Photon Spectrum

The equivalent photon method is a very useful technique for extracting information about the electromagnetic excitation of radioactive nuclei, provided a reliable calculation of the photon spectrum is available. The expression for the E1 photon spectrum as a function of solid angle, given below and also in eqn. 1.3, is valid for all beam energies:

$$\frac{dN_{E1}(E)}{d\Omega} = \frac{Z_T^2\alpha}{4\pi^2}\left(\frac{c}{v}\right)^2 \varepsilon^4\xi^2 e^{-\pi\xi}\left[\frac{\varepsilon^2-1}{\varepsilon^2}\right]\left[K_{i\xi}(\varepsilon\xi)\right]^2 + \left[K'_{i\xi}(\varepsilon\xi)\right]^2] \qquad \text{(E.1)}$$

Here, Z_T is the target charge, α is the fine structure constant, v is the projectile velocity, $\xi = Ea/\hbar\gamma v$, a is half the distance of closest approach for a head on collision in a strictly Coulomb potential, E is the excitation energy delivered to the projectile, $d\Omega$ is the element of solid angle into which the projectile deflects and ε is the eccentricity of the Coulomb orbit, which is related to the Rutherford scattering angle by $\varepsilon = 1/\sin(\theta/2)$. The function $K_{i\xi}(\varepsilon\xi)$ is a modified Bessel function with an imaginary index, and $K'_{i\xi}(\varepsilon)$ is the derivative of K with respect to the argument. These Bessel functions are not tabulated, and must be calculated numerically from the integral [49]:

$$K_{i\xi}(\varepsilon\xi) = \int_0^\infty e^{-\varepsilon\xi\cosh x}\cos\xi x\, dx \qquad \text{(E.2)}$$

Equation 5.1 was integrated over all pure Coulomb orbits to obtain the spectrum as a function of excitation energy. The integrated expression, $N_{E1}(E)$, was used to determine the photonuclear cross section from the measured Coulomb dissociation cross section (eqn. 1.4). Although a closed form expression exists for $N_{E1}(E)$ [50], it is a complicated function of bessel functions of complex arguments and imaginary indices, and their derivatives. Therefore, it was easier to perform a numerical integration of eqn. E.1 over solid angle. The integration is performed over $d\Omega = 2\pi \sin\theta d\theta$ from $\theta = 0$ up to $\theta = \theta_g$, where θ_g is the grazing angle. To calculate the grazing angle the sum of the radii of Pb and ^{11}Li is required. The ^{11}Li radius was taken to be 3.2 fm from ref. [1]. It will be shown later that the integrated photon spectrum is fairly insensitive to the value chosen for the ^{11}Li radius. For each value of excitation energy E, eqn. E.1 was integrated over solid angle. The result of the calculation, $N_{E1}(E)$ versus E, is shown in Figure E.1 by the solid line.

Because of the large amount of computer time necessary to perform this calculation, some approximations were also investigated. Hussein *et al.* [50] has given an approximation for the photon spectrum versus excitation energy that is expected to be valid in the regime of intermediate energy projectiles ($\approx$ 30 MeV/nucleon - 100 MeV/nucleon). The dotted line in Figure E.1 shows the result of this approximation for a ^{11}Li beam at 28 MeV/nucleon. The curves agree to better than 2%. Another approximation, the relativistic approximation, yields the simplest form for the photon spectrum. In the relativistic approximation straight line trajectories are assumed, hence the integration of eqn. E.1 over $d\Omega$ is replaced by an integration over $2\pi\ b\ db$. The expression, introduced initially by Fermi [51] and further developed by Weizsäcker and Williams [52], is given by:

$$N_{E1}(E) = \frac{2}{\pi} Z_T^2 \alpha (\frac{c}{v})^2 \left[x K_0(x) K_1(x) - \frac{1}{2} (\frac{v}{c})^2 x^2 \left(K_1^2(x) - K_0^2(x) \right) \right] \qquad \text{(E.3)}$$

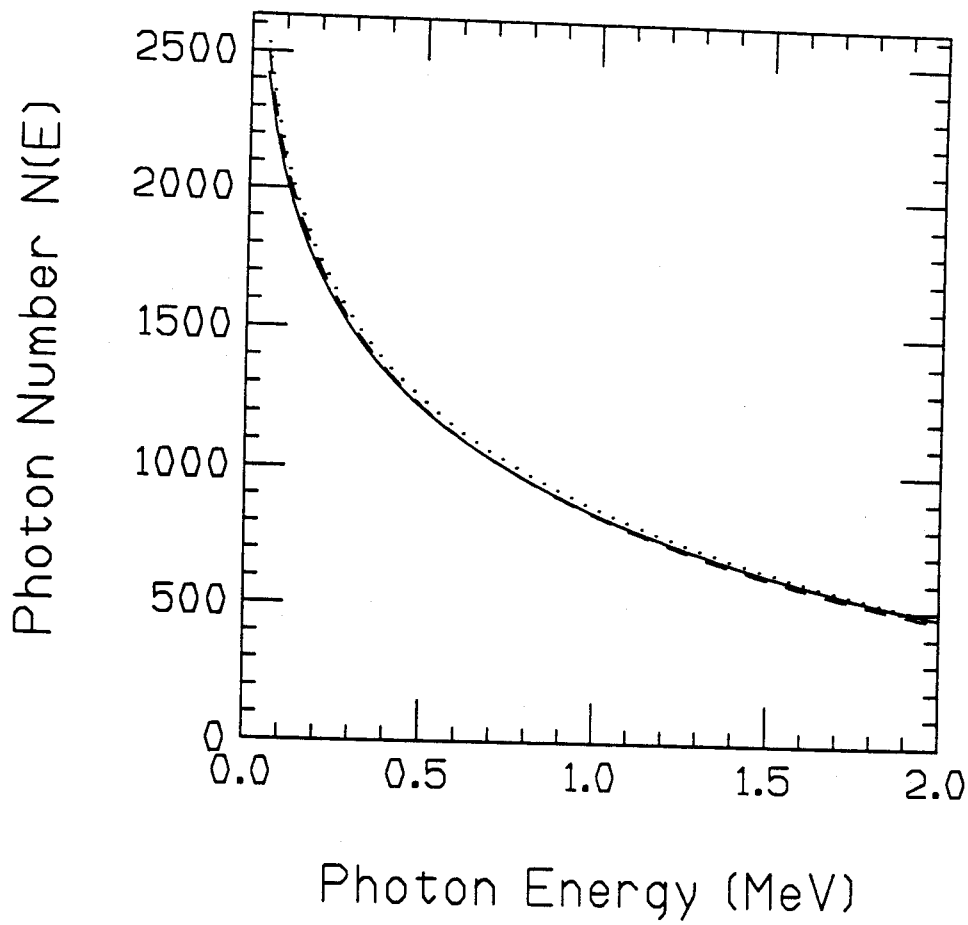

Figure E.1: Three different calculations are shown for the equivalent photon spectrum. (a) The solid line uses the expression valid for all beam projectile energies, the dotted line is the result of an approximation for intermediate energies [50] and the dashed line is the result of a relativistic approximation

In this expression, K_0 and K_1 are modified Bessel functions of the argument x, with $x = Eb_{min}/\hbar\gamma v$. A calculation of the photon spectrum for b_{min}=10.3 fm is shown in Figure E.1 by the dashed line. This value of b_{min} corresponds to the sum of the nuclear radii of Pb and ^{11}Li , using 3.2 fm for the ^{11}Li radius. The relativistic approximation also agrees to better than 2% with the exact calculation. Therefore, the relativistic approximation can be used to calculate the virtual photon spectrum to high accuracy even for beam energies as low as 28 MeV/nucleon.

In order to calculate the photon spectrum with any of the above expressions, the sum of the nuclear radii of Pb and ^{11}Li must be known to calculate b_{min}. Although the radius of Pb is easily calculated from the empirical expression $1.2A^{1/3}$, it is not so obvious what value to use for ^{11}Li because of the neutron halo. In this work, the matter radius of 3.2 fm was used, based on the measurement by Tanihata *et al.* [1], which yielded b_{min} = 10 fm. To investigate the sensitivity of $N_{E1}(E)$ to b_{min}, the photon spectrum was calculated for values of b_{min} =9, 10, and 11 fm using the relativistic approximation. The result of the calculations are shown in Figure E.2 by the dotted, solid, and dashed line for minimum impact parameters of 9, 10, and 11 fm, respectively. The shapes of the spectra are similar, but not the same. For example, for an excitation energy of 1 MeV, the photon spectrum increases by 12% between b=9 and b=11 fm. However, because there is little variation in the shape of the spectra, only the energy-integrated photonuclear cross section σ_{E1} will be affected by the uncertainty in b_{min}. More importantly, the shape of the photonuclear spectrum and the extraction of the Breit-Wigner parameters will be unaffected by the sensitivity of $N_{E1}(E)$ to b_{min}.

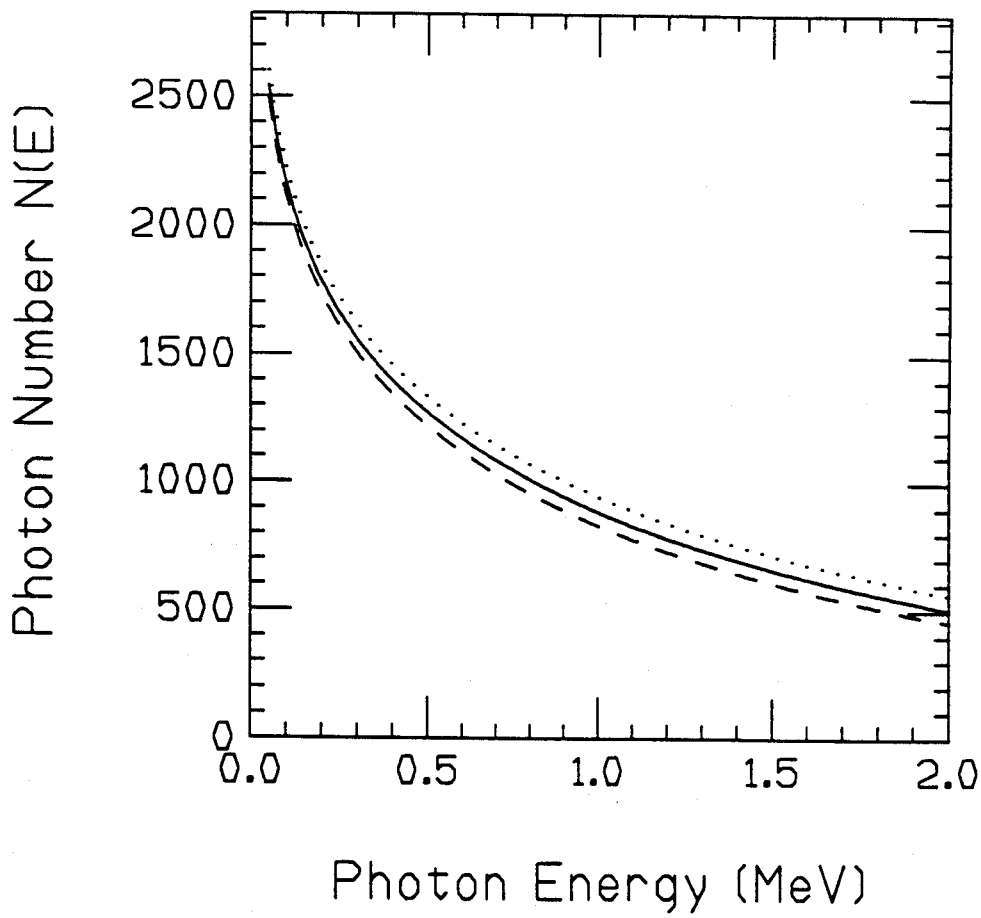

Figure E.2: Calculation of the equivalent photon spectrum using the relativistic approximation for b_{min} = 9 fm (dotted line), b_{min} = 10 fm (solid line), and b_{min} = 11 fm (dashed line).

Appendix F: Electronics and Data Acquisition

The basic flow of the electronics will be described in the following appendix. First the processing of the neutron signals will be detailed, followed by a description of the processing for the telescope signals. A description of the logic used for fragment singles events, neutron-fragment coincidence events, and the main features of the data acquisition scheme will be given.

I: Neutron Detectors

As shown in Figure F.1, signals from the neutron detectors were first split by an NSCL-built 4-way splitter (4WS) into three output signals. One of the output signals was integrated by a Lecroy 2249W ADC module to determine the area of the entire signal (Q_{tot}). Another signal from the splitter was used to determine the area under the tail of the pulse (Q_{tail}). A two-dimensional plot of Q_{tot} versus Q_{tail} was used during off-line analysis for neutron/γ-ray discrimination. The signal for Q_{tail} was put into a Phillips 7145 Linear Gate (LG) module. The third output from the splitter was sent to a Tennelec 455 Constant Fraction Discriminator (CFD). The NIM output signal from the discriminator was input to an NSCL Quad Gate Generator (GG), which in turn generated a 300 ns wide gate. This gate was also sent to the linear gate module, being delayed to arrive approximately 30 ns after the peak of the signal Q_{tail}.

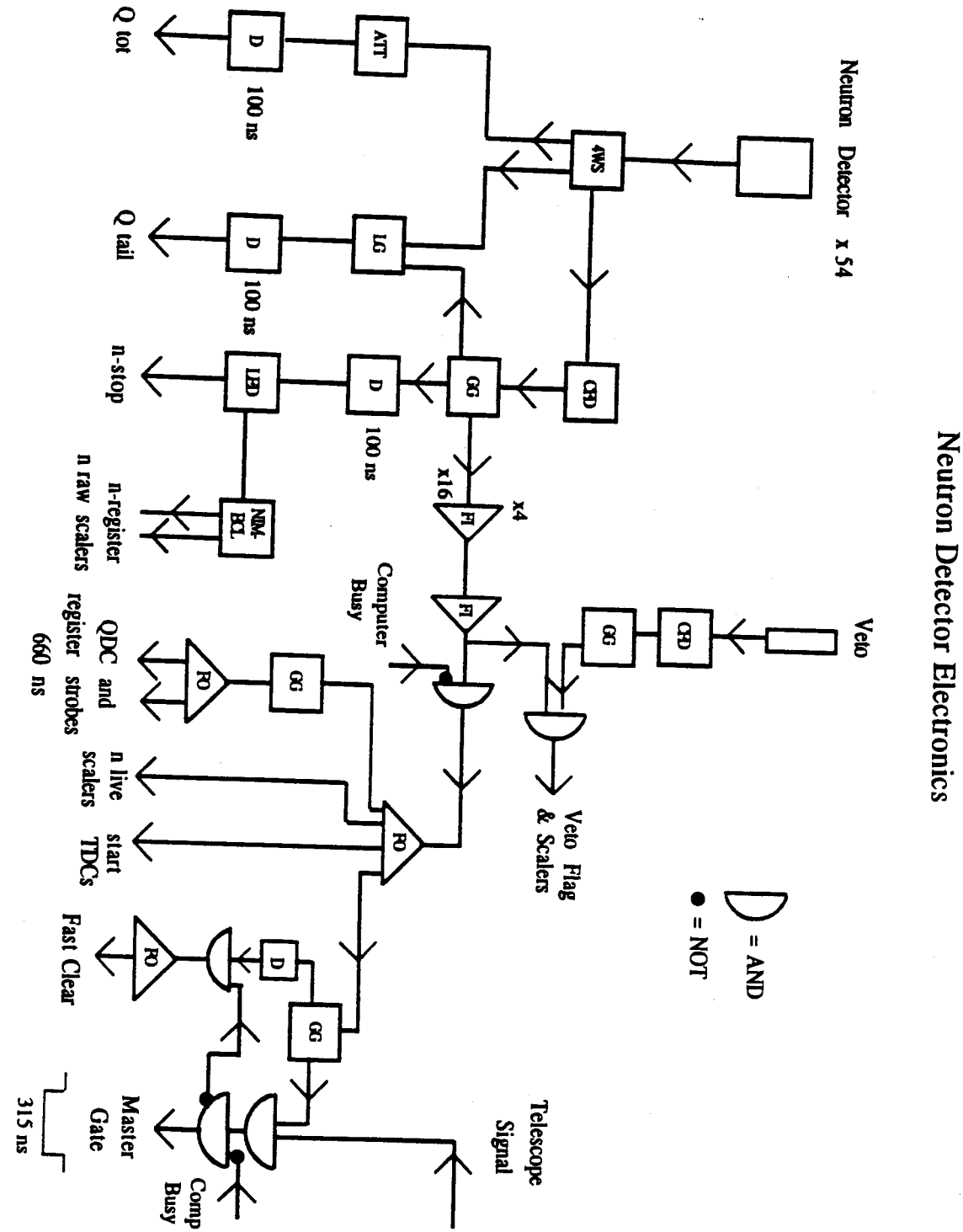

Figure F.1: Electronics setup for the neutron detector signal processing. The module abbreviations are defined in the text.

The output of the linear gate module was an analog signal representing only the tail portion of the signal from the neutron detector. The signal was also integrated by a Lecroy 2249W ADC module.

This method of obtaining the Q_{tail} signal, i.e. using a LG, is quite different from the technique used in previous experiments such as 88020 and 86006, but it was necessary when coincidence events between a fragment and two neutrons were being measured. For Q_{tail}, the gate must be timed to begin approximately 30 ns later than when the analog signal peaks. The only constraint on the gate for the Q_{tot} signal is that it arrives before the Q_{tot} signal. For events where only one neutron is detected, the signal from the detector can be split as shown in Figure F.1 and one of the outputs used to generate gates for Q_{tot} and Q_{tail} that are sent directly to the ADC modules. However, for events where two neutrons are detected, the arrival time of the Q_{tot} and Q_{tail} signals for the second neutron will have no correlation with the gates generated by the first neutron because of the different neutron flight times. Therefore the signals for the second neutron will not be properly gated by the ADC and good neutron/γ-ray discrimination will not be possible.

For the Q_{tot} signal, this problem is easily overcome by using a wide gate (660 ns for this experiment) and making the Q_{tot} signal of the leading neutron arrive about halfway through the gate, as shown in Figure F.2. The 660 ns gate was wide enough to still encompass the signal from a second neutron under either of the following extreme conditions:

1. The second neutron has an energy near the minimum value that is expected to be measured in the experiment, and it strikes the detector that is the furthest distance from the target, yielding a very large tof relative to the leading neutron.

2. The second neutron has an energy near the maximum value expected and strikes

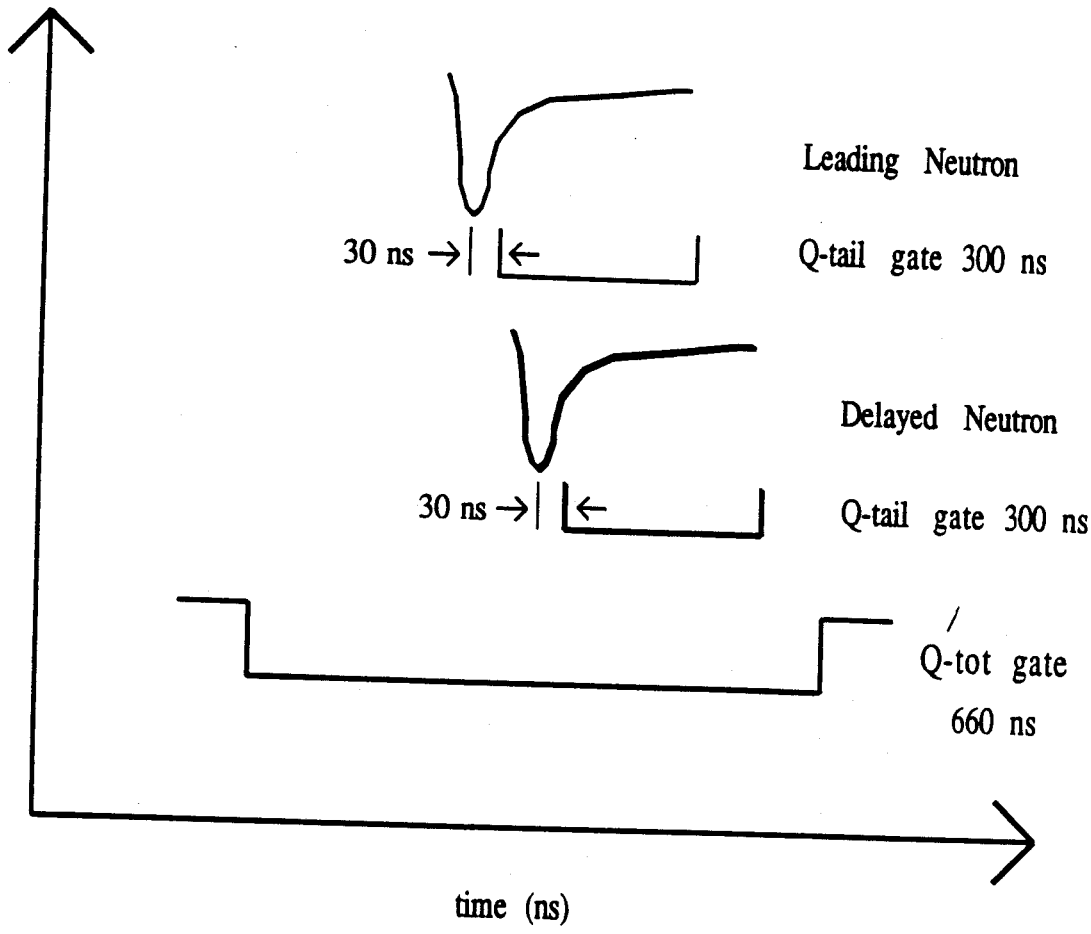

Figure F.2: Schematic of the timing for the leading and delayed neutron. Each signal has a separately timed gate for the Q_{tail} signal. Both the gate and the analog signal are put into the Linear Gate module. The Q_{tot} gate is used in the ADC modules for both the Q_{tot} and Q_{tail} signal.

a detector that is closest to the target, yielding a very short tof relative to the leading neutron.

For the Q_{tail} signal, the problem is more difficult because of the more precise timing required for the gate relative to the analog signal. The method used in this experiment was to generate a separate gate from the analog signal from each detector that yielded a signal. These gates were timed to begin 30 ns later than the time of the peak of the analog signal, as shown in Figure F.2. The gates were all 300 ns wide. The analog signal and it's 300 ns gate were put into a linear gate module. A separate linear gate input was available for each neutron detector. The output (analog) of the linear gate was the portion of the Q_{tail} signal that was inside the input gate. This signal was sent to a Lecroy 2249W ADC for integration. The gate for the ADC module is the 660 ns Q_{tot} gate described above and shown in Figure F.2.

The remaining signal processing for the neutron detectors will be described next. Another of the GG outputs was further delayed (100 ns), sent through a leading edge discriminator (LED), and into a Lecroy 2228A TDC as a stop signal from the neutron detector. The LED was used to produce a well defined NIM signal from the gate whose shape was mildly distorted by the 100 ns cable delay. Because the neutron detector signals start all the TDCs, the TDC value determined from the neutron stop signal is only related to the cable delay and processing time of the various electronic modules. However, this value is necessary to calculate the neutron time-of-flights.

The third output from the GG from each detector was sent to a series of NSCL logic Fan-In (FI) modules. The Fan-In modules acted as a 54-fold OR operation. The output of the Fan-In modules was sent to an NSCL Fan-Out (FO) module, and fanned out to several areas. One of the outputs was sent to a gate generator to form a 315 ns gate labeled the coincidence gate in Figure F.1. A NIM signal from the

fragment telescope electronics was required to arrive within this 315 ns gate for an event to be classified as a coincidence event and a Master Gate signal to be generated. Other outputs from the Fan-Out served to start all the TD modules, increment the neutron scalers, generate the 660 ns ADC gates and strobe the neutron bit registers. The function of the bit registers will be discussed in section IV.

The 315 ns coincidence gate was also delayed and used in an AND operation with a NOT from the Master Gate coincidence unit. A NOT Master Gate indicated there was no fragment that arrived within the 315 ns coincidence gate. For this case, a neutron signal but no fragment signal, a NIM output from the AND between the coincidence gate and NOT Master Gate was used to fast-clear the TDC and 2249W ADC modules. The fast-clear was necessary because the neutron TDCs and ADCs were started before it was determined electronically that there was a fragment signal also present. Because neutron singles events would be dominated by cosmic ray events (2400/s), they were not written to tape, and thus it was necessary to clear the neutron TDC and ADC modules in the case of a neutron singles event. Of course, an alternative method would have been to delay the neutron signals by several hundred ns to be sure there was a neutron-fragment coincidence, thus eliminating the need for a fast-clear, but this technique would have required many more delay boxes and leading edge discriminators.

Finally, because the clear inputs on the TDC and ADC modules were used by the fast-clear input, for a good events the modules were cleared internally by the data acquisition software. Also, as shown in Figure F.1, veto detector signals were sent to a CFD and a GG. For veto signals in coincidence with neutron detector signals, bit-64 in the neutron register was flagged by a NIM signal. This concludes the description of the electronic processing of the neutron detector signals. The fragment and beam particle signal processing will be described next.

II: Fragment Detectors

The electronic processing for the fragment and beam detectors is shown in Figure F.3. An energy signal was taken from each of the 16 horizontal and 16 vertical strips from the silicon strip detector. The energy signals from the horizontal (front) strips were put into LBL 21X742 time pick-off units (TPOs). The time pick-offs provided both a fast output and an output to be further processed by pre-amplifiers and amplifiers. The fast outputs were first amplified by NSCL-built fast amplifiers and then were sent to CFDs. One of the CFD outputs was delayed by 400 ns, reshaped by an LED, and put into TDC modules as the stop signal for the neutron tof measurement. The LED output was also sent to the NIM-to-ECL converters, and the ECL output from the converter was put into the fragment bit registers, which required ECL-type logic signals. The NIM output from the converters served to increment the fragment scalers. The other outputs from the time pick-off units, which yielded signals for determining the energy deposited in the detectors, were processed by NSCL-built pre-amplifiers and Tennelec 241S amplifiers, and then sent to Ortec AD811 peak-sensing ADCs.

In order to classify a fragment event as a good event, it was required that signals from a horizontal strip, a vertical strip, ΔE2 and the CsI detector be present. The Tennelec 241S amplifiers used for the fragment detectors provided a fast output as well as an output for the ADCs. For the vertical strips, ΔE2, and the CsI detector, the fast outputs were sent to CFDs and the NIM output from the CFDs, were subjected to a 4-fold AND operation. For the front strips, the NIM signals from the CFD following the fast amplifier were used in the AND operation. If all detectors fired, the 4-fold coincidence unit issued a NIM output that was used for an AND operation with the coincidence gate generated by the neutron detectors. If the AND was satisfied, a Master Gate signal was generated. This Master Gate signal was fanned-out as a

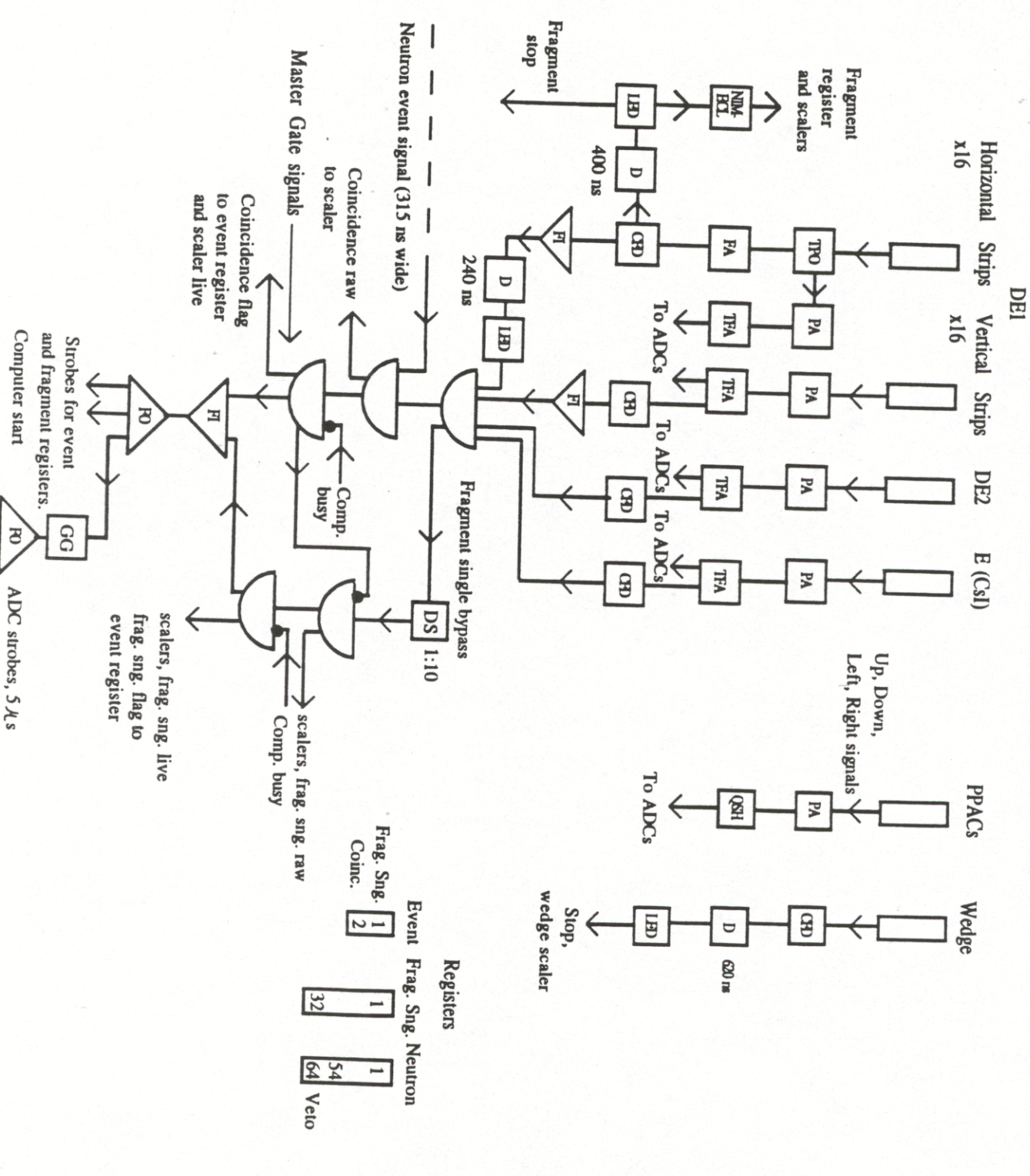

Figure F.3: Electronics processing for the fragment and beam detector signals. The module abbreviations are defined in the text.

computer start signal, as a flag indicating a coincidence event is present, as strobes for the event and fragment registers and was also sent to a gate generator to produce the 5 μs gates for the Ortec ADC modules.

In addition to the coincidence events, it was also necessary to record the number of unreacted ^{11}Li particles striking the telescope in order to determine cross sections and to normalize spectra from target-out measurements before subtracting from spectra recorded during target-in measurements. Also, it was desirable to record the number of ^{9}Li fragments detected so a 2-neutron removal cross section could be determined independently from the coincidence data. Therefore, a fragment singles bypass was also used in order to write fragment singles events to tape. Provided a good fragment event was present, determined by the 4-fold AND operation mentioned previously, the resulting NIM signal was also sent through a downscaler. Because only about 10% of the incident ^{11}Li particles dissociate into ^{9}Li and two neutrons in the target and detectors, and because the neutron detection efficiency is about 10%, the data being put to tape would consist predominately of fragment singles events. Thus the fragment singles events were downscaled by a factor of 10. The bypass circuit is depicted in Figure F.3. The NIM output from the downscaler is subjected to an AND operation with a NOT Master gate signal. If the AND is satisfied, it indicates there was no Master gate signal present, hence this event was not a coincidence event since there was not a signal from the neutron detectors. After verifying the computer was free, this NIM signal was then sent to the event register to flag the event as a fragment singles event. Also, it was sent to the fragment scalers, and then it was fanned-out to strobe the registers and start the computer and to strobe the Ortec ADC modules.

III: Beam Detectors

The beam detectors consisted of two PPAC detectors and a scintillator which was labelled S1 in Chapter 2. Each PPAC produced four signals, resistively divided into up, down, left and right signals. These signals were sent to an MSU-built pre-amplifiear (same type as used for the silicon detectors), to quad shaping amplifiers (labelled QSH in Figure F.3), and finally to an Ortec AD811 ADC module. This ADC was strobed by the same 5 μs gates as the ADC modules dedicated to the fragment telescope signals. A signal in the PPACs was not required to define a valid fragment event because the detection efficiency of the PPAC was suspected to be less than 100%.

The signal from S1 was used as a stop signal for the beam time-of-flight measurement. The signal was sent to a CFD, delayed 600 ns, reshaped in an LED, and sent to a TDC and scaler input.

IV: Data Acquisition

The data acquisition system at the NSCL is well documented in the manual *NSCL Data Acquisition System Reference Guide* by Ron Fox and John Winfield. In this section, the basic strategy of the data acquisition related to the layout of the input and output bit registers was briefly discussed. The layout of the input bit registers were shown in Figure F.3.

Separate registers were used for the neutrons detectors, the fragment registers and the event classification registers. The electronics for each of the 54 neutron detectors was wired to a separate bit in the 64 bit neutron register. A Lecroy 4448 48-bit ECL coincidence register plus an SEC 16 bit register was used. The registers required strobe inputs as well as clear signals. The origin of the strobe input was described in

the section on neutron detector electronics. The clear signal was taken from a Bi Ra 3251 NIM output register that generates a NIM signal when the front-end computer finishes processing an event. Provided the coincidence bit in the event register is flagged, the data acquisition code scans the neutron register to see which bits were flagged. For the flagged bits, the ADC and TDC channels corresponding to those detectors were read and then cleared.

Each of the 32 strips from the strip detector was also wired into a Lecroy 4448 ECL coincidence register. For either a coincidence or a fragment singles event, as determined by the event register, the data acquisition code scans the fragment register for all flagged bits. For any of the first 16 bits that are flagged, the ADC and TDC channels corresponding to those horizontal strips are read and cleared. Also read are the ADC values from ΔE2, the CsI detector, the PPAC ADC module and the TDC channel of S1. For any of the bits 17-32 that are flagged, the ADC values corresponding to those vertical strips are read and cleared. Finally, LAM time-out flags are issued by the software and generated by the Bi Ra 3251 NIM output register. These signals were sent to a scaler to check for the presence of LAM time-outs during the experiment.

BIBLIOGRAPHY

Bibliography

[1] I. Tanihata, H. Hamagaki, O. Hashimoto, Y. Shida, N. Yoshikawa, K. Sugimoto, O. Yamakawa, T. Kobayashi, and N. Takahashi, Phys. Rev. Lett., **55**, 2676 (1985).

[2] T. Kobayashi, O. Yamakawa, K. Omata, K. Sugimoto, T. Shimoda, N. Takahashi, and I. Tanihata, Phys. Rev. Lett., **60**, 2599 (1988).

[3] A.S. Goldhaber, Phys. Lett. **B53** 306 (1974).

[4] P. G. Hansen and B. Jonson, Europhys. Lett. **4**, 409 (1987).

[5] R. N. Boyd and I. Tanihata, Phys. Today 44 (1992).

[6] T. Kobayashi, Nucl. Phys. **A538**, 343c (1992).

[7] G. Baur, C.A. Bertulani, and H. Rebel, Nucl. Phys. **A458**, 188 (1986).

[8] F. Ajzenberg-Selove, Nucl. Phys. **A490**, 1 (1988).

[9] T. Kobayashi, S. Shimoura, I. Tanihata, K. Katori, K. Matsuta, T. Minamisono, K. Sugimoto, W. Muller, D.L. Olson, T.J.M. Symons, and H. Wieman, Phys. Lett **B232**, 51 (1989).

[10] K. Ikeda, Nucl. Phys. **A538**, 355c (1992).

[11] B.L. Berman and S.C. Fultz, Rev. Mod. Phys. **47**, 713 (1975).

[12] G.F. Bertsch and H. Esbensen, Ann. Phys. **209**, 327 (1991).

[13] N.Teruya, C.A. Bertulani, S. Krewald, H. Dias, and M.S. Hussein, Phys. Rev **C43**, R2049 (1991).

[14] H. Esbensen and G.F. Bertsch, Nucl. Phys. **A542**, 310 (1992).

[15] C. A. Bertulani, G. Baur, and M. S. Hussein, Nucl. Phys **A526**, 751, (1991).

[16] K. Ieki, D. Sackett, A. Galonsky, C. A. Bertulani, J. J. Kruse, W. G. Lynch, D. J. Morrissey, N. A. Orr, H. Schultz, B. M. Sherill, A. Sustich, J. A. Winger, F. Deak, A. Horvath, A. Kiss, Z. Seres, J. J. Kolata, R. E. Warner, and D. L. Humphrey, M.S.U. submitted to Phys. Rev. Lett.

[17] K. Alder, A. Bohr, T. Huus, B. Mottleson, and A. Winther, Rev. Mod. Phys. **28**, (1956) 432.

[18] C.A. Bertulani and G. Baur, Phys. Rep. **163**, 299, (1988).

[19] C.A. Bertulani and A. Sustich, to be published in Phys. Rev. C.

[20] B.M. Sherrill, D.J. Morrissey, J.A. Nolen, and J.A. Winger, Nucl. Instr. and Meth. **B56/57**, 1106 (1991).

[21] T. Davinson, A.C. Shotter, E.W. Macdonald, S.V. Springham, P. Jobanputra, A.J. Stephens, and S.L. Thomas, Nucl. Instr. and Meth. **A288**, 245 (1990).

[22] N. Colonna, G.J. Wozniak, A. Veeck, W. Skulski, G.W. Goth, L. Manduci, P.M. Milazzo and P.F. Mastinu, Nucl. Instr. and Meth. bf A321, 529 (1992).

[23] W.G. Gong, N. Carlin, C.K. Gelbke, and R. Dayton, Nucl. Instr. and Meth. **A287**, 639 (1990)

[24] W.G. Gong, Y.D. Kim, G. Poggi, Z. Chen, C.K. Gelbke, W.G. Lynch, M.R. Maier, T. Murakami, M.B. Tsang, and H.M. Xu, Nucl. Instr. and Meth. **A268**, 190 (1988).

[25] D. Horn, G.C. Ball, A. Galindo-Uribari, E. Hagberg, and R.B. Walker, Nucl. Instr. and Meth. **A320**, 273 (1992).

[26] J. Heltsley, L. Brandon, A. Galonsky, L. Heilbronn, B.A. Remington, S. Langer, A. Vandermolen, and J. Yurkon, Nucl. Instr. and Meth. **A263**, 441 (1988).

[27] M. Cronqvist, B. Jonson, T. Nilsson, G. Nyman, K. Riisager, H.A. Roth, O. Skeppstedt, O. Tengblad, K. Wilhelmsen, Nucl. Instr. and Meth. **A317**, (1992) 273.

[28] P. Desesquelles, A. Dauchy, A. Giorni, D. Heuer, A. Lleres, C. Morand, J. Saint-Martin, P. Stassi, J.B. Vian, B. Chambon, B. Cheynis, and D. Drain, Nucl. Instr. and Meth. **A307**, 366 (1991).

[29] R. A. Cecil, B. D. Anderson, and R. Madey, Nucl. Instr. and Meth. **161**, 439 (1979).

[30] A.C.C Villari, W. Mittig, E. Plagnol, Y. Schultz, M. Lewitowicz, L. Bianchi, B. Fernandez, J. Gastebois, A. Gillibert, C. Stephan, L. Tassan-Got, G. Audi, W. Zhan, A. Cunsolo, A. Foti, A. Belezyorov, S. Lukyanov, and Y. Penionzhkevich, Phys. Lett. **B268**, 345 (1991).

[31] B. Blank, J.J. Gaimard, H. Geissel, K.H. Schmidt, H. Stelzer, K. Summerer, D. Bazin, R. Del Moral, J.P. Dufour, A. Fleury, F. Hubert, H.G. Clerc, and M. Steiner, Z. Phys. A-Hadrons and Nuclei 340, 41, (1991).

[32] R. Anne, S.E. Arnell, R. Bimbot, H. Emling, D. Guillemaud-Mueller, P.G. Hansen, L. Johannsen, B. Jonson, M. Lewitowicz, S. Mattsson, A.C. Mueller, R.

Neugart, G. Nyman, F. Pougheon, A. Richter, K. Riisager, M.G. Saint-Laurent, G. Schrieder, O. Sorlin, and K. Wilhelmsen, Phys. Lett. B **250**, 19, (1990).

[33] H. Sagawa, N. van Giai, N. Takigawa, and M. Ishihara, preprint.

[34] N.A. Orr, N. Anantaraman, S.M. Austin, C.A. Bertulani, K. Hanold, J.H. Kelley, D.J. Morrissey, B.M. Sherrill, G.A. Souliotis, M. Thoennesen, J.S. Winfield, and J.A. Winger, Phys. Rev. Lett. **69**, 2050 (1992).

[35] P.R. Bevington, *Data Reduction and Error Analysis for the Physical Sciences* (McGraw-Hill, New York, 1969), p.237.

[36] G. Baur *"Proceedings of International Symposium on Strucure and Reactions of Unstable Nuclei"*, Niigata, Japan (1991).

[37] R. Serber, Phys. Rev. 72, 1008 (1947).

[38] A.I. Amelin, M.G. Gornov, Yu. B. Goruv, A.L. Ll'in, P.V. Morokhov, V.A. Pechkurov, V.I. Savel'ev, F.M. Sergeev, S.A. Smirnov, B.A. Chernyshev, R.R. Shafigullin and A.V. Shishkov, Sov J. Nucl. Phys. **52**, 782, (1990).

[39] K. Wilcox *et al.* , Phys. Lett. **B59**, 142 (1975).

[40] A. Sustich, Z. Phys. A-Hadrons and Nuclei 342, 31 (1992).

[41] R. Shyam, P. Banerjee, and G. Baur, Nucl. Phys. **A540**, 341 (1992).

[42] C.A. Bertulani and L.F. Canto, Nucl. Phys. **A539**, 163 (1992)

[43] K. Riisager, R. Anne, S.E. Arnell, R. Bimbot, H. Emling, D. Guillemaud-Mueller, P.G. Hansen, L. Johannsen, B. Jonson, A. Latimier, M. Lewitowicz, S. Mattsson, A.C. Mueller, R. Neugart, G. Nyman, F. Pougheon, A. Richard, A. Richter, M.G.

Saint-Laurent, G. Schrieder, O. Sorlin, and K. Wilhelmsen, Nucl. Phys. **A540**, 365, (1992).

[44] I. Tanihata, T. Kobayashi, T. Suzuki, K. Yoshida, S. Shimoura, K. Sugimoto, K. Matsuta, T. Minamisono, W. Christie, D. Olson and H. Wieman, Phys. Lett. **B287**, 307 (1992).

[45] P.G. Hansen, to be published in Nucl. Phys. A.

[46] *Table of Isosotopes* ed. by M. Lederer and V. Shirley, John Wiley and Sons Inc., NY 1978.

[47] W.G. Gong, Ph.D. Thesis, Michigan State University, 1991.

[48] L. Heilbronn, A. Galonsky, C.K. Gelbke, W.G. Lynch, T. Murakami, D. Sackett, H. Schelin, M.B. Tsang, F. Deak, A. Kiss, Z. Seres, J. Kasagi and B.A. Remington, Phys. Rev. **C43**, 2318, 1991.

[49] *Handbook of Mathematical Functions*, Natl. Bur. Stand. Appl. Math. Ser. No. 55, edited by M. Abramowitz and I.A. Stegun (U.S. GPO, Bureau of Standards, Washington, DC, 1964)

[50] M.S. Hussein, M.P. Pato and C.A. Bertulani, Phys. Rev. **C44**, 2219, (1991).

[51] E. Fermi, Z. Phys. **29**, (1924), 315.

[52] C.F. Weizsacker, Z. Phys. **88**, (1934), 612. E.J. Williams, Phys. Rev. **45**, (1934), 729.